View metadata, citation and similar papers at core.ac.uk
brought to you by CORE
provided by Online Research Database In Technology

Technical University of Denmark

Compact beamforming in medical ultrasound scanners

Tomov, Borislav Gueorguiev; Sparsø, Jens; Jensen, Jørgen Arendt; Bruun, Erik

Publication date:
2003

Document Version
Publisher's PDF, also known as Version of record

Link back to DTU Orbit

Citation (APA):
Tomov, B. G., Sparsø, J., Jensen, J. A., & Bruun, E. (2003). Compact beamforming in medical ultrasound scanners.

DTU Library
Technical Information Center of Denmark

General rights
Copyright and moral rights for the publications made accessible in the public portal are retained by the authors and/or other copyright owners and it is a condition of accessing publications that users recognise and abide by the legal requirements associated with these rights.

- Users may download and print one copy of any publication from the public portal for the purpose of private study or research.
- You may not further distribute the material or use it for any profit-making activity or commercial gain
- You may freely distribute the URL identifying the publication in the public portal

If you believe that this document breaches copyright please contact us providing details, and we will remove access to the work immediately and investigate your claim.

Compact beamforming in medical ultrasound scanners

Borislav Gueorguiev Tomov

January 31, 2003

Ørsted●DTU
Technical University of Denmark

SUBMITTED IN PARTIAL FULFILLMENT OF THE
REQUIREMENTS FOR THE DEGREE OF
DOCTOR OF PHILOSOPHY
AT
THE TECHNICAL UNIVERSITY OF DENMARK
JANUARY 2003

Signature of Author

THE AUTHOR RESERVES OTHER PUBLICATION RIGHTS, AND NEITHER THE THESIS NOR EXTENSIVE EXTRACTS FROM IT MAY BE PRINTED OR OTHERWISE REPRODUCED WITHOUT THE AUTHOR'S WRITTEN PERMISSION.

THE AUTHOR ATTESTS THAT PERMISSION HAS BEEN OBTAINED FOR THE USE OF ANY COPYRIGHTED MATERIAL APPEARING IN THIS THESIS (OTHER THAN BRIEF EXCERPTS REQUIRING ONLY PROPER ACKNOWLEDGEMENT IN SCHOLARLY WRITING) AND THAT ALL SUCH USE IS CLEARLY ACKNOWLEDGED.

© Copyright by Borislav G. Tomov 2004
All Rights Reserved

To my sister Tanya

Contents

Contents **i**

Abstract **iii**

Preface **v**

Acknowledgments **vii**

List of Figures **xiii**

List of Tables **xiv**

1 Introduction **1**
- 1.1 Ultrasound imaging principle 2
- 1.2 Medical ultrasound systems evolution 2
- 1.3 Blood velocity estimation 4
  - 1.3.1 Sonogram / Spectral Doppler 5
  - 1.3.2 Color flow map 6
- 1.4 Comparison with CT and MR imaging 8
  - 1.4.1 Computed tomography 8
  - 1.4.2 Magnetic resonance imaging 8
  - 1.4.3 Ultrasound imaging 9

2 Ultrasound acoustics **10**
- 2.1 Wave equation 10
- 2.2 Solutions to the wave equation 10
  - 2.2.1 Plane wave 10
  - 2.2.2 Spherical wave 11
- 2.3 Wavenumber-frequency space (*k*-space) 12

2.4 Propagation in tissue 12
2.4.1 Reflection 13
2.4.2 Scattering 13
2.4.3 Attenuation 14

3 Beamformation **15**
3.1 Transducer properties 15
3.1.1 Directivity properties of finite continuous apertures 15
3.1.2 Angular resolution concept 16
3.1.3 Directivity properties of arrays 17
3.1.4 Directivity properties of arrays of finite continuous sensors 19
3.1.5 Phased array angular resolution dependence on the incidence angle . . 20
3.2 Focusing 20
3.2.1 Focusing geometry 22
3.2.2 Influence of the speed of sound 23
3.2.3 Influence of the delay precision 23
3.3 Beamforming 24
3.3.1 Transducer element directivity implications 26
3.4 Beamforming techniques 27
3.5 Comparison between focusing techniques 29
3.6 Conclusion 30

4 Compression of the the focusing data **35**
4.1 Memory requirements in ultrasound beamforming 36
4.2 Delay calculation 37
4.3 Delta encoding 39
4.4 Piecewise-linear approximation 40
4.5 General parametric approach 42
4.5.1 Transformation to clock periods (clock cycles) 42
4.5.2 Delay values generation 42
4.6 LUCS delay generator 43
4.7 Comparison between approximation schemes 45
4.8 Discussion 46

5 Delta-Sigma modulation A/D conversion **47**
5.1 Principle of operation 48
5.1.1 Signal-to-quantization-noise ratio (SQNR) of a multi-bit Nyquist-rate data converter 48
5.1.2 SQNR of oversampling converters 50
5.2 Sample reconstruction 57
5.3 Higher-order noise shaping and band-pass modulators 57

6 DSM beamformer **58**
6.1 Previous approaches for utilizing DSM in beamformers 58
6.1.1 Modified modulator architecture for compensation of sample drop or insertion 59
6.1.2 Use of non-uniform sampling clock 61
6.2 New architecture for an oversampled beamformer 62
6.2.1 Sparse sample processing concept 62
6.2.2 Signal processing 64
6.2.3 Choice of reconstruction filter 64
6.2.4 Calculation of the necessary oversampling ratio 65
6.2.5 Simulation results 67
6.2.6 Phantom data processing results 68
6.3 Discussion 68

7 Implementation **74**
7.1 Sample buffer 75
7.2 Delay generation logic 76
7.3 Apodization 77
7.4 Summing block 78
7.5 Filters for in-phase and quadrature component 78
7.6 Interface 79
7.7 Synthesis results for a 32-channel beamformer 80

8 Conclusion **81**

A A new architecture for a single-chip multi-channel beamformer based on a standard FPGA **82**
1 Introduction 83
2 Principles behind the suggested beamformer architecture 84
2.1 Rationale for the sparse sample processing 84
2.2 Usage of the Delta-Sigma modulator in the beamformer 84
2.3 Delay generation 85
3 Beamformer architecture 87
4 Implementation tradeoffs and choices 87
5 Phantom data processing results 89
6 Conclusion 89

B Delay generation methods with reduced memory requirements **91**
1 Memory requirements in ultrasound beamforming 92
2 Index generation geometry 94
3 General parametric approach 95
3.1 Transformation to clock periods (clock cycles) 96

3.2 Influence of the directivity properties of the transducer elements . . . 96
3.3 Delay generation algorithm 98
4 LUCS delay generator 98
5 Piecewise-linear approximation 100
6 Comparison between index generation techniques 101
7 Discussion 102
8 Conclusion 103

C Compact FPGA-based beamformer using oversampled 1-bit AD converters 104
1 Introduction 104
2 Traditional beamformer architecture 106
3 New beamformer features 107
3.1 Sparse sample processing 107
3.2 Beamforming with oversampled signals 109
3.3 Reconstruction filters 111
4 Image quality 111
4.1 Calculating the necessary sampling frequency 112
4.2 Simulation results 113
4.3 Phantom image 115
5 Implementation 115
5.1 Implementation results 117
6 Discussion 117
7 Conclusion 117

Bibliography 127

Abstract

This Ph.D. project was carried out at the Center for Fast Ultrasound Imaging, Technical University of Denmark, under the supervision of Prof. Jørgen Arendt Jensen, Assoc. Prof. Jens Sparsø and Prof. Erik Bruun. The goal was to investigate methods for efficient beamforming, which make it possible to fit a large number of channels on a single integrated circuit. The use of oversampled analog-to-digital (A/D) converters with the corresponding beamforming was identified as a particularly promising approach, since it provides both inexpensive and compact A/D conversion and allows for much more compact implementation of the beamformer compared to the case where conventional A/D conversion is used.

The compact and economic beamforming is a key aspect in the progress of medical ultrasound imaging. Currently, 64 or 128 channels are widely used in scanners, top-of-the-range scanners have 256 channels, and even more channels are necessary for 3-dimensional (3D) diagnostic imaging. On the other hand, there is a demand for inexpensive portable devices for use outside hospitals, in field conditions, where power consumption and compactness are important factors.

The thesis starts with an introduction into medical ultrasound, its basic principles, system evolution and its place among medical imaging techniques. Then, ultrasound acoustics is introduced, as a necessary base for understanding the concepts of acoustic focusing and beamforming, which follow. The necessary focusing information for high-quality imaging is large, and compressing it leads to better compactness of the beamformers. The existing methods for compressing and recursive generation of focusing data, along with original work in the area, are presented in Chapter 4.

The principles and the performance limitations of the oversampled delta-sigma converters are given in Chapter 5, followed by an overview of the present architectures of oversampled beamformers. Then, a new architecture is introduced, which has the potential of achieving the highest image quality that an oversampling beamformer can provide. That architecture has been implemented using VHDL, and estimates for its performance have been obtained. The results indicate that a 32-channel beamformer reaches the target operation frequency of 140MHz, thereby providing diagnostic image with dynamic range of 60 dB for an excitation central fre-

quency of 3MHz. That image quality is comparable to that of the very good scanners currently on the market. The performance results have been achieved with the use of a simple oversampled converter of second order. The use of a higher order oversampled converter will allow higher pulse frequency to be used while the high dynamic range in the end image is preserved. The logic resource utilization of a Xilinx FPGA device XCV2000E-7 is less than 45 % when a 32-channel beamformer is implemented. The maximum number of channels that can fit in that FPGA device is 57, due to the fact that too many of the available gates take part in the routing when the channel number is increased.

Preface

The initial name of this Ph.D. project was ”Integrated circuits in medical ultrasound”, with the goal of investigating the integrated circuits necessary for the implementation of advanced medical ultrasound imaging techniques. By the time of the submission of the study plan, a more specific goal was chosen: to investigate methods for efficient beamforming, which make it possible to fit a large number of channels on a single integrated circuit. The use of oversampled analog-to-digital (A/D) converters was identified as an attractive concept, leading to the development of very compact beamformers.

During the Ph.D. study, the following papers were published:

- B. G. Tomov and J. A. Jensen. A new architecture for a single-chip multi-channel beamformer based on a standard FPGA. In *Proceedings of the IEEE Ultrasonics Symposium*, volume 2, pages 1529-1533, 2001.
- B. G. Tomov and J. A. Jensen. Delay generations with reduced memory requirements, in Proceedings of SPIE Vol. 5035 *Medical Imaging 2003:Ultrasonic Imaging and Signal Processing*, edited by William F. Walker, Michael F. Insana, (SPIE, Bellingham, WA, 2003) pages 491-500.
- B. G. Tomov and J. A. Jensen. Compact FPGA-based beamformer using oversampled 1-bit AD converters”, In *IEEE Transactions on Ultrasonics, Ferroelectrics, and Frequency Control”*, Submitted for publication, 2003.

Their content is given in the appendices.

The incentive for the present work was the aspiration for compact and inexpensive scanners, which I and my adviser Jørgen Arendt Jensen shared. Three years ago, ultrasound scanners were expensive and bulky machines, and portable scanners were not on the market yet. Prof. Jensen had the vision of making the ultrasound diagnostic devices as common as the stethoscopes. Although one should have certain basic training in order to be able to use such a device and make a correct diagnosis, the presence of inexpensive scanners on the market will be beneficial for the patients in the long run.

Oversampled data converters - both A/D and D/A, have proven themselves in audio and telecommunication. Their use, along with other technological improvements, has facilitated the wide spread of high-quality data conversion, leading to affordable Hi-Fi audio and inexpensive communications. What makes the oversampled converters so wide spread is their suitability for CMOS implementation. They can be implemented along the digital logic on a chip, thus enabling a single-chip devices to interface the analog environment. It can be expected that in a few years multiple delta-sigma modulators on a single chip will be mass-produced and will be used in ultrasound scanners, bringing simplified connections and beamformation.

The limiting factor for the use of oversampled converters is the necessary high oversampling ratio, which, together with the complexity of the modulators, determines the quality of the conversion. This is the reason why there are not many examples of oversampled converters for video signals and higher frequency signals.

This thesis describes my research in oversampled beamformers and other means for achieving compact beamformation. I hope that it is a useful reading and it is a good base for further research in that area.

Acknowledgments

My adviser, prof. Jørgen Arendt Jensen, is the person who made this work possible. I am deeply grateful to him for his guidance, patience and understanding. His suggestion that I get acquainted with oversampled converters led to the choice of the present research area, which has been interesting and exciting. His idea for sparse sample processing made it possible to use FIR filters for sample reconstruction, thus achieving high image quality. On numerous occasions, I had the privilege to learn from his example the proper scientific research practices. I highly appreciate the opportunity to work with him.

I am grateful to my advisers Jens Sparsø and Erik Bruun for their care and attention through my study.

I would like to thank all my colleagues at the Center for Fast Ultrasound Imaging for creating a helpful and positive environment. In particular I would like to thank:

- my colleague from the Technical University of Sofia and the Radar school in the army, Svetoslav Ivanov Nikolov, for presenting to me the opportunity to study as a Ph.D. student at CFU and encouraging me to apply for the position. During these years, he helped me with technical expertise (Linux, Matlab and programming) and inspiring discussions on ultrasound imaging. He also kindly donated the LaTeX style for the present thesis. He has been a very good friend.
- Peter Munk, with whom we worked on the experimental sampling system RASMUS. Apart form his kind and helpful attitude during his stay at the Center, it was an enjoyable experience for me to work in a team with a person as competent and as dedicated as him.
- Malene Schlaikjer, for helping me with many practical aspects of my study and residence in the well organized country of Denmark.
- Thanassis Misaridis, for being a friendly and cheering co-worker.
- Kim Løkke Gammelmark, for being a great officemate and a helpful colleague.

- Henrik Møller Pedersen, for being very helpful and co-operative during my first months at the Center for Fast Ultrasound Imaging.
- Paul David Fox, Jens Vilhjelm and Kaj-Åge Henneberg, for their cooperation on various work-related occasions and their friendly attitude.

I would also like to thank our system administrator Henrik Laursen and our hardware specialist Benny Johansen, for being very helpful and quick with resolving software and hardware issues.

During the testing and the debugging of the ultrasound sampling system RASMUS I had the opportunity to work with dedicated and inspiring people like Martin Hansen, Ole Holm, Henrik Bendsen, Lars Joost Jensen and Kim Gormsen from I/O Consulting A/S, and I would like to thank them for that experience.

I would like to thank Villy Brænder from B-K Medical A/S for his support and cooperation in the recent months.

Last, but not least, I would like to thank my wife, Rayna Georgieva, for her loving and support through these years.

This work was made possible thanks to financial support from the Danish Science Foundation (grants 9700883 and 9700563), from B-K Medical A/S, Herlev, Denmark, from the Thomas B. Thrige Center for Microinstruments, and from the Danish Research Academy.

List of Figures

1.1 Illustration of the principle of ultrasound imaging. 1
1.2 A-mode system architecture. 3
1.3 M-mode system architecture. 3
1.4 Real-time B-mode system architecture. 4
1.5 Multi-element transducers: Linear array (left) and phased array(right). The beam positions are shown with gray dashed line, and the spatial extent of one beam is shown with black line. 5
1.6 Triplex mode image, showing B-mode image, spectral Doppler (bottom graphics) and color flow map of the carotid artery (image courtesy of B-K Medical A/S). 6
1.7 Analog demodulation module. 7

2.1 Transmission and reflection of a plane wave propagating obliquely to medium border. 14

3.1 Continuous linear aperture and its response to a propagating continuous plane wave (aperture smoothing function). 16
3.2 Directivity pattern of a continuous linear aperture. 17
3.3 Aperture smoothing function of an array of omnidirectional sensors. 18
3.4 Grating lobes generation. Isophase surfaces spaced at 2π are drawn in gray. . . 18

3.5 Directivity pattern of a 3λ-spaced 12-element array with no gaps between elements and with 15 % gaps. The array response is shown in gray and the sensor element response is shown in black in the upper plots. The lower plots show the resulting response. 19

3.6 Angular resolution (angle of the first zero in the directivity pattern) of an array with size 32λ, given as a function of angle of incidence of the incoming wave. . 21

3.7 Illustration of near field (ultrasound) and far field (radar). 21

3.8 Focusing geometry 22

3.9 Analog signal transformations in an ultrasound imaging system. 25

3.10 Practical limitations of the beamforming. 26

3.11 Setup for calculating the delay after which a channel could take part in the beamforming. 27

3.12 Fixed focus setup (left) and multiple receive focal zones (right). The shape of the transmitted wave at different depths is illustrated by black arcs and the expected waveforms (summed coherently in the imaging system) are shown in gray. 28

3.13 Digital beamformer architecture 28

3.14 Pulse-echo fields for different beamforming techniques 31

3.15 Point spread functions for depths corresponding to F-numbers of 1, 2, and 4. The fixed-focus case is drawn with dashed line, the dynamic receive focusing is represented by black line, and the STA is shown with gray line. 32

3.16 Point spread functions for depths corresponding to F-numbers of 6, 8, and 10. The fixed-focus case is drawn with dashed line, the dynamic receive focusing is represented by black line, and the STA is shown with gray line. 33

3.17 PSF widths: fixed-focus is shown with continuous line, dynamic focus in receive is shown with dashed line, and STA is shown with dotted line. 34

4.1 Image line positions in different imaging techniques. 36

4.2 Delay calculation geometry 37

4.3 Delay profiles for center element (gray) and an element (black) situated at 8 λ away from the center element. 38

4.4 Index error and delta-encoded index information for target index resolution of T_s. 39

4.5 Index error and delta-encoded index information for target index resolution of $\frac{T_s}{4}$. 40

4.6 Piecewise-linear approximation of a delay curve. 41

4.7 Piecewise-linear delay generator. 41
4.8 Delay calculation geometry for the LUCS delay generator. 44
4.9 LUCS delay generator. 44

5.1 Quantization of a discrete analog sinusoidal signal (gray dots) results in coarse representation (black dots on the upper plot). The introduced quantization error, scaled up twice, is shown on the lower plot. 49
5.2 Assumed probability density function of the quantization error for an ”active” (rapidly varying) input signal. 49
5.3 Assumed spectral density of the quantization noise. By filtering out the noise that lies outside the frequency band of interest, the noise power in the quantized signal is diminished. 51
5.4 Noise-shaping modulator architecture 52
5.5 First order delta-sigma modulator 53
5.6 Noise transfer functions for oversampling only (dash-dotted) and first-order noise-shaping (solid line) A/D converters. The signal transfer function is constant one (dotted line). The level of the oversampling only quantization noise and the f_0 is shown for OSR = 4. 54
5.7 Second order delta-sigma modulator 55
5.8 Noise transfer functions for first-order noise-shaping (solid line) and second-order (dashed line) delta-sigma modulators. The signal transfer function is constant one (dotted line). 55
5.9 Theoretic SQNR curves for oversampling only (dash-dotted), first-order noise-shaping (solid line), and second-order noise-shaping (dashed line) A/D converters. 56

6.1 Block diagram of an oversampled beamformer. 59
6.2 Modified modulator structure for compensating of delay increase 60
6.3 Modified modulator structure for compensating of delay decrease 61
6.4 Illustration of delay profile coincidence with data values on different channels . 61
6.5 Block diagram with of a oversampled beamformer utilizing non-uniform sampling clock 62
6.6 Signal processing of the proposed beamformer, illustrated with 4 channels . . . 64

6.7 DSM output spectrum (gray) with frequency response of the matched filter (black) for OSR=20. 65
6.8 Simulated PSF: classic beamforming (grey), DSM beamforming (black) for depths of 1,3,5, and 7 cm. 70
6.9 Simulated PSF: classic beamforming (grey), DSM beamforming (black) for depths of 9,11,13, and 15 cm. 71
6.10 Velocity profiles obtained using different numbers of shots. The real velocity profile is drawn with dotted line. The flow estimate from conventional beamformed data is drawn in gray. The flow estimate from DSM beamformed data is drawn in black. 72
6.11 Image created using classic phased array beamforming and DSM phased array beamforming. Dynamic range: 60 dB 73

7.1 Sparse sampling architecture layout 75
7.2 Writing and reading form the sample buffer 76
7.3 Delay generation logic 77
7.4 Filter block with 4 parallel data paths 79

A.1 Signal processing of the proposed beamformer, illustrated with 4 channels . . . 84
A.2 Delay calculation geometry 85
A.3 Beamformer architecture 86
A.4 Frequency response of perfect matched filter (solid line) a shortened one (dashed line), along with typical DSM output spectrum (gray). 88
A.5 Simulated PSF: classic beamforming (solid line), ideal matched filter (dashed line), shortened filter (grey line). 88
A.6 Images created with classic beamforming and with the suggested beamforming at different OSR. The dynamic range is 40 dB 90

B.1 Image line positions in different imaging techniques. 93
B.2 Delay calculation geometry 94
B.3 Delay profiles for center element (gray) and an element (black) situated at 8 λ away from the center element. 95
B.4 Limitations to the element contribution to the beamforming. 97

B.5 Setup for calculating the delay after which a channel can contribute to the beamforming of a given image line. 97

B.6 Delay generation geometry for the LUCS generator. 99

B.7 LUCS delay generator. 99

B.8 Piecewise-linear approximation of a delay curve. 100

B.9 Piecewise-linear delay generator. 101

C.1 Beamformer architecture for dynamic receive focusing 105

C.2 Signal processing of the proposed beamformer, illustrated with 4 channels. The analog echo signals are modulated into one-bit streams. Corresponding bit-stream sequences form the different channels are added, and the result is filtered to produce in-phase and quadrature components. 110

C.3 DSM output spectrum (gray) with frequency response of the matched filter (black) for OSR=20. 111

C.4 Simulated PSF: classic beamforming (grey), DSM beamforming (black) for depths of 1,3,5, and 7 cm. 119

C.5 Simulated PSF: classic beamforming (grey), DSM beamforming (black) for depths of 9,11,13, and 15 cm. 120

C.6 Velocity profiles obtained using different numbers of shots. The real velocity profile is drawn with dotted line. The flow estimation on conventional beamformed data is drawn in gray. The flow estimation on DSM beamformed data is drawn in black. 121

C.7 Image created using classic phased array beamforming and DSM phased array beamforming. Dynamic range: 60 dB 122

C.8 Beamformer structure 122

C.9 Illustration of the writing and the reading from the sample buffer. 123

C.10 Filter block structure 123

List of Tables

3.1 Parameters for the obtained directivity patterns using different beamforming techniques . . . 30

4.1 Parameters for the delay generation approximation approaches comparison . . 46
4.2 Implementation results for delay generation approaches, per channel 46

6.1 Digital recoding techniques for inserting a zero sample 60
6.2 Digital recoding techniques for inserting a sample in half 60
6.3 Target beamformer parameters. 66
6.4 Simulation parameters 67
6.5 Simulated flow parameters 68

7.1 Parameters for the implementation 74
7.2 Resource utilization results 80

B.1 Parameters for the delay generation approximation approaches comparison . . 102
B.2 Implementation results for delay generation approaches, per channel 102

C.1 Target beamformer parameters 112
C.2 Simulation parameters 114
C.3 Simulated flow parameters 114
C.4 Target implementation parameters 115

CHAPTER

ONE

Introduction

The use of ultrasound in medicine as visualization tool dates back to the early 50s. The first imaging systems were working with one transducer element. Since then, the capabilities of ultrasound imaging devices have increased a lot, due to the advances in electronics and signal processing. Nowadays, two-dimensional imaging and color maps of the blood velocity are common features of the scanners, with 3-D (volume) imaging becoming mainstream. This chapter will introduce the principles along which the ultrasound imaging systems operate and some distinct modes of operation, which were characteristic for the generations of the scanners at the time. An overview of applications and the drawbacks of the most popular medical imaging techniques will be presented.

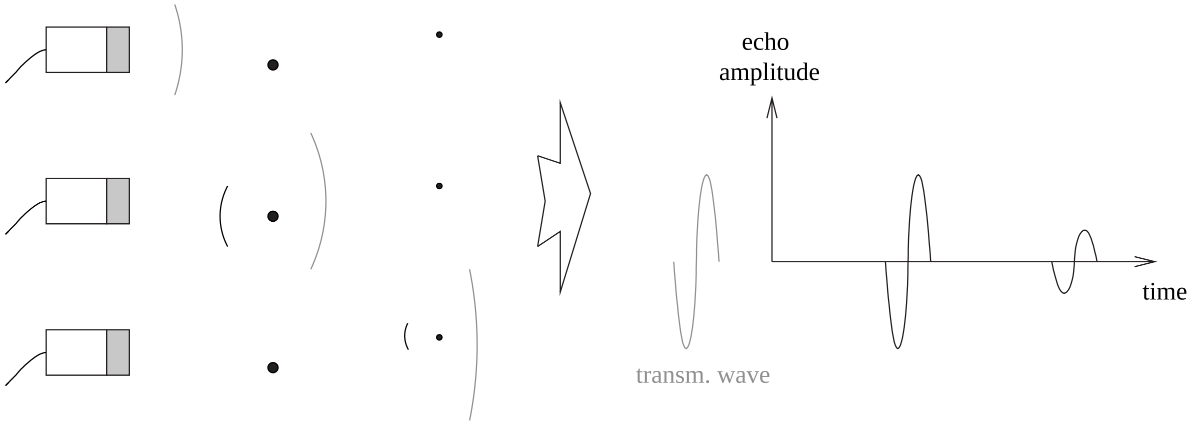

Figure 1.1: Illustration of the principle of ultrasound imaging.

1.1 Ultrasound imaging principle

Ultrasound is the sound at frequencies above the human hearing range, i.e. above 20 kHz. The propagation of the ultrasound is described as a wave propagation. The ultrasound waves can be directed, or even focused at a specific focal point, given that the medium is homogeneous enough, as is the case with air and water.

In an imaging system, electrical impulse excites a piezoelectric transducer which creates pressure changes in its neighboring medium. As the transmitted wave propagates, any irregularities in the medium create reflected waves, which are then detected by the transducer. The obtained trace carries information about the position and the strength of reflectors (also called *scatterers*). That is illustrated in Fig. 1.1. During its propagation, the wave is attenuated not only because of the distance, but also due to absorption in the medium. In human body that attenuation is very strong and has to be compensated for. This is done by using amplifiers whose amplification coefficient is minimal at the time of transmit and increases with time. The process is called time gain compensation (TGC). The resolution that can be achieved with such an imaging system depends on the impulse that is used. In general, the higher its frequency is, the better resolution is achieved. At present, general purpose imaging systems operate in the range 3 - 12 MHz.

1.2 Medical ultrasound systems evolution

This section provides an overview of the generations of the ultrasound imaging systems from their early days to present time. The source used is [1]. In accordance to the subject of this thesis, pulsed wave systems are discussed, and not continuous wave systems, which are thoroughly described in the mentioned above source.

The first ultrasound imaging systems operated in the so called A-mode (Amplitude). The structure of such a system is shown in Fig. 1.2. They worked pretty much like an oscilloscope, showing the logarithmically compressed magnitude of the echo signal against time (depth). The displayed information could hardly give an insight into structures, but motion was easy to perceive, as the refresh rate of the traces was very high.

For visualizing motion, M-mode (Motion) systems were developed. In these, the amplitude of the echo signal is represented by brightness, the vertical axis represents the depth, and the traces of consecutive interrogations in the same direction are displayed next to each other in the horizontal direction (See Fig. 1.3).

An evolution step following the M-mode systems were the static B-mode (Brightness) systems, in which the different traces in the image corresponded to different positions of the transducer. The correspondence was achieved by keeping track of the transducer position. A disadvantage of that concept is the susceptibility to motion blur and the long acquisition time.

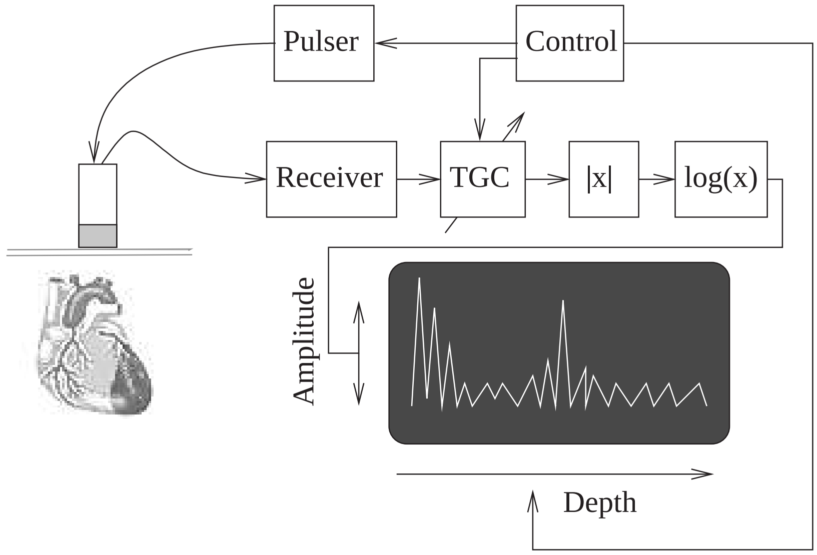
Pulser
Control
Receiver
TGC
|x|
log(x)
Amplitude
Depth

Figure 1.2: A-mode system architecture.

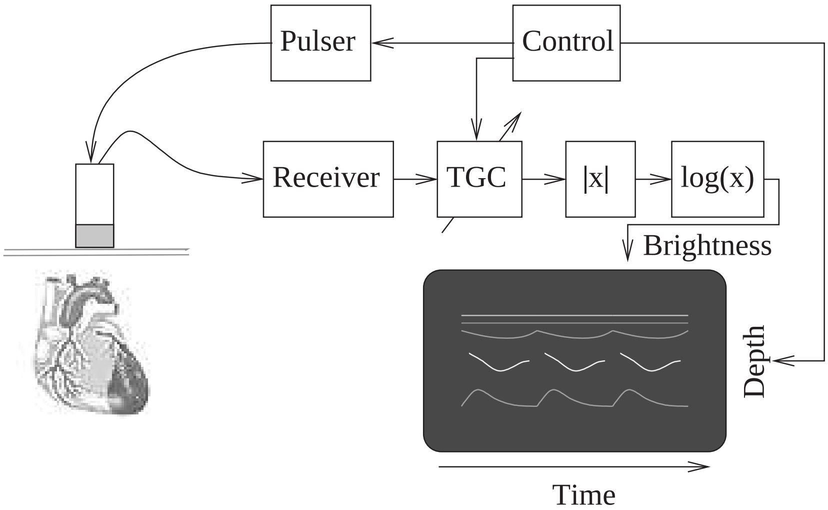
Pulser
Control
Receiver
TGC
|x|
log(x)
Brightness
Depth
Time

Figure 1.3: M-mode system architecture.

The modern scanners operate in real-time B-mode, in which several images per second are displayed on a screen. In case of a single element transducer with rotating crystal, the covered area has a sector shape and scan conversion is necessary before display. The scan conversion places the trace data in a rectangular matrix in such a way that the geometry of the interrogated area can be shown on the display without distortion. Also, interpolation is done between the trace data so that the displayed image has no gaps between the trace positions. A real-time B-

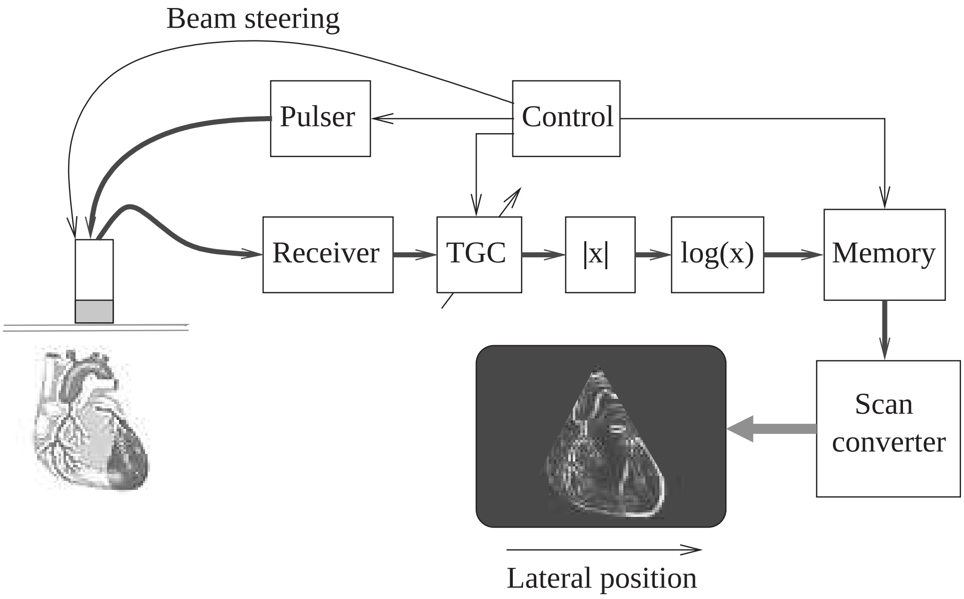

Figure 1.4: Real-time B-mode system architecture.

mode system architecture is shown in Fig. 1.4. The data paths in transmit and receive are shown with thicker line to indicate that all modern scanners have many independent channels and utilize multi-element transducers. There are two types of such transducers: linear arrays and phased arrays (See Fig. 1.5). Linear array transducers can be flat or convex, and are operated by using several adjacent elements at a time in transmit and receive. A set of parallel lines is obtained. Before display, interpolation between the lines is done in the scan conversion module. In phased arrays, all elements are used together and beam steering is performed by properly delaying the transmissions on the different elements. With the introduction of multi-element transducers, electronic focusing became necessary. It will be discussed in Chapter 3.

1.3 Blood velocity estimation

Blood is not a homogeneous fluid, and as aggregates of blood cells move, the position in time (after the moment of the transmission) of their echo signal changes. There exist two techniques for presenting information for the blood flow:

- Sonogram presentation / spectral Doppler.
- Color flow map.

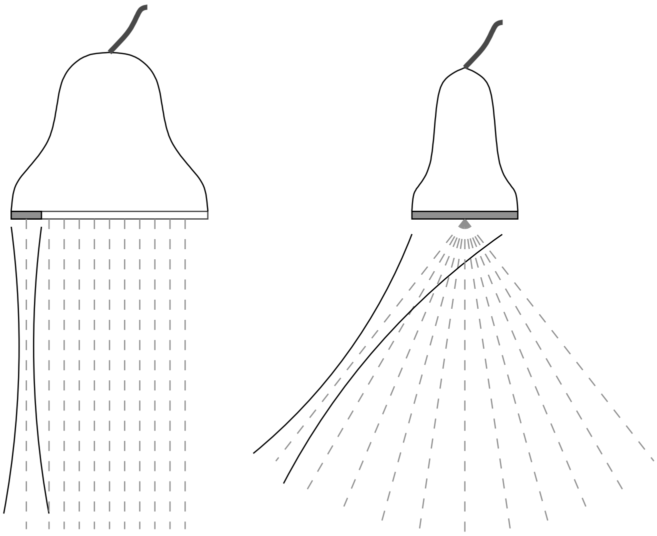

Figure 1.5: Multi-element transducers: Linear array (left) and phased array(right). The beam positions are shown with gray dashed line, and the spatial extent of one beam is shown with black line.

An excellent source of information about the blood velocity estimation techniques and their implementation is [1]. Here, an overview of the techniques will be given.

1.3.1 Sonogram / Spectral Doppler

The echo signal contains a sum of echoes from different scatterers. Any value (sample) in that signal is influenced by scatterers which occupy a depth range corresponding to the spatial extent of the transmitted waveform. The change in that signal value from one interrogation to the next is due to the movements of all contributing scatterers.

The sonogram presentation is done by sending the signal values corresponding to specific depth in the same direction, to audio amplifier and loudspeaker. The produced sound represents the nature of the movement of the contributing scatterers: for static tissue/blood, the signal value does not change and no sound will be produced; for fast moving scatterers, the sound contains relatively high frequencies; for slowly moving scatterers, the sound contains relatively low frequencies. The sampling frequency in this case is the frequency with which new echo traces are generated (called also *pulse repletion frequency*, f_{prf}). Frequency components above half of the sampling frequency get aliased, therefore the pulse repetition frequency is usually adjusted depending on the expected and the observed blood velocity.

Graphic representation of the same information is done by displaying the discrete Fourier transformation of the signal in consecutive time instances, in a fashion resembling M-mode imaging

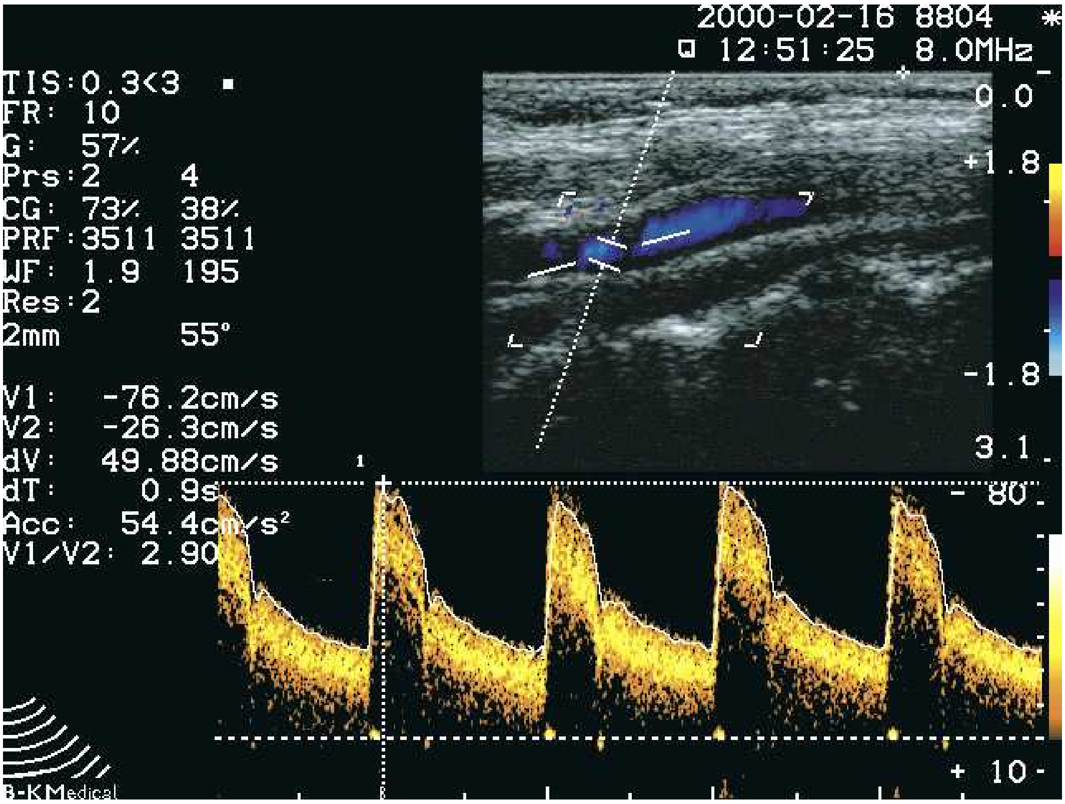
2000-02-16 8804
12:51:25 8.0MHz
TIS:0.3<3
FR: 10
G: 57%
Prs:2 4
CG: 73% 38%
PRF:3511 3511
WF: 1.9 195
Res:2
2mm 55°
V1: -76.2cm/s
V2: -26.3cm/s
dV: 49.88cm/s
dT: 0.9s
Acc: 54.4cm/s²
V1/V2: 2.90
0.0
+1.8
-1.8
3.1
-80
+10
1
B-KMedical

Figure 1.6: Triplex mode image, showing B-mode image, spectral Doppler (bottom graphics) and color flow map of the carotid artery (image courtesy of B-K Medical A/S).

(See Fig 1.6). The brightness represents the amplitude of the corresponding spectral component. The name ”Spectral Doppler” is used by convention. It is an incorrect description of this technique, since Doppler effect is never utilized with pulsed systems and is an artifact at most.

1.3.2 Color flow map

Color flow map is a blood velocity visualization technique, in which the velocity is represented by color. Velocity estimates are obtained for a grid of points and a correspondingly colored map is presented on top of the B-mode image. There are two techniques that can provide the necessary velocity estimates:

- Phase-shift estimation (autocorrelation)
- Time-shift estimation (cross-correlation)

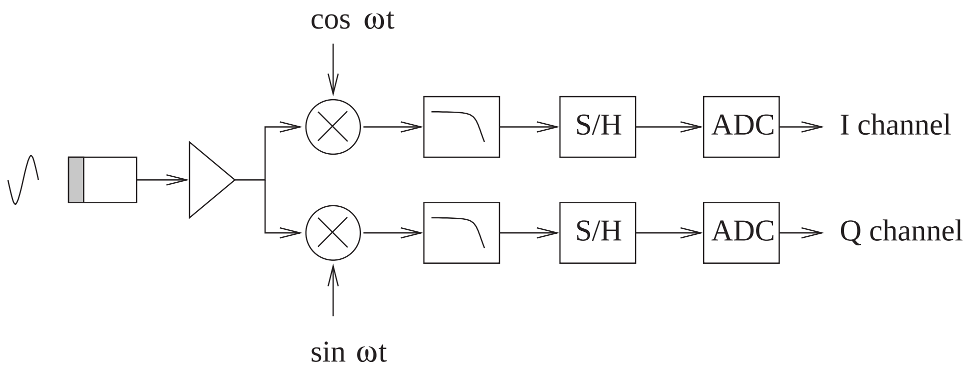

Figure 1.7: Analog demodulation module.

Phase-shift estimation

Phase-shift estimation utilizes the phase difference between the echo signal values corresponding to two consecutive interrogations in the same direction. The velocity estimate is proportional to the phase shift. For improving the precision of the estimates and diminishing the effect of the noise in the signal, several (4, 8, 16 or more) interrogations in the same direction are made, thus providing a number of phase difference estimates, the mean value of which is used further. Velocities which cause phase shifts outside the range $(-\pi, \pi)$ are aliased, therefore the pulse repetition frequency in scanners is made adjustable. Since the echo signals from the tissue are much stronger than the ones from the blood, the former have to be removed by applying stationary echo cancelling (subtraction of the consecutive echo signals from the same direction).

The phase can be calculated from the values of the in-phase and the quadrature component of the echo signal. An analog solution that provides them is shown in Fig. 1.7. It should be noted that this approach is narrow-band, i.e. it is valid only for the frequency ω and introduces error for other frequencies. In digital systems, Hilbert transformation of the sampled echo signal produces the quadrature component.

Time-shift estimation

The time shift estimation correlates a trace segment with a number of trace segments chosen around the same depth, from a previous interrogation in the same direction. The offset of the best match (at which the cross-correlation has a maximum) is taken as an estimate of the movement between the two interrogations. This technique has the disadvantage that it is very computationally intensive. On the other hand, it does not exhibit aliasing.

1.4 Comparison with CT and MR imaging

1.4.1 Computed tomography

Computed tomography (CT) imaging, also known as ”CAT scanning” (Computed Axial Tomography), was developed in the early to mid 1970s. It provides images of soft tissue, bone and blood vessels. CT allows direct imaging and differentiation of soft tissue structures, such as liver, lung tissue, and fat. CT is especially useful in searching for large space occupying lesions, tumors and metastases and can not only reveal their presence, but also the size and spatial location. CT imaging of the head and brain can detect tumors, show blood clots and blood vessel defects, show enlarged ventricles (caused by a build up of cerebrospinal fluid) and image other abnormalities such as those of the nerves or muscles of the eye.

Drawback:

> Of the approximately 600,000 abdominal and head CT examinations annually performed in children under the age of 15 years (in USA), a rough estimate is that 500 (approximately 1/10th of a percent) of these individuals might ultimately die from cancer attributable to the CT radiation. *David Brenner, Center for Radiological Research at Columbia University*

1.4.2 Magnetic resonance imaging

Magnetic Resonance (MR) Imaging (also know as MRI) was initially researched in the early 1970’s and the first MR prototypes were tested on clinical patients in 1980. MR imaging was cleared for commercial availability by the Food and Drug Administration (FDA) in 1984. MR provides very good contrast between different tissues with similar densities, for instance gray and white brain matter, and is used for imaging of :

- the brain, vessels of the brain, eyes, inner ear
- the neck, shoulders, cervical spine and blood vessels of the neck
- the heart, aorta and coronary arteries
- the thoracic and lumbar spine
- the upper abdomen, liver, kidney, spleen, pancreas and other abdominal vessels
- the pelvis and hips, male and female reproductive system, and bladder
- the musculoskeletal skeletal system including joints such as the shoulder, knee, wrist, ankles and feet

MR is a powerful tool for finding and diagnosing many forms of cancer.

Drawbacks:

- many people cannot safely be scanned with MRI (for example, because they have pacemakers), or because they are claustrophobic
- the machines are very noisy
- MRI scans require patients to hold very still for extended periods of time
- Orthopedic hardware (screws, plates, artificial joints) in the area of a scan can cause severe artifacts (distortions) on the images.
- MRI systems are very expensive to purchase, and therefore the exams are also very expensive.

1.4.3 Ultrasound imaging

Ultrasound imaging (also called ultrasound scanning or sonography) is a relatively inexpensive, fast, portable and radiation-free imaging modality. Ultrasound is excellent for non-invasive imaging and diagnosing a number of organs and conditions. Modern obstetric medicine (for guiding pregnancy and child birth) relies heavily on ultrasound to provide detailed images of the fetus and uterus. Ultrasound can show fetal development and body functions like breathing, urination, and movement. Ultrasound is also extensively used for evaluating the kidneys, liver, pancreas, heart, and blood vessels of the neck and abdomen. Ultrasound can also be used to guide fine needle for tissue biopsy to facilitate sampling cells from an organ for lab testing (for example, to test for cancerous tissue).

Ultrasound imaging has an important role in the detection, diagnosis and treatment of heart disease, heart attack, acute stroke and vascular disease which can lead to stroke. Ultrasound is also being used more and more to image the breasts and to guide biopsy of breast cancer.

Medical ultrasound safety

No negative effects have been ever registered. Prolonged scan heats the transducer and causes discomfort to the patient. Also, the tissue around the transmit focal point is heated. In general, prolonged scanning of fetus head is not practiced.

CHAPTER

TWO

Ultrasound acoustics

As with any physical phenomenon, understanding the wave propagation in tissue makes it possible to design and build imaging systems that utilize it. This chapter considers the basic linear acoustics in medical ultrasound. The *wave equation* which governs the acoustic wave propagation, is shown. Its most widely used solutions are given. The phenomena encountered when an acoustic wave propagates in human tissue are considered. An introduction to the wavenumber-frequency space is given, as this concept is used in the next chapter.

2.1 Wave equation

The propagation of waves is described by the *wave equation*. For a spatiotemporal signal $s(\vec{x},t)$, where $\vec{x} \equiv (x,y,z)$ represents position, it is written as [2]:

$$\frac{\partial^2 s}{\partial x^2} + \frac{\partial^2 s}{\partial y^2} + \frac{\partial^2 s}{\partial z^2} = \frac{1}{c^2}\frac{\partial^2 s}{\partial t^2} \tag{2.1}$$

In this equation, the parameter c is the signal propagation speed in the media.

2.2 Solutions to the wave equation

In this section, the most used solutions to the wave equation will be shown.

2.2.1 Plane wave

One way of solving the wave equation is to assume a separable solution, i.e.

$$s(x,y,z,t) = f(x)g(y)h(z)p(t) \tag{2.2}$$

A function of that type is (see Section 2.2 in [2]) the complex exponential function

$$\dot{s}(x,y,z,t) = A\exp\left(j(\omega t - (k_x x + k_y y + k_z z))\right), \tag{2.3}$$

where A is a complex constant and k_x, k_y, k_z and ω are real constants with $\omega \geq 0$. Substituting this form in the wave equation yields

$$k_x^2\dot{\Phi}(x,y,z,t) + k_y^2\dot{\Phi}(x,y,z,t) + k_z^2\dot{\Phi}(x,y,z,t) = \frac{\omega^2}{c^2}\dot{\Phi}(x,y,z,t) \tag{2.4}$$

$$\Downarrow$$

$$k_x^2 + k_y^2 + k_z^2 = \frac{\omega^2}{c^2} \tag{2.5}$$

The above constraint defines the *plane waves*.

This solution is known as a monochromatic plane wave and for a given point in space with coordinates (x_0,y_0,z_0) it becomes:

$$\dot{\Phi}(x_0,y_0,z_0,t) = \dot{F}\exp\left(j[\underbrace{\omega}_{\text{frequency}} t - \underbrace{(k_x x_0, + k_y y_0 + k_z z_0)}_{\text{phase}}]\right) \tag{2.6}$$

The observable signal at (x_0,y_0,z_0) is a complex exponential with frequency ω. The wave is a *plane wave* because the phase is the same at the points lying on the plane given by $k_x x + k_y y + k_z z = C$, where C is a constant. The distance along the propagation direction between two points that have the same phase is called *wavelength* and is equal to:

$$\lambda = \frac{c}{f}. \tag{2.7}$$

The wave number and the wavelength are related through the equation:

$$k = \frac{2\pi}{\lambda} \tag{2.8}$$

2.2.2 Spherical wave

When the wave equation is solved in spherical coordinates, an assumption that the solution exhibits spherical symmetry greatly simplifies the equation ([2]):

$$\frac{\partial^2}{\partial r^2}(r\dot{\Phi}) = \frac{1}{c^2}\frac{\partial^2}{\partial t^2}(r\dot{\Phi}). \tag{2.9}$$

Solutions to this equation are the *spherical* waves, which in complex form are given by:

$$\dot{\Phi}(r,t) = \frac{\dot{F}}{r} \exp j(\omega t - kr), \tag{2.10}$$

where $\dot{F}$ is a complex amplitude, r is the distance traveled by the wave and k is the wave number:

$$k^2 = \frac{\omega^2}{c^2}. \tag{2.11}$$

The waves can be either diverging (going away from the source) or converging. The diverging wave can be expressed by:

$$\dot{\Phi}(r,t) = \frac{\dot{F}}{r} \exp(j\omega(t - \frac{r}{c})). \tag{2.12}$$

2.3 Wavenumber-frequency space (*k*-space)

Using wavenumber-frequency representations of signals and ultrasound systems is a convenient analysis technique. It will be used for gaining understanding of the focusing and beamforming further in the thesis, and therefore, some notations will be given here.

Consider a continuous sinusoidal plane wave with a wavelength λ, propagating in a direction defined by a vector $\vec{x} = (x, y, z)$ (in Cartesian coordinates) with a magnitude of 1. The wave can be represented by a vector $\vec{k}$ which incorporates all the necessary information about it, in the following way:

$$\begin{aligned} \vec{k} &= (k_x, k_y, k_z) \\ k_x &= x\frac{2\pi}{\lambda} \\ k_y &= y\frac{2\pi}{\lambda} \\ k_z &= z\frac{2\pi}{\lambda} \end{aligned} \tag{2.13}$$

This vector is called *wavenumber vector* and its magnitude $\frac{2\pi}{\lambda}$ represents the spatial frequency of the wave (number of wave periods per unit distance). Its direction is the same as that of $\vec{x}$.

2.4 Propagation in tissue

In medical ultrasound, pulses with central frequency of 3MHz and above are used. The electrical signals are transformed into pressure waves using piezo-electrical transducers. As the pressure waves propagate in the human tissue, echoes are generated due to two phenomena: reflection and scattering.

2.4.1 Reflection

Reflection occurs at the border of two regions with different acoustic impedances. For a monochromatic wave the relation between particle velocity u and the pressure p is given through the acoustic impedance Z [3]:

$$u = \frac{p}{Z}. \tag{2.14}$$

For a plane progressing wave the impedance is:

$$Z = \rho_0 c. \tag{2.15}$$

The situation of reflection and transmission of a plane wave propagating obliquely to the reflecting surface is shown in Figure 2.1. If the first medium has a speed of sound c_1 and second medium c_2, then the angles of transmitted and reflected waves are described by Snell's law:

$$\frac{c_1}{c_2} = \frac{\sin\theta_i}{\sin\theta_t}, \tag{2.16}$$

where θ_i and θ_t are the angles of the incident and transmitted waves, respectively. If the angles are measured with respect to the normal vector to reflecting surface then:

$$\theta_r = -\theta_i. \tag{2.17}$$

The pressure amplitude transmission coefficient is given by:

$$\frac{p_t}{p_i} = \frac{2Z_2\cos\theta_i}{Z_2\cos\theta_i + Z_1\cos\theta_t}, \tag{2.18}$$

where Z_1 and Z_2 are the acoustic impedances of the first and the second media, respectively, and p_i and p_t are the respective amplitudes of the pressure.

2.4.2 Scattering

Scattering is a physical phenomenon, in which small changes in density, compressibility and absorption give rise to wave, radiating in all directions (by [1]). What the scanners display is the scattering, which has been detected by the transducer. In fact, reflections are not desired, since their amplitude is too large compared to the scattering and they saturate the imaging system.

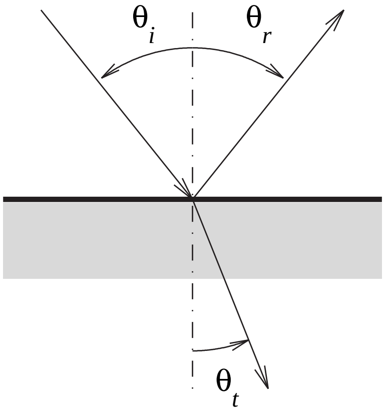

Figure 2.1: Transmission and reflection of a plane wave propagating obliquely to medium border.

The spatial pulse-echo response for a single scatterer corresponds to the convolution of the spatial impulse responses of the transmit and receive apertures [4]. This can be easily justified since a point can be represented as a delta function $\delta(x_p, y_p, z_p)$ and the system is assumed to be linear. In the rest of the dissertation the pulse-echo response of a point will be called *point spread function*. The point spread function can be in space $\mathbf{P}(x_p, y_p, z_p)$, or in space and time. In the latter case this usually represents a collection of the responses along a line of points.

There is a Fourier relation between the apodization of a focused transducer and the point spread function in the focus. The point spread functions must be defined on a spherical surface, so often they will be given as a function of angle.

In a real measurement situation, a group of scatterers is insonified. The wave reaches the scatterers and they start to vibrate, becoming omnidirectional sources of spherical waves (Rayleigh scattering). The scattering is assumed to be weak, i.e. a wave generated by a scatterer cannot be scattered again by another scatterer (Born approximation [3]). The medium is assumed to be linear and homogeneous, and the total response of the field is the sum of the responses of the individual scatterers.

2.4.3 Attenuation

The human tissue is a lossy medium and the ultrasound pulse is attenuated as it propagates in it. This attenuation is not accounted for in the linear wave equation and most of it is due to absorption. The attenuation can be approximated by expressing the losses in dB/(MHz·cm) [5], and is 0.5 to 1 dB/(MHz·cm) for most soft tissues. For fat, the attenuation is 1 to 2 dB/(MHz·cm) (source: [1]).

CHAPTER

THREE

Beamformation

In medical ultrasound, the images are created by sending an ultrasound pulse into the tissue and performing signal processing on the received echo signal. The geometry of the utilized electro-acoustical transformers (transducers) has a great impact on the image resolution. In this chapter, some of the basic transducer properties are described. For providing a focusing of the echo signals, a signal processing technique called beamforming is used in medical ultrasound. Its principles and its more widely used variants are presented.

3.1 Transducer properties

The active area of the modern transducers is made of continuous transducer elements, placed in line on a flat or convex surface. Transducer directivity properties can be analyzed in two steps: the first step is to consider the properties of the transducer elements, and the second is to consider the properties of the grid on which they are placed.

3.1.1 Directivity properties of finite continuous apertures

The transducer elements are continuous finite pressure sensors. Their response to an incoming continuous sinusoidal plane wave, expressed as a function of the wavenumber vector, is called *aperture smoothing function* (ASF). When the response is expressed as a function of angle of incidence, it is called *directivity pattern*.

As a primer, the simple case of a one-dimensional linear aperture with size D, situated along the axis x, is considered. Its response to a wave with a wavenumber vector $\vec{k}$ depends only on the component k_x of $\vec{k}$ ([2]):

$$W(\vec{k}) = \frac{\sin \frac{k_x D}{2}}{\frac{k_x}{2}} \tag{3.1}$$

An illustration of the ASF is shown in Fig. 3.1.

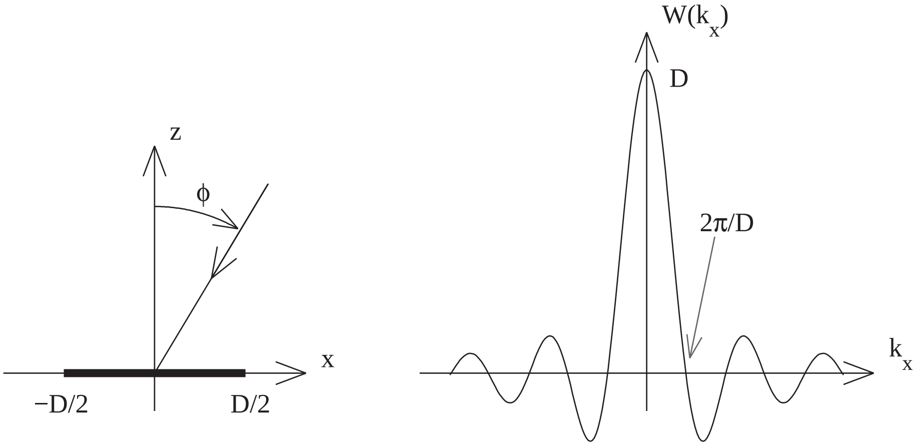

Figure 3.1: Continuous linear aperture and its response to a propagating continuous plane wave (aperture smoothing function).

The ASF can be transformed into a directivity pattern by using the fact that

$$k_x = -k \sin\phi \tag{3.2}$$

and replacing $k = \frac{2\pi}{\lambda}$ in equation (3.1). It becomes

$$W\left(\frac{-2\pi\sin\phi}{\lambda}\right) \equiv W'(\phi) = \lambda\frac{\sin(D'\pi\sin\phi)}{\pi\sin\phi}, \tag{3.3}$$

where $D' = \frac{D}{\lambda}$ is the normalized aperture. W' is a periodic function of ϕ with a period of π and is therefore only plotted for $-\pi/2 < \phi \leq \pi/2$ (Fig. 3.2).

The directivity pattern has zeros for angles in which $D'\sin\phi$ is integer. The first zero occurs at an angle

$$\phi_1 = \arcsin\frac{1}{D'}, \tag{3.4}$$

which indicates that, for larger aperture, the main lobe is narrower.

The sidelobes obstruct the detection of other signal sources and introduce artifacts into the image. The first sidelobe level lies at $\approx -20\log\frac{3}{2}\pi \approx -13.5$ dB relative to the main lobe and occurs at an angle $\phi_s \approx \arcsin\frac{3}{2D'}$.

3.1.2 Angular resolution concept

The ability of a sensor or an array of sensors to distinguish between two signal sources is very important for the imaging systems in general and the ultrasound imaging systems in particular.

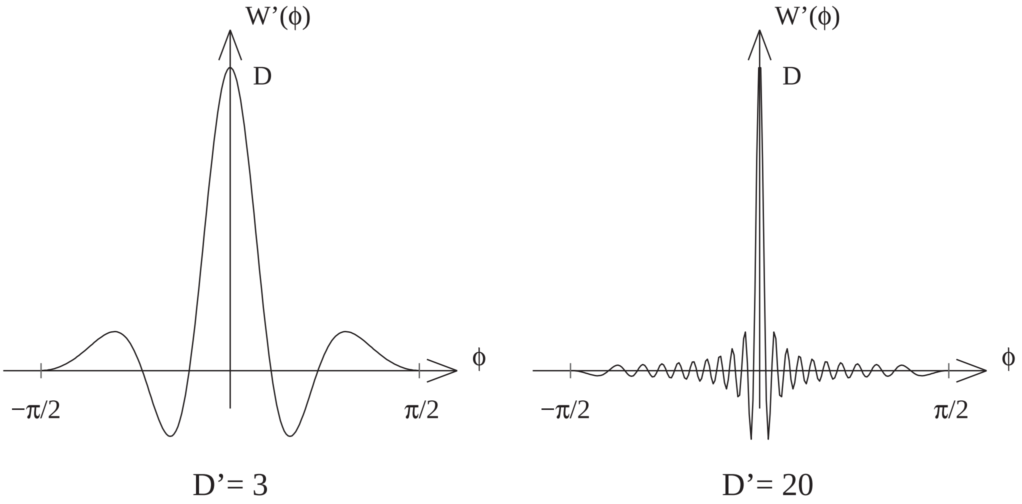

Figure 3.2: Directivity pattern of a continuous linear aperture.

In the current overview of apertures and arrays, the Rayleigh criterion for resolution will be used. It states that two incoherent plane waves are resolved if the mainlobe peak of aperture response to one of them falls on the first zero of the response to the other.

In medical ultrasound systems, the envelope of the echo signal is calculated, and is logarithmically compressed for display, therefore another approach is taken. It is based on the image of a single point source (point scatterer) which is called *point spread function* (PSF). The angular and the axial (along the beam) resolution are expressed as the PSF width at 6 dB below its peak (at half amplitude).

3.1.3 Directivity properties of arrays

The ASF of a regular linear array of omnidirectional sensors is described described by ([2]):

$$W(k) = \frac{\sin\frac{k_x M d}{2}}{\sin\frac{k_x d}{2}}, \tag{3.5}$$

where d is the sensor spacing (called *pitch*) along the axis x and M is the number of the sensors. The parameter k_x is the wavenumber vector component along the axis x. A plot of a 10-element sensor array ASF is shown in Fig. 3.3.

The maximums observed away from the main lobe are called grating lobes. They arise when the incidence angle of the arriving wave is such that the signal phases at the different sensors differ by full periods (see Fig. 3.4). In this case, the signals from all sensors add constructively. That

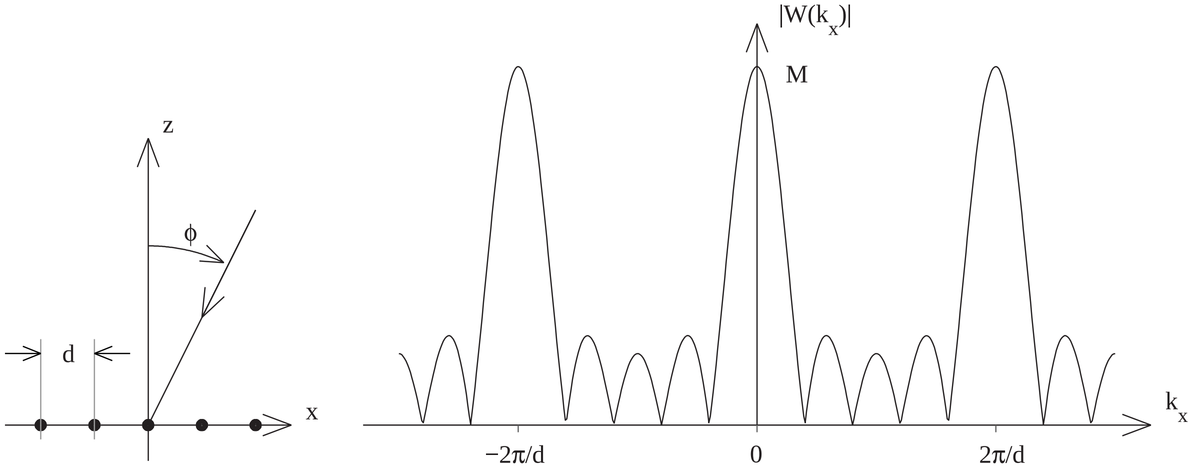

Figure 3.3: Aperture smoothing function of an array of omnidirectional sensors.

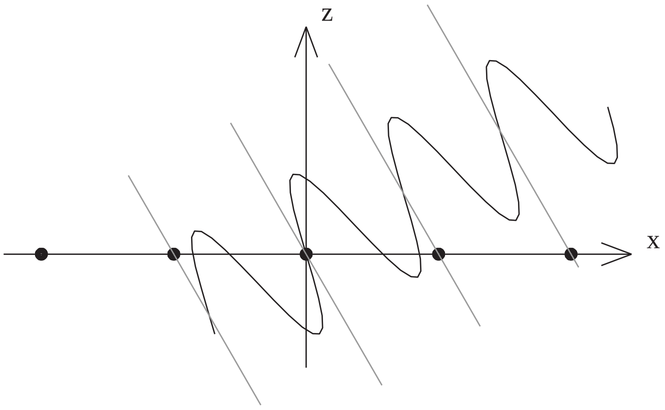

Figure 3.4: Grating lobes generation. Isophase surfaces spaced at 2π are drawn in gray.

phenomenon is called *aliasing* by analogy to the spectrum aliasing due to time undersampling in data conversion.

The first sidelobe occurs at $k_x = \frac{3\pi}{Md}$ and its relative level is $20\log\frac{M}{\sin\frac{3\pi}{M}}$. This relation shows that increasing the number of elements improves the directivity properties of the array.

The directivity pattern of an array can be derived using the same transformations as in the continuous aperture case. It is:

$$W\left(\frac{-2\pi\sin\phi}{\lambda}\right) \equiv W'(\phi) = \frac{\sin(Md'\pi\sin\phi)}{\sin(d'\pi\sin\phi)}, \tag{3.6}$$

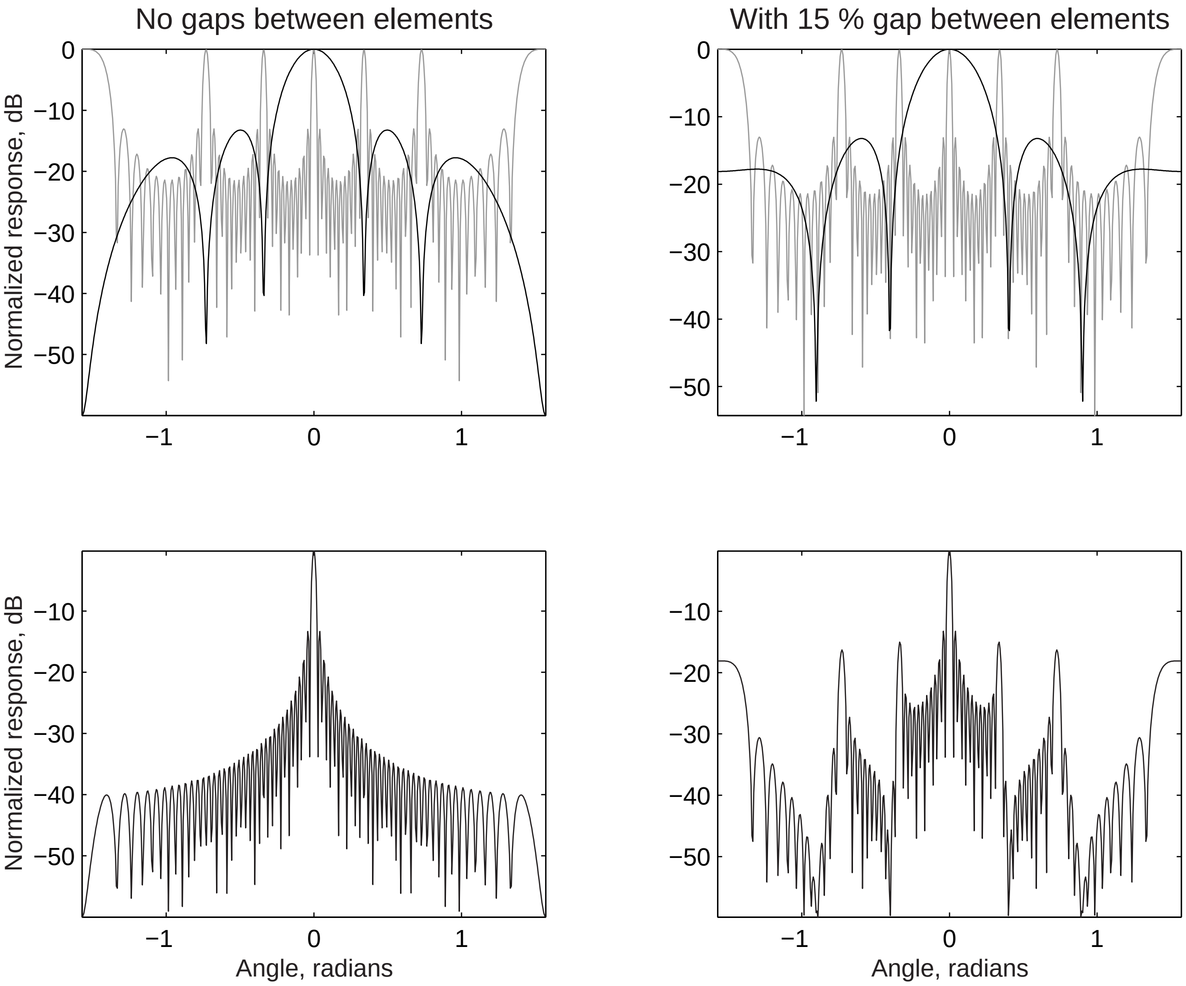

Figure 3.5: Directivity pattern of a 3λ-spaced 12-element array with no gaps between elements and with 15 % gaps. The array response is shown in gray and the sensor element response is shown in black in the upper plots. The lower plots show the resulting response.

where $d' = \frac{d}{\lambda}$ is the normalized inter-element distance.

3.1.4 Directivity properties of arrays of finite continuous sensors

The directivity properties of an array of finite continuous sensors are illustrated through an example (see Fig. 3.5), in which the a 12-element array with spacing of 3λ is considered. If the elements size is equal to the distance between the element centers (there are no gaps between the elements), then the zeros of the element response fall on the grating lobes of the array response. The resulting sensor array response is identical to that of a single element with size equal to the extent of the sensor array. In reality, the transducers have around 15 % gap (called *kerf*) between their elements, therefore they would suffer from grating lobes, if the transducer pitch allows for these to arise in the visible sector from $-\frac{\pi}{2}$ to $\frac{\pi}{2}$. For that reason, transducers are usually designed with pitch $\frac{\lambda}{2}$, which provides good directivity properties for the frequencies for which it will be used.

For suppressing the sidelobes, weighting coefficients are assigned to the signals produced by different array sensors. The outer sensors have lower weights assigned. This reduces the sidelobe level at the expense of widening the mainlobe.

3.1.5 Phased array angular resolution dependence on the incidence angle

The first zero in an array directivity pattern occurs at an angle $\phi_0 = \arcsin \frac{\lambda}{Md}$, therefore it can be concluded that the resolution improves with enlarging the spatial extent of the array . The quoted angle represents the angular resolution of the array for waves that arrive from the broadside of the array. When the directivity pattern has to be steered in other direction than the normal to the array, appropriate delays are applied to the sensor signals. In these cases, the apparent array size is smaller, and therefore the angular resolution is worse. A plot of the angular resolution on an array with spatial extent 32λ for angles up to $\frac{\pi}{3}$ is shown in Fig. 3.6.

3.2 Focusing

In general, focusing is the process of applying appropriate delays to a set of available sensor signals so that the incoming signal from a given direction or point source is amplified. The delays are chosen such that the sensor signals generated by a propagating isophase surface are summed coherently.

When the signal source is relatively far from the sensor array, using an assumption that the isophase surface is planar does not introduce significant error in the focusing. In such cases, it is said that the signal source is located in the *far field*. An example of such a situation is the conventional radar, where the distance to the signal source is much larger than the size of the sensor. When the described assumption is not acceptable, i.e. the isophase surface has to be regarded as spherical for achieving good focusing, the signal source is said to be located in the *near field*.

In ultrasound, the size of the transducer array is significant compared to the image depth, and the echoes from the region of interest have to be regarded as spherical waves.

An illustration of the concepts of near and far field is shown in Fig. 3.7.

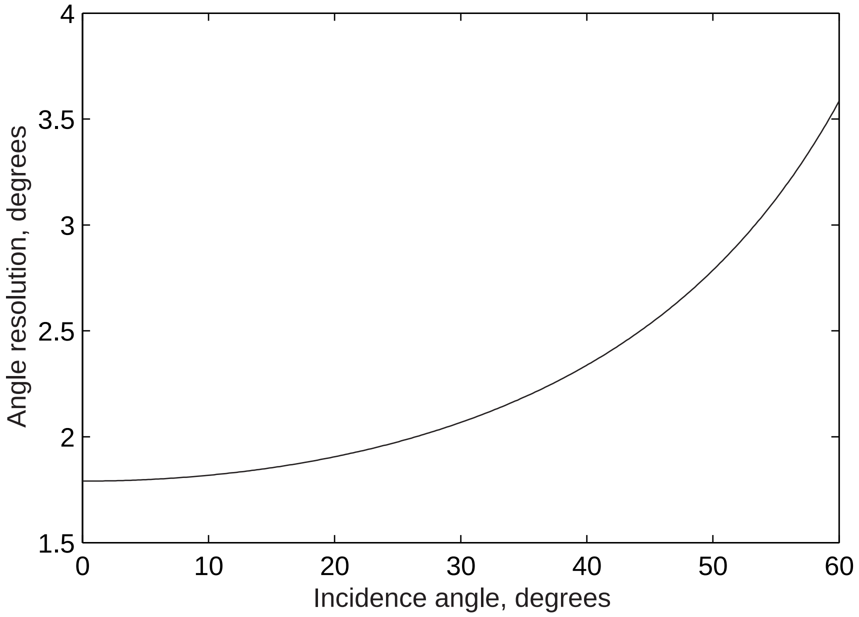

Figure 3.6: Angular resolution (angle of the first zero in the directivity pattern) of an array with size 32λ, given as a function of angle of incidence of the incoming wave.

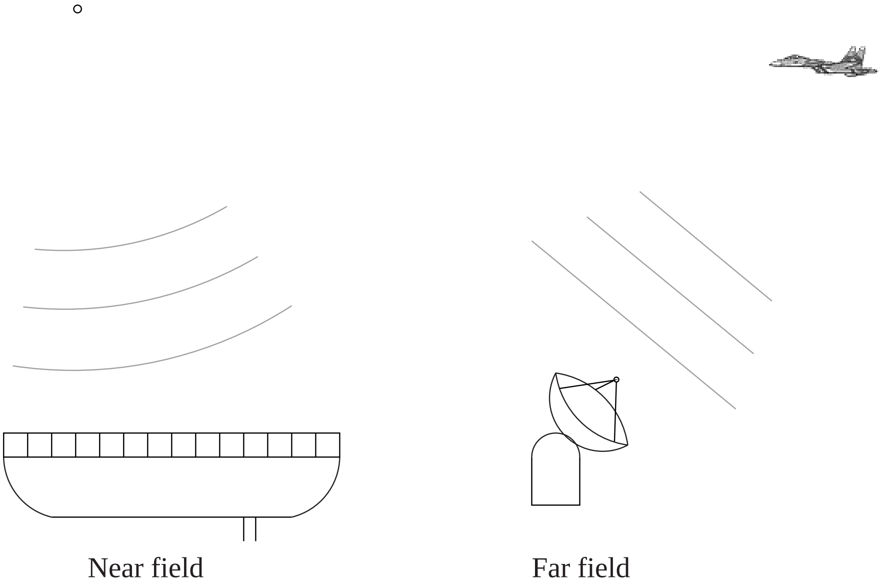

Figure 3.7: Illustration of near field (ultrasound) and far field (radar).

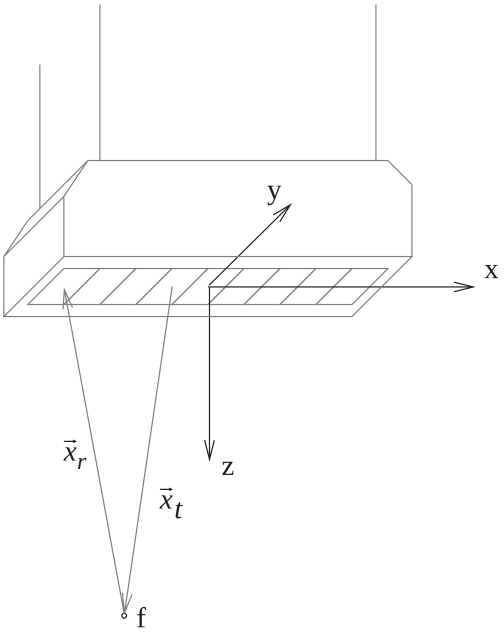

Figure 3.8: Focusing geometry

3.2.1 Focusing geometry

The focused signal is obtained by coherent summing of the sensor signals:

$$s(t) = \sum_{i=1}^{N_{xdc}} a_i r_i(\tau_i(t)) \tag{3.7}$$

In this expression, N_{xdc} is the number of transducer elements, r_i is the received echo signal and τ_i are the times of flight of the wavefront. The parameters a_i are the apodization (tapering, weighting) coefficients, which are applied on the sensor signals with the purpose of suppressing the sidelobes in the directivity pattern.

The time of flight τ is calculated as

$$\tau_i(t) = \frac{|\vec{x}_t(t)| + |\vec{x}_r(t)|}{c}, \tag{3.8}$$

where $\vec{x}_t$ is the path from a transmit element to the focal point f, and $\vec{x}_r$ is the echo path to a receiving element (see Fig.3.8).

According to the convention adopted by the Center for Fast Ultrasound imaging, the coordinate system has its origin at the middle of the transducer array, the axis x is along the array and the axis z points in depth, perpendicular to the array surface. In most imaging modalities used nowadays, and throughout this dissertation, the beam origin is at the middle of the transducer and coincides with the origin of the coordinate system.

A receiving element close to the focal point projection on the transducer surface receives the echoes earlier than a more distant one. Therefore, the alignment of the echo signals requires delaying of some sensor signals with respect to other by means of inverse binary tree or delay lines. In general, the length of the delay lines should be such that they can compensate for the maximum difference between the times of flight of the echo signal to different receive elements.

3.2.2 Influence of the speed of sound

In the above geometric calculations, and throughout this thesis, the speed of sound c is assumed to be constant. In reality, it varies by up to several percent in different tissue types. As a result of that, the signal from given scatterer might arrive later or earlier than calculated to some receive element. The focusing in that case is not as effective as in the case of constant sound speed. There exist phase aberration correction methods [6, 7, 8] which attempt to detect the corresponding source (scatterer) contributions in different sensor traces by finding the peak of the correlation between the latter. Then, the contributions are aligned and summed. These methods are very computationally intensive.

3.2.3 Influence of the delay precision

The precision of the delays applied on the sensor signals has high impact on the array ability to focus in a given direction. Several research groups have been attempting to quantify that influence [9, 10, 11]. There are two ways in which the imperfect delays can introduce unwanted lobes in the directivity pattern of an array. One is the presence of periodicity of the delay error across the array, effectively forming a number of subarrays that point away from the target direction. Such an effect can occur when the focus is in the far field, and is less pronounced in near filed focusing. The resulting lobes are called *discrete quantization lobes*. More significant for the medical ultrasound are the *random quantization lobes* which are caused by randomly distributed delay error across the array in near field focusing. According to the most restrictive of the published formulae, given in [11], the worst-case discrete quantization lobe level in a beamformer is described as:

$$SL_{focus} \approx \frac{2}{mL\cos\varphi}\frac{1}{IPG}\left(\frac{r\lambda}{m}\right)^{\frac{1}{2}}, \tag{3.9}$$

where

$$IPG = \frac{1}{N}\sum_{n=0}^{N-1}\omega_n^2 \tag{3.10}$$

is the incoherent power gain of an N-element array with apodization coefficients $\omega_n, n = 1..N$, φ is the beam angle from the normal, λ is the wavelength, $m = \frac{f_s}{f_0}$ is the ratio of the sampling frequency and the central frequency, L is the aperture size, and r is the distance along the beam.

The maximum random quantization lobe level (due to random phase errors over the array) is

$$SL_{peak} \approx \frac{\pi}{m}\left(\frac{4.6\,ENBW}{3\,N}\right)^{\frac{1}{2}}, \tag{3.11}$$

where

$$ENBW = \frac{IPG}{CPG}, \; CPG = \left[\frac{1}{N}\sum_{n=0}^{N-1}\omega_n\right]^2 \tag{3.12}$$

is the equivalent noise bandwidth, (CPG being the coherent power gain of an N-element array). The maximum quantization lobe level is $SL_{max} = max(SL_{focus}, SL_{peak})$.

In a common imaging situation, the necessary delay precision is $\frac{1}{40}$ to $\frac{1}{20}$ of the period of the central frequency used for the imaging. It should be noted that it is enough to calculate the necessary precision for achieving half of the desired quantization lobe level, since the formulae given above refer to the one-way directivity pattern.

3.3 Beamforming

In medical ultrasound, delay-and-sum (time-domain) [2, 12, 13, 14, 15] focusing is used. The information for the interrogated tissue is gathered by creating focused ultrasound beams in transmit and forming a directivity pattern in receive that points in the same direction, hence the term *beamforming*. In the most popular technique nowadays, series of adjacent beams are formed, which sweep the area of interest. The received echoes are displayed as adjacent lines on the screen, and interpolation is performed across them. No information about the interrogated area should be lost, therefore the spacing between the image lines is smaller or equal to the lateral (angular) resolution of the system.

The envelope reconstruction requires in-phase and quadrature components of the received signal. These can be obtained by demodulation applied on the received signal. This approach is a narrow-band one, and is not precise in case of wider signal band. In simulations and off-line processing the quadrature component is generated by applying Hilbert transformation on the received signal. If a sampling technique is used that provides the in-phase and the quadrature component of the received signal, there is no need for high sampling rate and the beamforming need only be performed for the desired focal points.

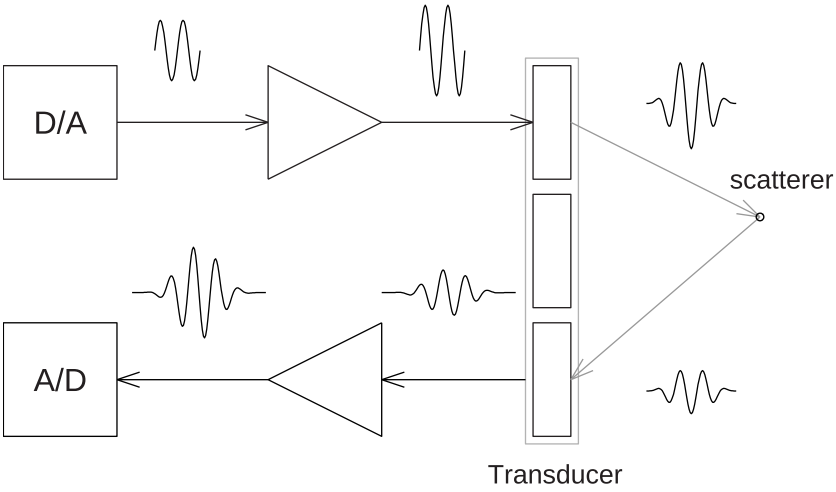

Figure 3.9: Analog signal transformations in an ultrasound imaging system.

Range resolution of an ultrasound imaging system

For the purpose of evaluating the properties of an ultrasound imaging system and comparing it to other systems, it is necessary to define the criteria that are used. The angle resolution has been considered in 3.1.2. In this subsection, the range resolution criterion will be defined.

The analog signal transformations in an ultrasound imaging system are illustrated in Fig. 3.9. A specified waveform $s(t)$ is generated by a D/A converter and is amplified by high-voltage amplifiers. On transmit, the pulse is shaped by the impulse response of the transducer element. The pressure wave propagates into the tissue and is reflected by the inhomogeneities. The echo is shaped by the impulse response of the receiving transducer element and after suitable amplification is sampled. In this path, the transducer impulse response $h(t)$ distorts the signal most. Usually, the transducer transfer function has approx. 60 % bandwidth at -6 dB around certain frequency. Since that bandwidth is not infinite, the impulse response is not a delta function, but a longer, oscillating waveform.

The received echo from a point reflector in front of the transducer will be

$$e(t) = s(t) \underset{t}{*} h(t) \underset{t}{*} h(t), \tag{3.13}$$

and it is longer than the pulse sent initially. The length of the envelope of $e(t)$, measured at 6 dB below the peak (at half amplitude), is said to be the range (axial) resolution of the ultrasound image system.

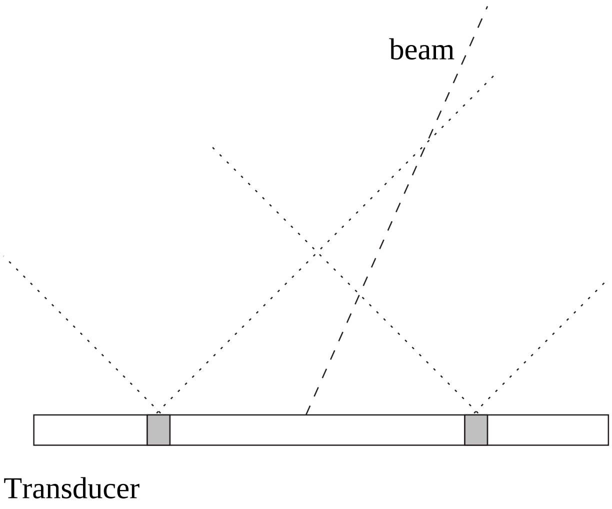

Figure 3.10: Practical limitations of the beamforming.

3.3.1 Transducer element directivity implications

Because of the directivity of the transducer elements, the channels can start contributing to the beamforming at some instant t_s after the transmission takes place. The delay between the transmission time t_0 and t_s depends on the beam inclination and the directivity pattern of the transducer elements, as illustrated in Fig. 3.10.

In this example, a practical limit of $\frac{\pi}{4}$ was set on the directivity pattern of the transducer element. Therefore, the range of inclinations φ of the beam is limited to the range $\left[-\frac{\pi}{4}, \frac{\pi}{4}\right]$. At the limits of that range, only half of the elements in the aperture can contribute useful signal. That is the reason why in real phased array images the signal-to-noise ratio is lower at the sides of the images.

For the purposes of the beamforming, one additional parameter can be specified for each channel: delay to start of use. The setup for calculating that parameter is shown in Fig. 3.11.

The distance d_0 along the image line from which an element i should start taking part into the beamforming can be derived using the Sinus theorem for a triangle as

$$d_{0,i} = \frac{x_i}{\sqrt{2}\sin(\frac{3\pi}{4} - \varphi)}, \tag{3.14}$$

where x_i is the distance between the transducer element and the origin of the transmitted beam. According to this relation, the receive aperture is not symmetrical when the image line is tilted.

Taking the described limitation into account when designing a beamformer leads to relaxed requirements for the length of the delay lines.

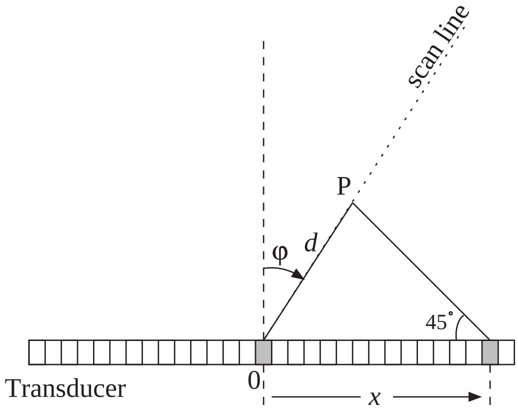

Figure 3.11: Setup for calculating the delay after which a channel could take part in the beamforming.

3.4 Beamforming techniques

In this section, a brief description of the beamforming techniques used in medical ultrasound will be given.

Fixed focus beamforming

Historically, the first method to be used was fixed focusing, not by electronic steering or delays, but by using fixed-focus single-element transducers. The sweep of the region of interest was done by rotating the transducer. The imaged area had sector shape and the imaging systems had fixed focus both in transmit and receive.

Multiple focal zones in receive

The introduction of multi-element transducers allowed better focusing in receive. By switching delay lines, several receive foci can be formed. The switching introduces noise, therefore special measures have to be applied, for example saving the switching noise and subtracting it form the displayed lines. The image resolution around the focal points is better than elsewhere. For avoiding the presence of areas with visibly lower resolution, the foci should be sufficiently closely spaced. The multiple focal zones approach and the fixed-focus approach are shown in Fig. 3.12.

Dynamic focusing in receive

The introduction of digital delay lines made it easy to change the length of the delay lines at every clock cycle. Thus, every beamformed sample can be reconstructed with time error of ±1 clock period. For achieving higher delay precision, fractional bandwidth filters can be used [16], if the beamformer has the necessary calculation capabilities. Linear interpolation

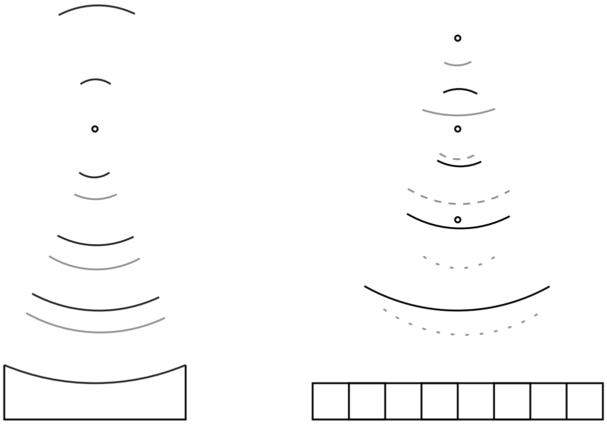

Figure 3.12: Fixed focus setup (left) and multiple receive focal zones (right). The shape of the transmitted wave at different depths is illustrated by black arcs and the expected waveforms (summed coherently in the imaging system) are shown in gray.

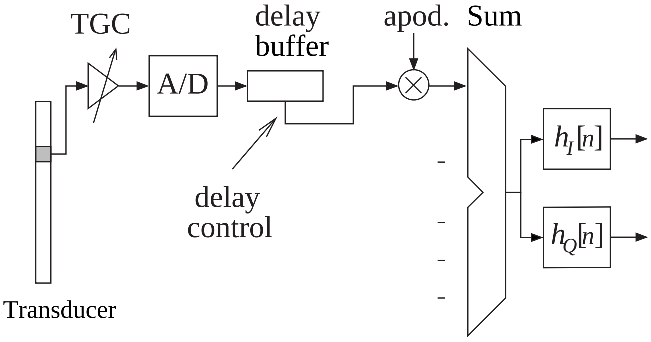

Figure 3.13: Digital beamformer architecture

between samples has been implemented in the experimental RASMUS system [17].

The architecture of a digital beamformer is shown in Fig. 3.13. The echo signal on each channel is amplified by a time-gain compensation (TGC) amplifier which compensates for the signal attenuation as it propagates in tissue. A buffer with variable length provides the delay precision of ± 1 clock period. After applying fine delay and aperture tapering (apodization), the aligned signals from all active channels are summed.

Advanced techniques with fixed transmit focus

In the described approaches, a fixed focus in transmit exists. That limits the achievable resolution of the imaging systems away from the focus. There exist approaches to compensate for it [18, 19, 20], based on depth- or position-based matched filtering of the echo signal. Another approach is to re-beamform the echo data after a full image has been created [21].

Synthetic transmit aperture (STA) beamforming

The STA beamforming (also called Synthetic Transmit Focusing - STF) achieves high resolution by performing focusing in both transmit and receive. In this imaging technique, low-resolution images are created instead of image lines, by transmitting with one element and receiving with all. The same focal points are imaged in all low-resolution images. Each low-resolution image contains a contribution to the final image that corresponds to the used transmit element. A high resolution image is obtained by summing the low-resolution images. The distribution of focal points within the image follows the conventions of the older imaging techniques, and the images consist of image lines originating from the transducer. The reason for adhering to the concept of image line is that having closely spaced samples allows signal envelope reconstruction.

Using one element in transmit leads to very poor echo strength and correspondingly, low signal-to-noise ratio (SNR). One way of increasing the amount of transmitted energy is to use several elements and emulate the wavefront of point source [22]. Another approach is to send longer pulses that contain more energy. For achieving low axial sidelobe level, appropriate encoding techniques are used. An effective and simple encoding is the linear frequency modulation [23]. The waveforms, called *chirps*, sweep across the available transducer bandwidth. A combination of encoding and use of multiple elements in transmit gives very good results [24]. Also, spatial encoding using Hadamard matrices can be used for improving the SNR [25].

A drawback of the STA technique is its susceptibility to tissue motion, due to the fact that the image points are created using several transmissions. Therefore, it is preferable that the number of the necessary transmissions is kept low. Otherwise, motion compensation techniques have to be used. That issue affects only the B-mode imaging. The flow estimation can successfully be implemented without applying motion compensation [26].

3.5 Comparison between focusing techniques

In Fig. 3.14, the two-way directivity patterns of the fixed-transmit-focus techniques are shown. The image was obtained by simulating a linear array in the ultrasound field simulation program Field II [27]. The simulation parameters are shown in Table 3.1. The F-number is defined as the ratio between a given distance and the extent of the transducer that is used in the specific case.

The figure shows only the intensity profile and does not reveal all the benefits from dynamic beamforming. The phase alignment is very important, and when dynamic beamforming is used, a better resolution is achieved.

A simulation of the beamforming was done in Field II that compares the fixed transmit focus

Parameter	Value
Speed of sound	1540 ms^{-1}
Transducer center frequency f_0	5 MHz
Excitation	2 periods of a sinusoid at f_0
Number of channels	32
Transducer pitch	$\frac{\lambda}{2}$
Transmit focus depth, F-number	5
Image depth, F-number	10
Transmit apodization	uniform
Receive apodization	Hamming window

Table 3.1: Parameters for the obtained directivity patterns using different beamforming techniques

approaches to synthetic transmit aperture beamforming. The parameters of the imaging are the same with the exception that the number of elements is 64 and the transmit focal depth is at F-number of 6. The beamforming for the fixed transmit focus techniques was done by routines in Field II, while the beamforming for the STA technique was done using the Beamformation toolbox [28] by Svetoslav Nikolov, Ph.D. The point spread functions of point reflectors at depths corresponding to F-number of 1, 2, 4, 6, 8 and 10 are shown in Fig. 3.15 and 3.16.

It can be seen that with STA, the resolution improvement is most significant close to the transducer, where the fixed transmit focus approaches have large delay errors. A comparison of the lateral resolutions obtained at different depths using the considered approaches is shown in Fig. 3.17.

3.6 Conclusion

It can be seen that a beamforming technique with dynamic focusing both in transmit and receive provides a uniform high angular resolution across the ultrasound image. Regardless of whether it is a re-beamforming technique or STA approach, its memory and computational requirements are higher than these of the conventional line-by-line techniques. There is no doubt that in the coming years, as more and more logic and memory is integrated in one integrated circuit, the mentioned advanced techniques will find their way into commercial ultrasound scanners.

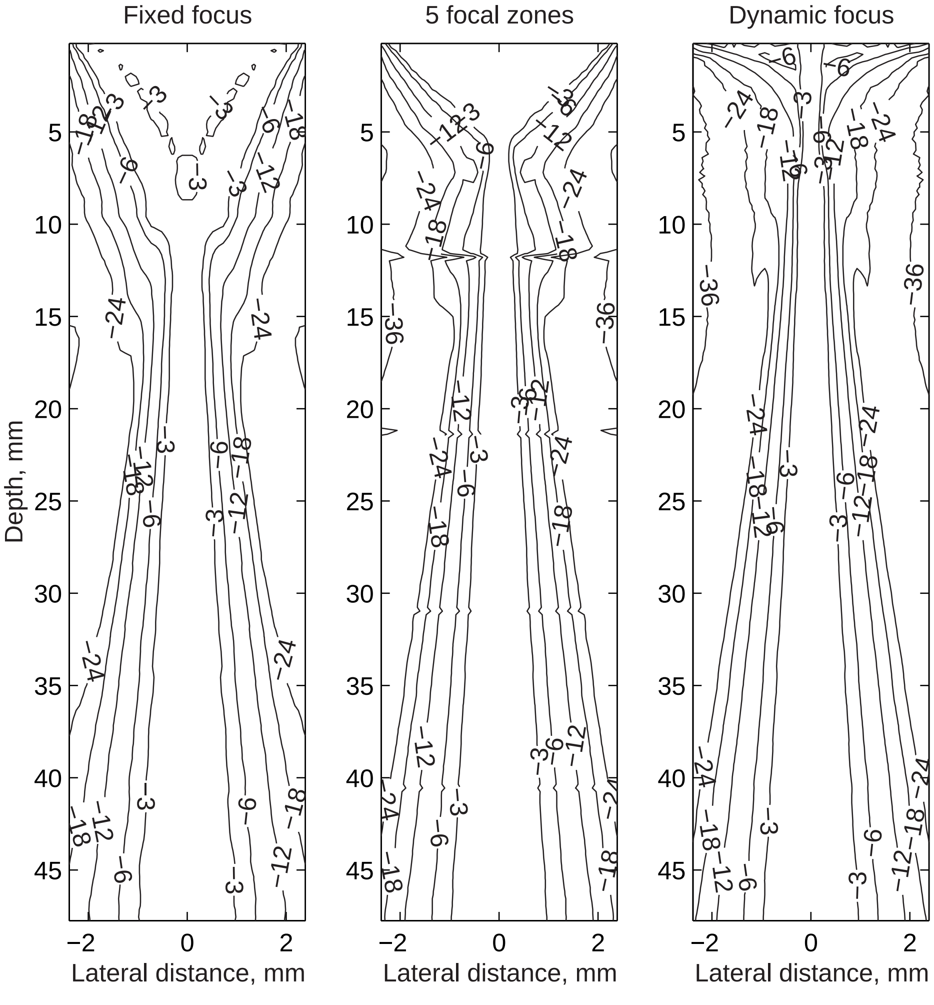

Figure 3.14: Pulse-echo fields for different beamforming techniques

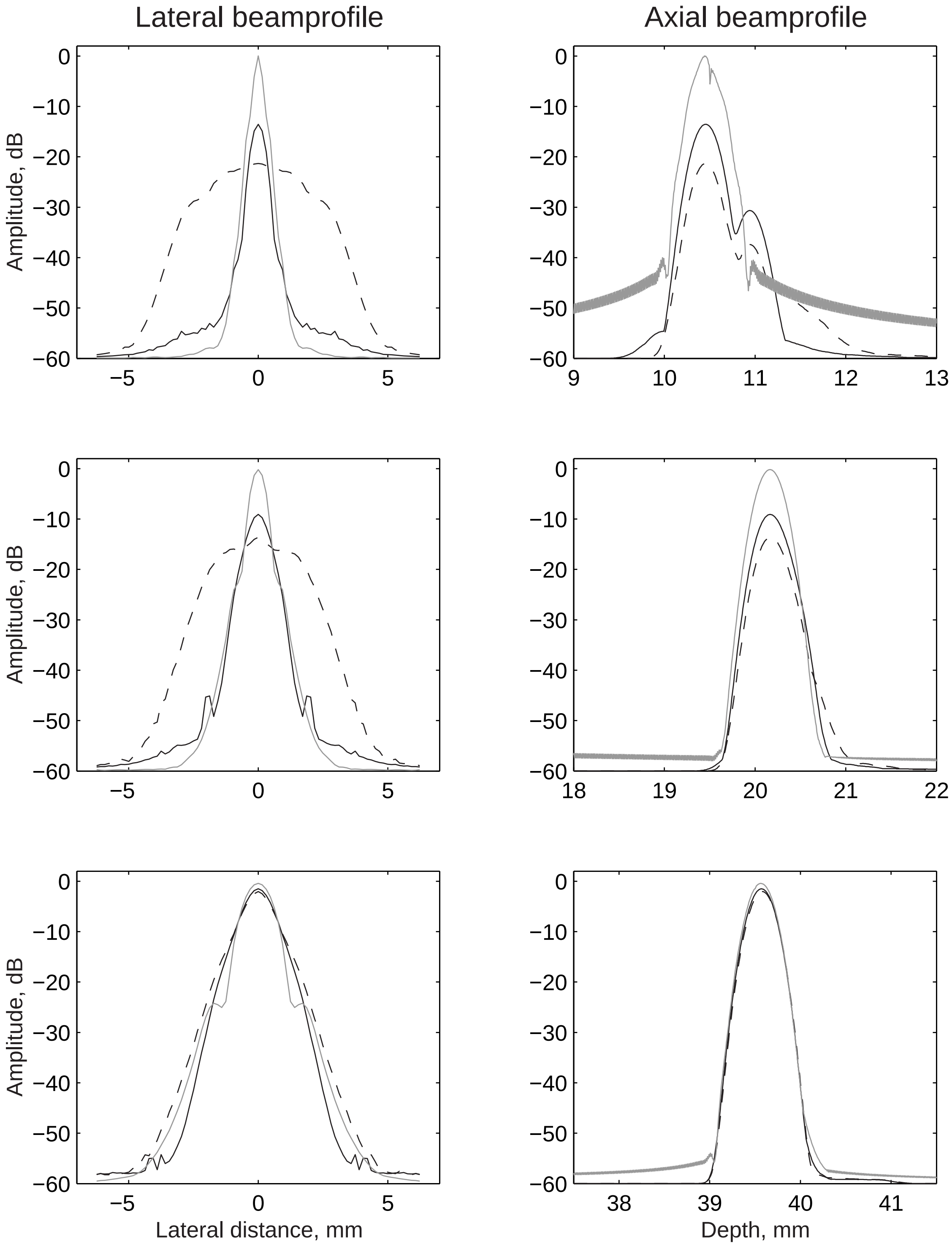

Figure 3.15: Point spread functions for depths corresponding to F-numbers of 1, 2, and 4. The fixed-focus case is drawn with dashed line, the dynamic receive focusing is represented by black line, and the STA is shown with gray line.

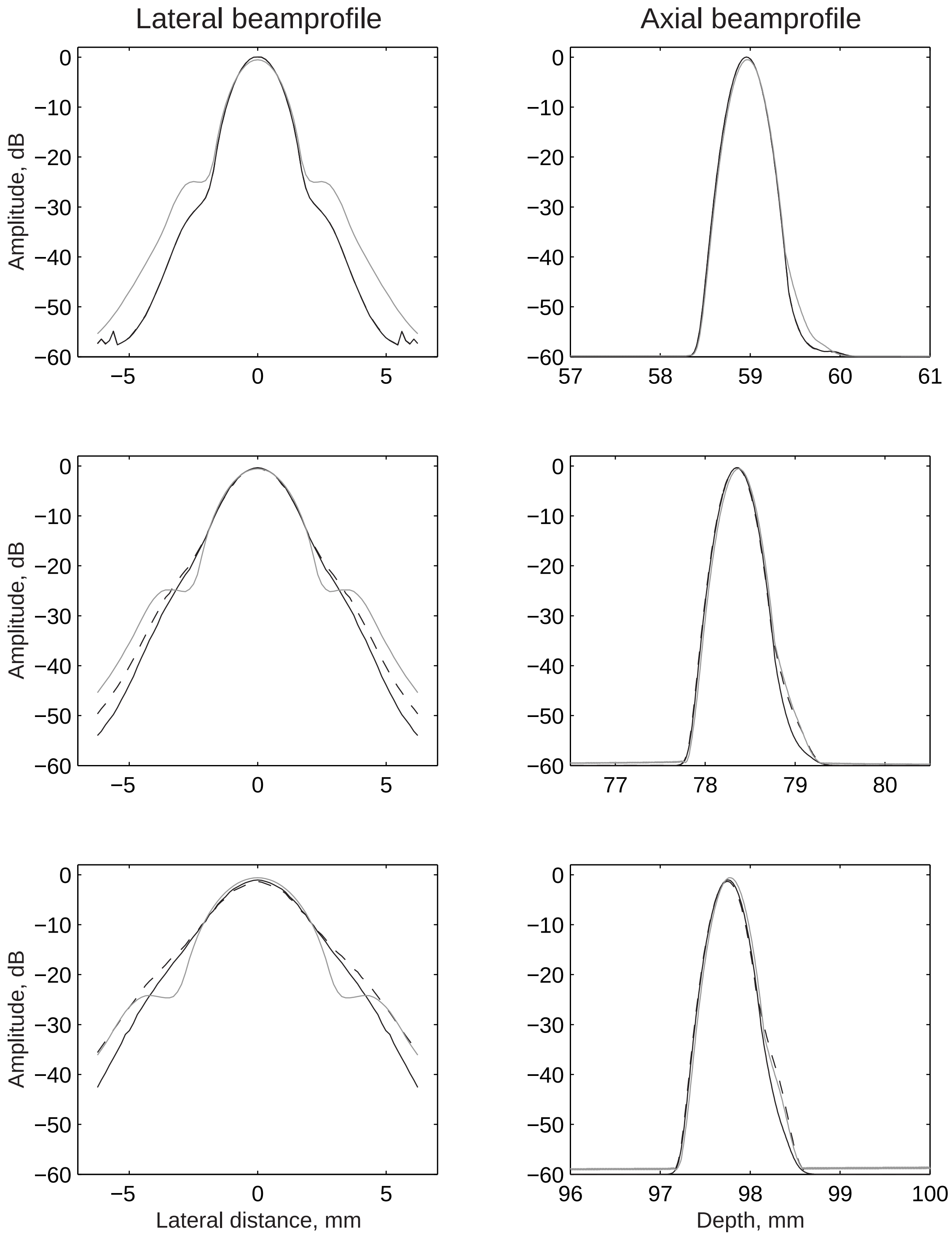

Figure 3.16: Point spread functions for depths corresponding to F-numbers of 6, 8, and 10. The fixed-focus case is drawn with dashed line, the dynamic receive focusing is represented by black line, and the STA is shown with gray line.

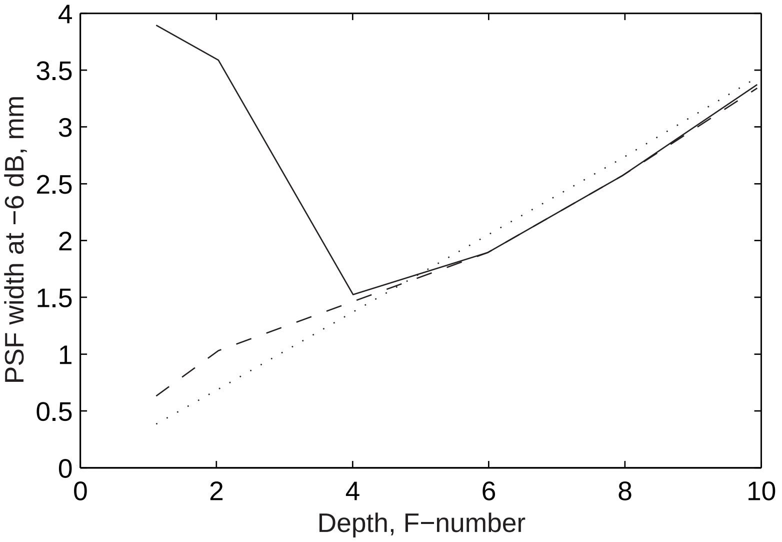

Figure 3.17: PSF widths: fixed-focus is shown with continuous line, dynamic focus in receive is shown with dashed line, and STA is shown with dotted line.

CHAPTER

FOUR

Compression of the the focusing data

The use of digital memory allows a new focal point to be targeted for each sample produced by the beamformer. The amount of necessary focusing information is large, since delay information for all receive channels for all focusing depths has to be stored. Keeping it in an uncompressed form requires a lot of memory, and researchers have been working on approaches for compression since the introduction of the digital beamformation. With the advances in digital IC fabrication, the algorithms grew in complexity. Among the first to investigate compression of focusing data were Peterson and Kino [10]. They suggested delta encoding - storing only the differences between the delay (index) values. Among the first to suggest a parametric approach for delay calculation were Jeon et al. [29], who applied this technique to sampling clock generation. Recently, Feldkämper at al. [30], while working on the LUCS (Low-power Ultrasound Chip Set) project, developed an efficient delay computation scheme along the same principle, offering a very compact implementation. This method will be discussed further and it will be referred to as the ”LUCS delay generator”.

During the development of a new oversampled beamformer architecture [31], a general parametric delay generation algorithm was developed, capable of providing a geometrically valid delay value for all channels from the moment of transmission. Due to the need of operation at a high frequency, piecewise-linear approximation of the delay curve was also investigated. This paper presents the approaches considered and the implementation results for each of them.

This chapter will focus on the available approaches and the trade-offs that can be made in that area. Section 4.1 demonstrates by an example the need for compressing the focusing data. Section 4.2 shows the delay calculation geometry and the equations that can be derived from it. Section 4.3 describes the delta-encoding and its performance with respect to compression of delay information. In Section 4.4, the piecewise-linear approximation approach is presented. The general parametric approach is described in Section 4.5 and the LUCS delay generator is presented in Section 4.6. Comparison between the memory requirements of the approaches and their implementation results are given in Section 4.7. Section 4.8 contains a discussion on the suitability of the approaches for different beamformer types.

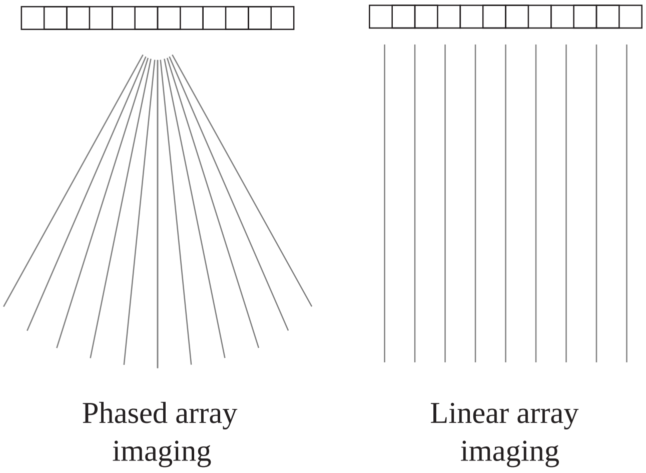

Figure 4.1: Image line positions in different imaging techniques.

4.1 Memory requirements in ultrasound beamforming

A digital beamformer that performs dynamic receive focusing requires a new delay value on each clock cycle and for every channel involved in the beamformation. For an image line with a length $d_l = 15$ cm, sampled at a frequency $f_s = 40$ MHz and for speed of sound $c = 1540$ ms^{-1}, the number of the delay values is

$$N_l = \frac{2d_l f_s}{c} = 7792. \tag{4.1}$$

That number, multiplied by the number of channels n, will yield the necessary storage size for the beamformation of one image line. For calculating the necessary storage for a whole image, multiplication by the number of lines m has to be done. For a modest ultrasound imaging system with 64 channels, the number of delay values per frame consisting of 80 lines is

$$N_f = mn\frac{2d_l f_s}{c} \approx 40 \times 10^6. \tag{4.2}$$

Depending on the way the image lines are generated in an ultrasound image, different options for reducing the amount of necessary memory exist:

- In phased array imaging, the symmetry in the beamforming can be exploited so that the number of values is halved (see Fig. 4.1).
- In linear array imaging, with linear or convex transducer, the delay information is the same from line to line, and the channels connect to a different transducer element on

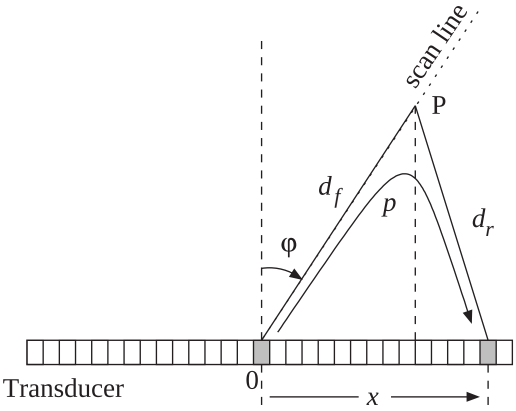

Figure 4.2: Delay calculation geometry

every emission. In addition, there is symmetry in the delay profiles, which allows the amount of focusing data to be halved. In that case, the necessary number of delay values for a 64-channel system is

$$N_f = m\frac{2d_l f_s}{2c} = 249 \times 10^3. \tag{4.3}$$

In both cases, the necessary storage could hardly fit together with the focusing logic into a single-chip beamformer. Compression the focusing information relaxes the memory requirements. A conventional, transportable imaging system, also benefits from reducing the amount of integrated circuit it uses.

4.2 Delay calculation

The images produced by the contemporary ultrasound scanners consist of straight lines originating from the transducer surface. The geometry for the calculation of the time of flight of the ultrasound wave is shown in Fig. 4.2.

The distance from the beam origin to a focal point P along the scan line is denoted d_f and the echo path is denoted d_r. The full path of the ultrasound wave is denoted $p \equiv d_f + d_r$. The distance between the beam origin center and the receiving element is denoted x and the angle between the scan line and the normal to the transducer surface is denoted φ.

The echo path d_r can be expressed as:

$$\begin{aligned} d_r = p - d_f &= \sqrt{(x - d_f \sin\varphi)^2 + (d_f \cos\varphi)^2} \\ &= \sqrt{x^2 - 2d_f \sin\varphi + d_f^2}. \end{aligned} \tag{4.4}$$

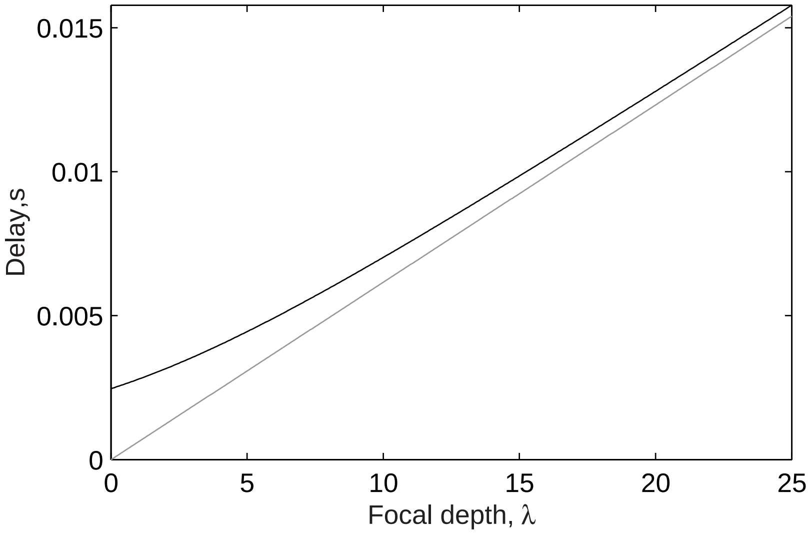

Figure 4.3: Delay profiles for center element (gray) and an element (black) situated at 8 λ away from the center element.

The pulse-echo path p is calculated as

$$p = d_f + d_r = d_f + \sqrt{x^2 - 2d_f \sin\varphi + d_f^2}. \tag{4.5}$$

The times of flight for transducer element at the beam origin and for another element that is situated at a distance of 8λ away from it are shown for depths up to 25λ and non-tilted beam in Fig. 4.3. Here $\lambda = \frac{c}{f_0}$ is the wavelength, while c is the speed of sound and f_0 is the central frequency of the transmitted wave. The figure illustrates the nature of the delay profiles in beamforming. As the wave propagates in depth, the difference between the times of flight for different receiving elements decreases.

The forward path d_f is calculated as

$$d_f = c(t - t_0) \tag{4.6}$$

where t_0 is the time of the firing. In a digital beamformer, the time is discretized by the sampling period $T_s = \frac{1}{f_s}$, and is expressed as $t_n = nT_s$. Eq. 4.5, is converted to clock cycles by dividing its both sides by the path traveled by the ultrasound wave in one clock period cT_s. The forward path is expressed as $d_f[n] = cnT_s$ and the resulting expression for the sample index that carries the echo from a point that was reached by the wave on clock cycle n is

$$u[n] = n + \sqrt{x_d^2 - 2x_d n \sin\varphi + n^2}. \tag{4.7}$$

Here, the number of clock cycles corresponding to element distance from the transducer center is $x_d = \frac{x}{cT_s}$.

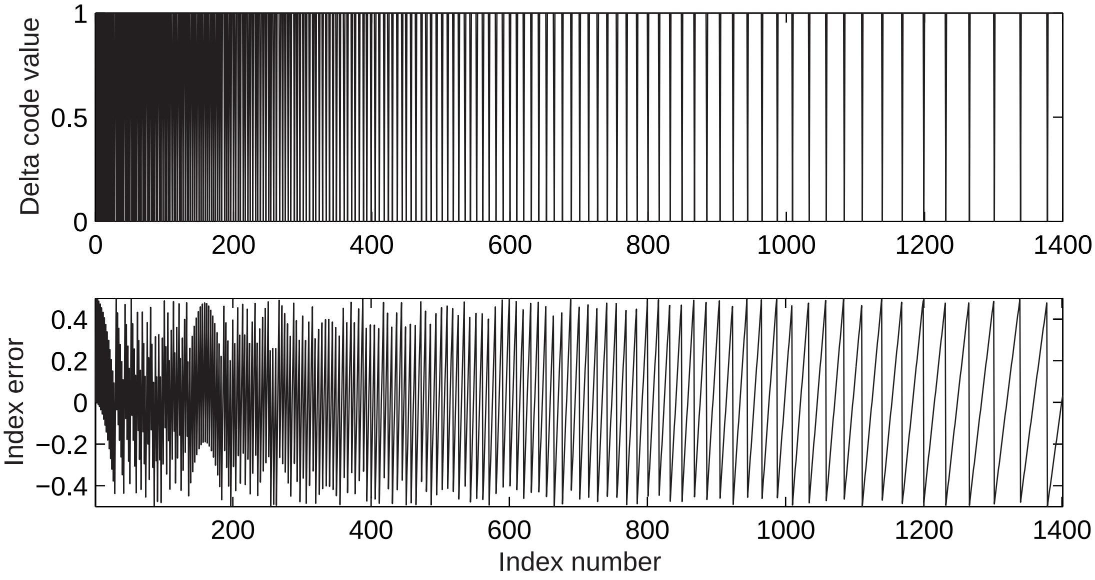

Figure 4.4: Index error and delta-encoded index information for target index resolution of T_s.

In this thesis, independent beamformer channels are considered and the focusing is viewed as selecting the correct sample for a given focal point from the sample streams of different channels. Therefore, the beamformation will be described by sample indexes (absolute delays from the moment of transmission) and not by relative delays between channels.

4.3 Delta encoding

The most obvious way of reducing the necessary storage space is to store the differences $d_{d,n}$ between the consecutive index values

$$v[n] = u[n+1] - u[n]. \tag{4.8}$$

This technique is called delta encoding and it has been used in digital beamformers for many years [10].

When the target is to provide an index resolution of 1 clock period, 0s and 1s are sufficient for representing the difference information, as shown in Fig. 4.4. This figure has been obtained for an image depth of 15 cm and sampling frequency of 40 MHz. The difference information, together with initial delay value, describes the quantized delay curve. The delay values are in the range from 0 to 7794, therefore they have to be represented by 13-bit numbers. The delta-encoding information consists of 0's and 1's and therefore it is represented by a single bit. The saving in memory for this case is $\frac{13-1}{13} \approx 92$ %.

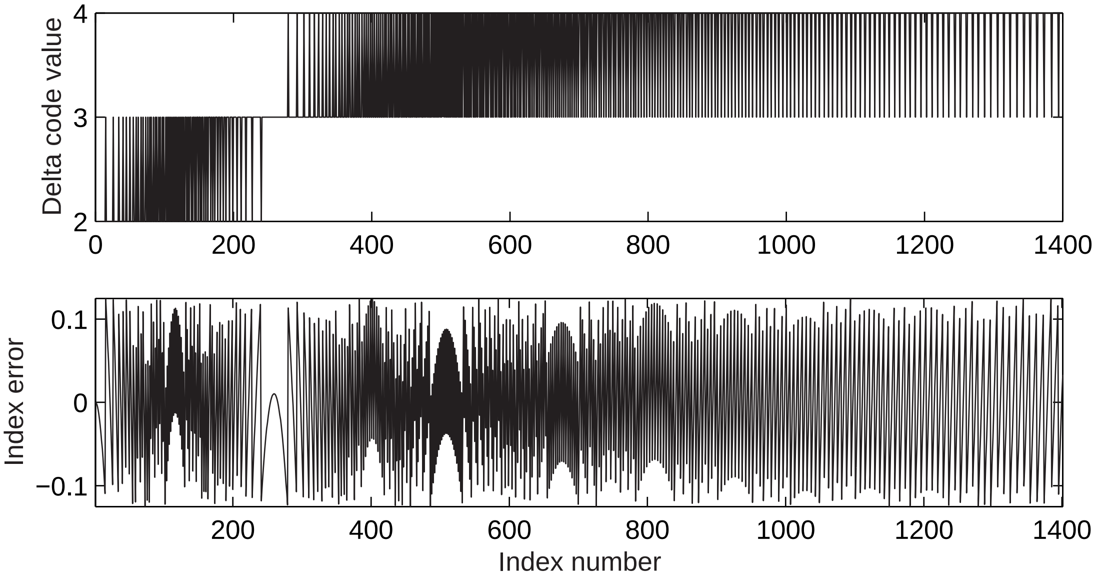

Figure 4.5: Index error and delta-encoded index information for target index resolution of $\frac{T_s}{4}$.

In most beamformer realizations available nowadays, the sampling rate alone does not provide the necessary index resolution for good image quality (discussed in 3.2.3), and interpolation between samples is used. For that purpose, the sample indexes have to include additional bits that provide the intersample precision. In that case the delta information is represented by more than one bit, as shown in Fig. 4.5. Here, 2 additional bits are necessary for representing the non-compressed index information, and 2 bits are necessary for representing the difference information. The saving in memory for this case is $\frac{15-2}{15} \approx 87$ %

It is obvious that the approach is quite beneficial, compared to the non-compressed storage approach. With respect to compact beamformation, though, the amount of necessary memory is too large.

4.4 Piecewise-linear approximation

The delay curve can be approximated using a piecewise-linear approximation, as shown in Fig. 4.6, where axis t represents the time and axis n represents the sample index. The number of segments is determined by the magnitude of the acceptable error and the curvature of the delay profile. For a less curved delay profile or larger acceptable error, the amount of data (the number of pairs slope/segment length) is smaller than for a strongly curved profile or smaller acceptable error. After determining the number of necessary segments for representing the delay curve with some predetermined precision, a set of tests is run for determining the necessary bit width

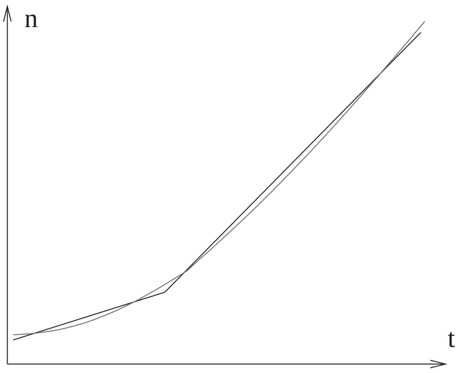

Figure 4.6: Piecewise-linear approximation of a delay curve.

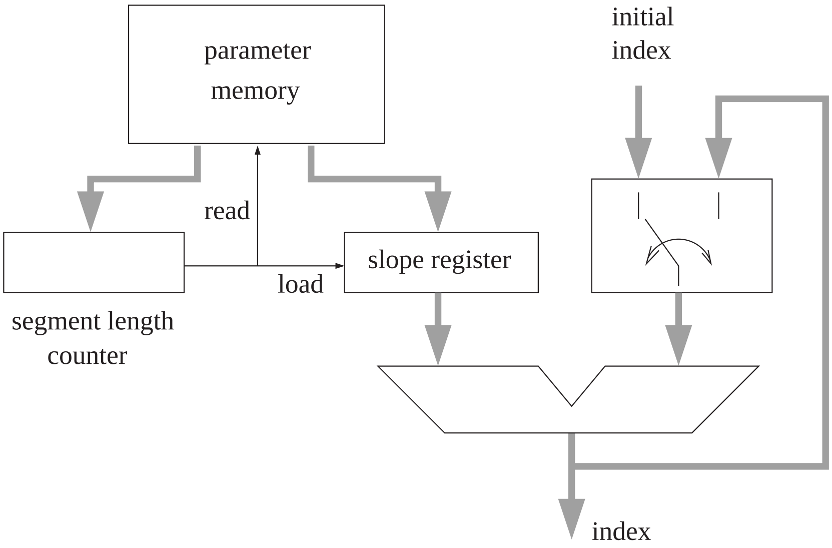

Figure 4.7: Piecewise-linear delay generator.

of the slope representation word, so that the introduced error from quantization is below 10 % of the selected maximum delay error.

A simple logic for the delay generation using that method is shown in Fig. 4.7. It is very simple and can operate at very high speed. An adder adds the slope to the current delay on each clock cycle. When the segment counter reaches the end of the current segment, new segment length and slope are loaded. The focusing data is represented by an initial sample index and pairs of slope and length for each segment. Delta encoding can be used for the segment slope component, since it gradually increases, and the segment length, since it also increases as the curvature of the delay profile decreases with depth.

4.5 General parametric approach

A pioneer in the numeric control, Bresenham suggested algorithms for fast drawing of lines, circles and ellipses on raster devices [32]. According to his approach, the describing equation of a curve is rewritten as a function of point coordinates. When the value of the function is zero, the point with the current coordinates lays on the curve. When the value is positive or negative, the point is either above or below (on the left or on the right side of) the curve. The sign/space relation depends on the chosen leading coordinate and the way the curve equation is rewritten. The leading coordinate is the one that is supposed to increase by a unit at each calculation (and drawing) step. During drawing of circles and ellipses, the leading coordinate changes (from x to y) at the places where the slope of the curve crosses $\frac{\pi}{4}$.

Bresenham's approach can be generalized for use with any kind of curve that is described by a quadratic function. Due to the fact that the delay curve can be described by an equation, a delay generation algorithm can be built around that equation by numerically solving it at each step of increase of a leading variable (in this case - time). The resulting implementations require a few input parameters, but have the disadvantage of dissipating power in calculations. This section presents a general algorithm for approximating the ideal delay curve, developed for use in a compact beamformer.

4.5.1 Transformation to clock periods (clock cycles)

After some transformations, (4.5) turns into

$$p^2 - 2d(p - x\sin\varphi) - x^2 = 0. \tag{4.9}$$

This is the equation of the delay curve. The term $x\sin\varphi = k$ is constant for a given line inclination and element.

The aim of the delay generation approach is for every focused output sample to produce delays (sample indexes, RAM addresses) that for each channel are pointing to the appropriate input sample, necessary for the focusing of that output sample. For this purpose, the algorithm is expected to generate delays at a rate of one value per output sample. The leading variable in (4.9) is the instant focal depth d, which changes by $\Delta = cT_s/2$ with each clock cycle. Dividing both sides of (4.9) by the squared distance Δ^2 converts the computation unit into clock cycles:

$$f(p_N, d_N) \equiv p_N^2 - 2d_N(p_N - k_N) - x_N^2 = 0. \tag{4.10}$$

The index N denotes that the variable unit is quantized and it is integer.

4.5.2 Delay values generation

In the suggested algorithm, the function to be evaluated is $f(p_N, d_N)$.

In order to keep the focus on the imaged line, the delay generation logic has to keep $f(p_N,d_N)$ as close to 0 as possible, therefore it should increase p_N by 1 or 2 for each unit increase of d_N. The choice[1] is made by evaluating the sign of the function $f(p_N+1,d_N+1)$. It can be seen that:

$$f(p_N+1,d_N+1)=f(p_N,d_N)-2d_N+2k_N-1<f(p_N,d_N) \tag{4.11}$$

and

$$f(p_N+2,d_N+1)=f(p_N,d_N)+2p_N-4d_N+2k_N>f(p_N,d_N). \tag{4.12}$$

Therefore the following algorithm is suggested:

1. The initial values $d_N(1)=d_{start}\frac{f_s}{c}$, $p_N(1)=p_{start}\frac{f_s}{c}$, and $k_N=x\sin\varphi\frac{f_s}{c}$ are supplied.
2. If $f(p_N+1,d_N+1)>0$, then $p_N(n+1)=p_N(n)+1$, else $p_N(n+1)=p_N(n)+2$.
3. If the end of the line is not reached, go to 2.

The described algorithm generates output with a maximum error of ± 1 units. Since these units correspond to the distance that the waveform travels in a half clock period, the time error is less than $\pm 1/2$ clock periods.

4.6 LUCS delay generator

This approach is based on a different use of the delay geometry. It is shown in Fig.4.8. The distance to the focal point is expressed as $r(t)=tc/2$ and the time-of-flight difference between the transducer element at the beam origin and another element is calculated as:

$$l(t)=\sqrt{r^2(t)+2r(t)x\sin\varphi+x^2}-r(t). \tag{4.13}$$

The focal depth changes by $\Delta=cT_s/2$. Eq. (4.13) is squared and scaled with the distance Δ . It becomes:

$$\underbrace{n^2+2nk(n)+k^2(n)}_{A(n)}=\underbrace{n^2+n\alpha+\beta}_{B(n)}, \tag{4.14}$$

where $n=r(nT_s)/\Delta$ is the clock period number, $k(n)=l(nT_s)/\Delta$ is the quantized value for the time-of-flight difference, and $\alpha=2x\sin\varphi/\Delta$ and $\beta=x^2/\Delta^2$ are precalculated constants, specific for each scan line. The expressions $A(n)$ and $B(n)$ are calculated iteratively:

---

[1] In case of a tilted line, p_N could also stay unchanged at some increase of d_N. The decision requires evaluation of the sign of $f(p_N,d_N+1)$.

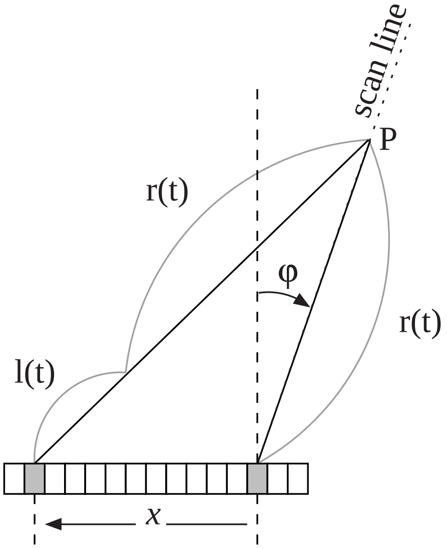
scan line
P
r(t)
φ
r(t)
l(t)
x

Figure 4.8: Delay calculation geometry for the LUCS delay generator.

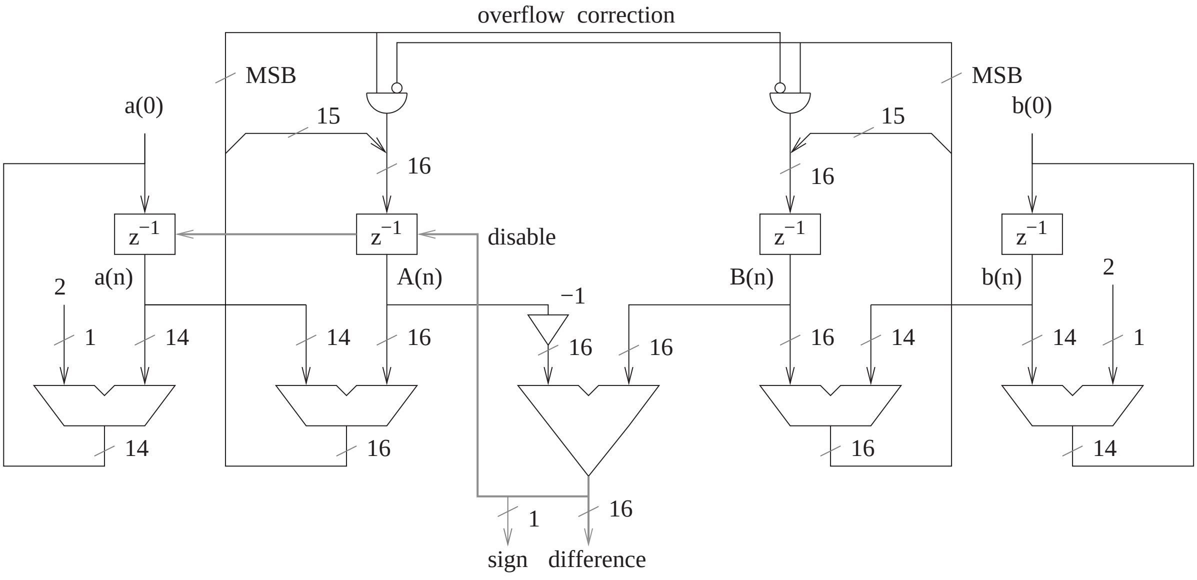
overflow correction
MSB
MSB
a(0)
b(0)
15
15
16
16
z^{−1}
z^{−1}
z^{−1}
z^{−1}
disable
a(n)
A(n)
B(n)
b(n)
2
2
−1
1
14
14
16
16
16
16
14
14
1
14
16
16
14
1
16
sign
difference

Figure 4.9: LUCS delay generator.

$$A(n+1) = A(n) + \underbrace{2n + 2k(n) + 1}_{a(n)}, \qquad A(0) = k^2(0) \tag{4.15}$$

$$B(n+1) = B(n) + \underbrace{2n + 1 + \alpha}_{b(n)}, \qquad B(0) = \beta \tag{4.16}$$

The update terms are calculated as:

$$a(n+1) = a(n) + 2, \qquad a(0) = 2k(0) + 1 \tag{4.17}$$

$$b(n+1) = b(n) + 2, \qquad b(0) = \alpha + 1; \tag{4.18}$$

Comparison between $A(n)$ and $B(n)$ determines whether $k(n)$ should be changed. Whenever $A(n) > B(n)$, $k(n)$ has to be decreased by one. It can be calculated that $A(n+1, k-1) = A(n,k)$ and $a(n+1, k-1) = a(n,k)$, therefore the consequence of decreasing k is skipping one update cycle of $A(n)$ and $a(n)$.

A block diagram of the algorithm is shown in Fig.4.9, with some example bus widths.

The overflow correction ensures that when the most significant bits (MSB) of both $A(n)$ and $B(n)$ are 1, then they both become 0. In this way, both expressions are represented with the same number of bits at all times. The bus width and the register width should be chosen so that the maximum value of $a(n)$ and $b(n)$ that can occur for some imaging setup will not cause overflow and loss of information.

One simplification that can be made with this algorithm is the following: In the beginning of a calculation it is assumed that the present parameters depict a point on the delay curve. Since only the difference between $A(n)$ and $B(n)$ matters, their initial values can be set to 0 without introducing an error into the further calculations. In this way β does not have to be used at all.

4.7 Comparison between approximation schemes

A comparison between approximation schemes for possible embedding in a compact beamformer was performed. The necessary memory amount, occupied logic resources and power consumption were estimated for a VHDL implementation in an FPGA for a target device XCV2000E by Xilinx. Approximately the same level of optimization was achieved in the designs. The parameters for the delay generation are given in Table 4.1.

The implementation results for the delay generation approaches are shown in Table 4.2. The power consumption was estimated at 40 MHz. The column labeled ”Speed” shows the estimation for the maximum operating frequency of the corresponding design. It can be seen that the general parametric approach occupies most logic, consumes most, and can not achieve high operation speed. The LUCS delay generator, on the other hand, performs very well, and provides additional bit of intersample precision with little overhead - only one comparator more is necessary (described in [30]). The piecewise-linear approximator is simple and fast, with the only drawback that it requires more memory than the parametric approaches. The delta encoding has far higher memory requirements and is not an option when compact beamforming is considered. This is the reason why it is not included in the comparison.

Parameter	**Value**
Speed of sound	1540 ms^{-1}
Transducer center frequency f_0	5 MHz
Sampling frequency f_s	140 MHz
Image type	phased array image
Number of channels	32
Transducer pitch	$\frac{\lambda}{2}$
Image depth, cm	15
Target precision, clock periods	± 1

Table 4.1: Parameters for the delay generation approximation approaches comparison

Approach	**Memory, bits**	**Logic, gates**	**Power, mW**	**Speed, MHz**
Piecewise-linear approx.	240	1125	7.8	184.9
General parametric gen.	48	2819	13.6	81.9
LUCS delay generator	48	2095	10.6	131.9

Table 4.2: Implementation results for delay generation approaches, per channel

4.8 Discussion

The delay generation methods presented are suitable for use in many contemporary imaging modalities, where the images are created line by line. Their particular strength is in compact implementation of ultrasound beamformers. For an imaging system with 64 channels that produces phased array images consisting of 90 lines, the necessary logic resource for the delay generation is 143040 gates, and the necessary memory is 4320 bits per channel (276480 bits in total), when the LUCS delay generator is implemented. These resources are available in the bigger FPGA devices nowadays. If the use of an external memory module is acceptable, then the piecewise-linear approximation can be used, with the benefit of less power consumption.

CHAPTER

FIVE

Delta-Sigma modulation A/D conversion

The interface to the environment is very important for signal-processing devices. In a digital system that processes and/or produces analog signals, the analog-to-digital and digital-to-analog converters are the gates through which the information flows. Their quality directly influences the overall quality of the device. There are two main types of A/D and D/A converters:

Nyquist-rate converters generate output values that have direct correspondence to the input signal values within the quantization error. Due to difficulties in realizing anti-aliasing and reconstruction filters, these converters are often selected to operate at rates that are several times higher than the Nyquist rate.

Oversampled converters operate at much higher data rates than the Nyquist rate. They have a low number of bits (often 1) and achieve the necessary signal-to-noise ratio (SNR) by filtering the quantization noise that is not in the signal bandwidth. While oversampling alone is not an effective way of increasing the SNR, the quantization noise can be pushed away from signal bandwidth by *noise shaping*. This is done in the Delta-Sigma ($\Delta\Sigma$) modulation[1] (DSM) converters, which are the ones people have in mind when they talk about oversampled converters.

The DSM converters are attractive due to their insensitivity to circuit imperfections, simplicity and compactness. Moreover, they are compatible with the digital integrated circuit fabrication technology. The only limiting factor for their use is the required high sampling frequency. Currently, all mass-produced digital audio and telecommunication equipment (modems) is based on DSM converters, and their mass use in video equipment is approaching.

There exist number of good introductory papers and books on DSM data conversion [33, 34, 35, 36, 37], but as a basis for ideas that are discussed further in the thesis, this chapter provides description of the operation principle of the DSM converters and shows derivations of some quantitative expressions for their performance. Also, the sample reconstruction is discussed and some more complex DSM architectures are introduced.

---

[1] The qualifiers *delta-sigma* and *sigma-delta* used with respect to oversampled converters mean the same and their usage varies with authors. In the current thesis, the term ”delta-sigma” is preferred, in accordance with the convention used in the book *Oversampling delta-sigma data converters. Theory, design and simulation* [33].

5.1 Principle of operation

In this section, a derivation of the characteristics of an oversampled converter will be made. First, the relation between signal-to-quantization-noise ratio (SQNR) and the resolution of a multi-bit Nyquist rate converter will be shown. Then, the SQNR figure for an oversampled and noise-shaping converter will be derived.

5.1.1 Signal-to-quantization-noise ratio (SQNR) of a multi-bit Nyquist-rate data converter

Quantization is a process of transforming the sample amplitude of a signal s into a discrete amplitude taken from a set of possible amplitudes. The spacing between the possible amplitudes is called a *quantum* or *step-size*.

Fig. 5.1 illustrates the quantization process. The signal to be quantized has been discretized in time by an appropriate sample-and-hold circuit. The quantizer approximates the input signal level with a level from within a predetermined set, and in the process introduces an error e defined as the difference between the input signal and the output signal. The error is called the *quantization error*. In this example the signals are assumed to be voltages (hence the amplitude axis is named u), but they can also be currents or charges.

The error introduced by a quantizer with step-size Δ is bound by $-\frac{\Delta}{2}$ and $\frac{\Delta}{2}$ if the quantizer is not overloaded by the input signal. Assuming that the input signal is rapidly varying, the error will be uniformly distributed between these limits, as illustrated in Fig. 5.2.

The probability density function can be described as follows:

$$p_e(u) = \begin{cases} \frac{1}{\Delta} & -\frac{\Delta}{2} < u \leq \frac{\Delta}{2} \\ 0 & \text{otherwise.} \end{cases} \tag{5.1}$$

As a result of that, the mean value of the error is zero and its power is equal to its variance, which is:

$$P_e = \sigma_e^2 = \int_{-\infty}^{\infty} u^2 p_e(u)\, du = \frac{1}{\Delta}\int_{-\frac{\Delta}{2}}^{\frac{\Delta}{2}} u^2\, du = \frac{1}{\Delta}\frac{u^3}{3}\bigg|_{-\frac{\Delta}{2}}^{\frac{\Delta}{2}} = \frac{\Delta^2}{12} \tag{5.2}$$

The dynamic range of a data converter can be expressed as the ratio of the signal power of a full scale signal to the quantization noise power, and it is equal to its signal-to-quantization-noise

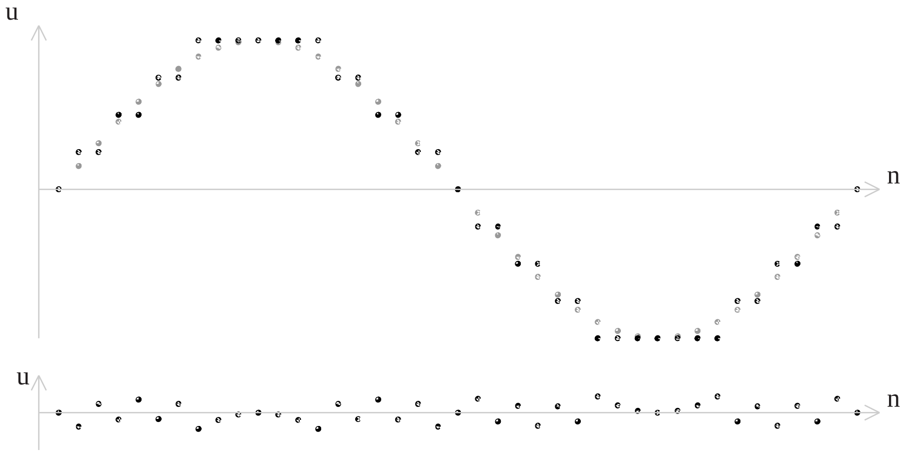

Figure 5.1: Quantization of a discrete analog sinusoidal signal (gray dots) results in coarse representation (black dots on the upper plot). The introduced quantization error, scaled up twice, is shown on the lower plot.

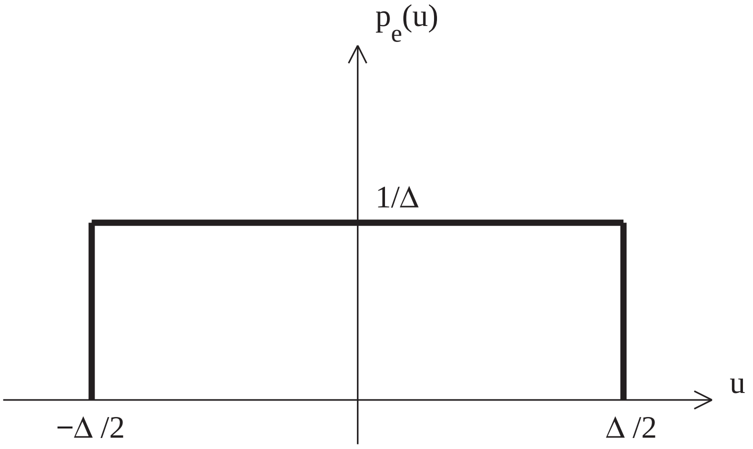

Figure 5.2: Assumed probability density function of the quantization error for an ”active” (rapidly varying) input signal.

ratio (SQNR). Usually, a sinusoid is used as a reference signal. A sinusoid is a periodic signal and its quantization error is also periodic, i.e. it does not justify the assumption of uniform distribution made above. Therefore, a stochastic signal with uniform probability density function within the input range of the data converter will be used as a reference signal. That signal justifies the above assumptions and introduces a minor simplification in the SQNR expressions, as will be seen further.

A converter with a word length of N [2] provides peak-to-peak amplitude of $\Delta 2^N$. Therefore, the maximum stochastic signal power is (by applying the same reasoning as for 5.2, with integral limits -$\frac{\Delta 2^N}{2}$ and $\frac{\Delta 2^N}{2}$):

$$P_s = \frac{(\Delta 2^N)^2}{12}. \tag{5.3}$$

The signal to noise ratio is (in dB)

$$SQNR = 10 \log \frac{\frac{(\Delta 2^N)^2}{12}}{\frac{\Delta^2}{12}} = 10 \log 2^{2N} \approx 6.02\, N \tag{5.4}$$

That formula shows that adding one bit to the digital word representing a signal corresponds to a 6 dB increase of the SQNR (the dynamic range) of the signal representation.

5.1.2 SQNR of oversampling converters

Oversampling converters is a name that also is often applied to delta-sigma modulation converters, although the latter incorporate noise-shaping features that improve the achievable signal-to-noise ratio. Pure oversampling converters without noise shaping are not practical, as will be shown further, and are not used. The nature and the benefits of the oversampling and the noise shaping are explained below.

Oversampling

The quantization noise power is independent of the sampling frequency f_s, as shown in Eq. 5.2. By oversampling (sampling high above the Nyquist rate), the quantization noise can be spread over a wider frequency band. The technique is illustrated in Fig. 5.3. Assuming white quantization noise, its power density is

$$k_e = \frac{P_e}{f_s} = \left(\frac{\Delta^2}{12}\right) \frac{1}{f_s} \tag{5.5}$$

For the purpose of expressing the degree of oversampling, the oversampling ratio (*OSR*) is introduced, and it is defined as:

$$OSR \equiv \frac{f_s}{2 f_0}, \tag{5.6}$$

---

[2] Regardless of whether the represented number is signed or unsigned, a binary word of width N provides the same number of levels - 2^N.

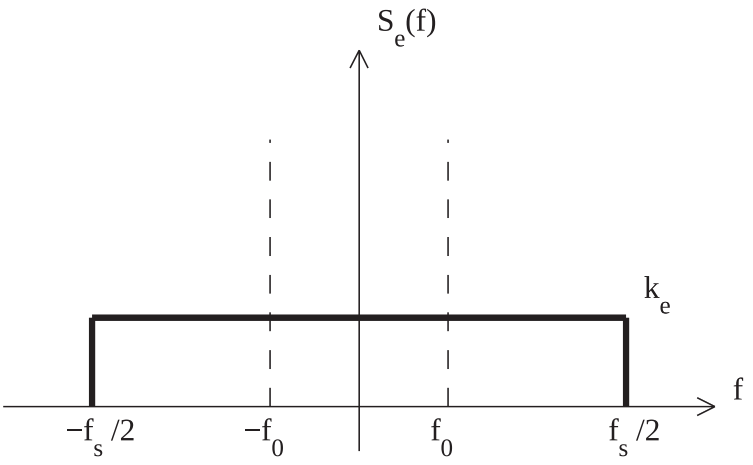

Figure 5.3: Assumed spectral density of the quantization noise. By filtering out the noise that lies outside the frequency band of interest, the noise power in the quantized signal is diminished.

where f_0 is the highest frequency in the band of interest and, accordingly, $2f_0$ is the Nyquist rate.

When filtered with a brick-wall low-pass filter from $-f_0$ to f_0, the noise outside the frequency band of the useful signal will be removed. The noise power within the signal frequency band is

$$P_e = \int_{-f_0}^{f_0} k_e \, df = \frac{2f_0}{f_s} \frac{\Delta^2}{12} = \frac{\Delta^2}{12} \frac{1}{OSR} \tag{5.7}$$

Using the maximum signal power from 5.3, the SQNR of the quantized signal is

$$SQNR_{os} = 10 \log \frac{P_s}{P_e} \approx 6.02\, N + 10 \log OSR \tag{5.8}$$

This result shows that the oversampling improves the *SNR* of a converter by 3 dB/octave, equivalent to 0.5 bits/octave. It should not be forgotten that such a gain can only be achieved for truly random signals, and should not be expected in case of slowly changing or periodic ones. Gaining 5 bits of resolution in this fashion requires *OSR* of $2^{\frac{5}{0.5}} = 1024$, which is impractical. Much better results are achieved by shaping of the quantization noise spectrum.

Quantization noise shaping

The quantization noise shaping in the A/D converters is achieved by having different transfer functions for the signal and the quantization noise. This can be realized through a feedback

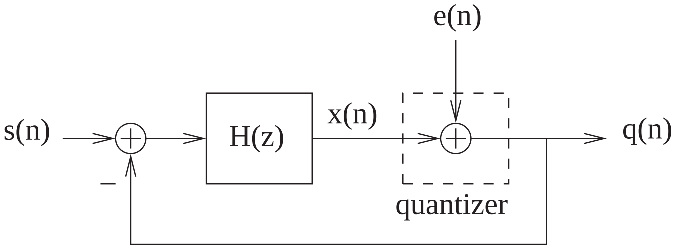

Figure 5.4: Noise-shaping modulator architecture

architecture shown in Fig. 5.4. Assuming that the signal and its quantization error are independent, the transfer functions for the signal, $S_{TF}(z)$, and the noise, $N_{TF}(z)$, can be expressed as:

$$S_{TF}(z) = \frac{Q(z)}{S(z)} = \frac{H(z)}{1+H(z)} \tag{5.9}$$

$$N_{TF}(z) = \frac{Q(z)}{E(z)} = \frac{1}{1+H(z)} \tag{5.10}$$

The quantized signal is a sum of the input signal and the quantization error, each filtered by its corresponding transfer function:

$$Q(z) = S_{TF}(z)S(z) + N_{TF}(z)E(z). \tag{5.11}$$

By choosing H(z) to be have a large transmission coefficient over the frequency band of interest, i.e. from 0 to f_0, $NTF(z)$ is close to zero in that band, and its value is inversely proportional to the gain of $H(z)$. At high frequencies, the noise is not attenuated, but it can be filtered out. The filtering is discussed in a subsequent section. For the purpose of deriving the basic DSM performance estimates, a brick-wall (ideal) filter will be assumed.

Since ideally the noise transfer function should be zero at low frequencies, $H(z)$ is chosen to be a discrete time integrator, described as

$$H(z) = \frac{1}{z-1}. \tag{5.12}$$

The corresponding quantizer architecture is shown in Fig 5.5.

The signal transfer function $S_{TF}(z)$ is

$$S_{TF}(z) = \frac{\frac{1}{z-1}}{1+\frac{1}{z-1}} = z^{-1} \tag{5.13}$$

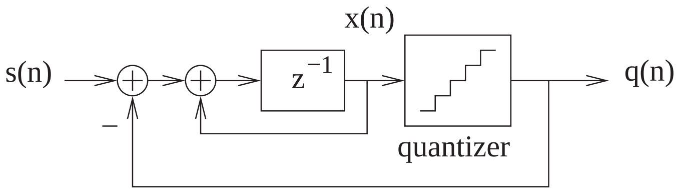

Figure 5.5: First order delta-sigma modulator

and the noise transfer function $N_{TF}(z)$ is

$$N_{TF}(z) = \frac{1}{1+\frac{1}{z-1}} = 1 - z^{-1}. \tag{5.14}$$

It can be seen that the signal transfer function is that of a delay of 1 clock period, while the noise transfer function is a discrete-time differentiator, i.e. high-pass filter. The frequency-domain representation of the latter can be obtained by letting $z = e^{j\omega T} = e^{j2\pi f/f_s}$ and using the following transformation:

$$\begin{aligned} N_{TF}(f) &= 1 - e^{j2\pi f/f_s} = e^{-j\pi f/f_s}e^{j\pi f/f_s} - e^{j\pi f/f_s}e^{j\pi f/f_s} \\ &= \frac{2j}{2j}(e^{-j\pi f/f_s} - e^{j\pi f/f_s})e^{j\pi f/f_s} \\ &= \frac{e^{-j\pi f/f_s} - e^{j\pi f/f_s}}{2j}e^{j\pi f/f_s}2j = \sin(\frac{\pi f}{f_s})2je^{j\pi f/f_s} \end{aligned} \tag{5.15}$$

The magnitude of that expression is

$$|N_{TF}(f)| = \left|2\sin(\frac{\pi f}{f_s})\right|, \tag{5.16}$$

The transfer functions for the signal and the quantization noise are illustrated in Fig.5.6

Using a brick-wall filter from $-f_0$ to f_0, the noise power in the signal frequency band is calculated as integration of the shaped noise power over that band:

$$P_e = \int_{-f_0}^{f_0} k_e|N_{TF}(f)|^2\,df = \int_{-f_0}^{f_0} \frac{\Delta^2}{12}\frac{1}{f_s}\left[2\sin(\frac{\pi f}{f_s})\right]^2 df \tag{5.17}$$

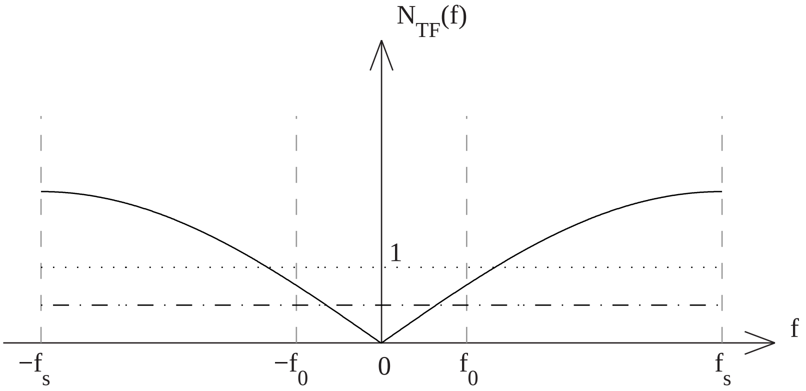

Figure 5.6: Noise transfer functions for oversampling only (dash-dotted) and first-order noise-shaping (solid line) A/D converters. The signal transfer function is constant one (dotted line). The level of the oversampling only quantization noise and the f_0 is shown for OSR = 4.

For $f \ll f_s$, i.e. high OSR, $\sin\left(\frac{\pi f}{f_s}\right)$ can be approximated with $\frac{\pi f}{f_s}$, therefore

$$P_e = \frac{\Delta^2}{12}\frac{\pi^2}{3}\left(\frac{2f_0}{f_s}\right)^3 = \frac{\Delta^2\pi^2}{36}\left(\frac{1}{OSR}\right)^3. \tag{5.18}$$

Using the signal power expression from (5.3), the SQNR can be written as:

$$SQNR_{1st} \approx 6.02\,N - 5.17 + 30\log OSR \tag{5.19}$$

The gain using oversampling with first-order noise shaping is 9 dB/octave, equivalent to 1.5 bits/octave. This is 6dB/octave (1 bit/octave) more than what the oversampling alone can provide.

Second-order noise shaping

By adding a second integrator to the first order modulator, the noise shaping can be improved. The resulting structure is shown in Fig. 5.7.

The signal transfer function $S_{TF}(z)$ for this architecture is [37]

$$S_{TF}(z) = z^{-1} \tag{5.20}$$

and the noise transfer function $N_{TF}(z)$ is

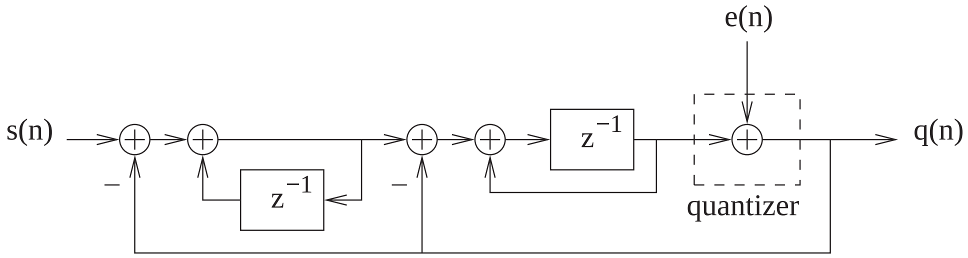

Figure 5.7: Second order delta-sigma modulator

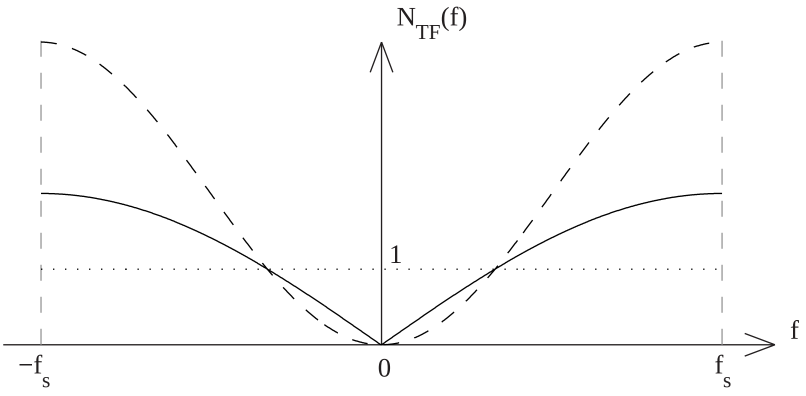

Figure 5.8: Noise transfer functions for first-order noise-shaping (solid line) and second-order (dashed line) delta-sigma modulators. The signal transfer function is constant one (dotted line).

$$N_{TF}(z) = (1 - z^{-1})^2 \tag{5.21}$$

Its magnitude in the frequency domain is (See Fig. 5.8)

$$|N_{TF}(f)| = \left[2sin(\frac{\pi f}{fs})\right]^2, \tag{5.22}$$

and the noise power within the signal frequency band is

$$P_e = \frac{\Delta^2 \pi^4}{60}\left(\frac{1}{OSR}\right)^5. \tag{5.23}$$

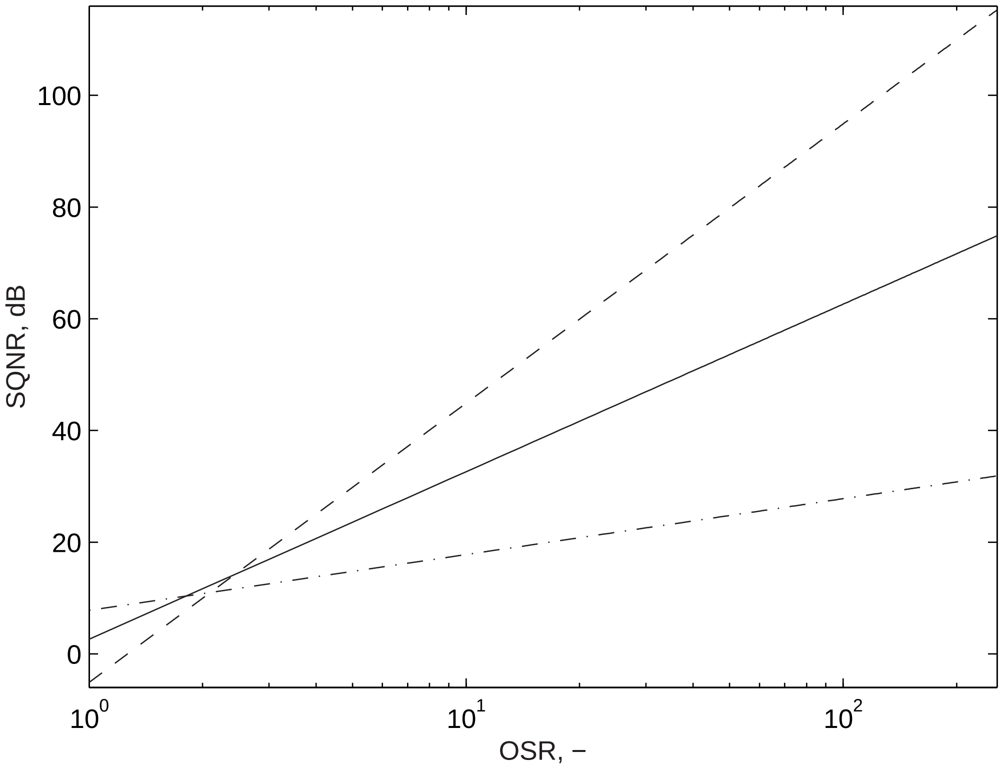

Figure 5.9: Theoretic SQNR curves for oversampling only (dash-dotted), first-order noise-shaping (solid line), and second-order noise-shaping (dashed line) A/D converters.

Using the signal power expression from (5.3), the SQNR is written as

$$SQNR_{2nd} \approx 6.02\,N - 12.9 + 50\log OSR \tag{5.24}$$

The gain using oversampling with second-order noise shaping is 15 dB/octave, equivalent to 2.5 bits/octave.

For illustrating of the performance of first- and second-order modulators, the theoretic SQNR curves of the discussed modulators as a function of *OSR* are shown in Fig. 5.9. It can be seen the a higher-order modulator provides the desired SQNR at lower OSR. Higher order modulator structures will be discussed further.

5.2 Sample reconstruction

In all mass applications of the DSM A/D converters, they are used instead of multi-bit converters that sample at regular intervals in time (uniform sampling). The sample rate of the DSM A/D converters is much higher than Nyquist rate. The best sample reconstruction method is applying a brick-wall low-pass[3] filter on the DSM bit-stream and decimating the filtered output, or applying the filtering operation on selected portions of the DSM bit-stream, at the exact times when the low-rate output samples have to be produced. This technique requires additions and multiplications at high rate. For avoiding that, comb filters plus decimation are used in consecutive stages. The last filter is usually a FIR filter that compensates for the distortions introduced by the preceding simpler filters.

In real life, ideal brick-wall filter can not be realized. Therefore, the achievable SQNR will be less than the value calculated in the previous section. The exact value of the SQNR, though, can be calculated if the transfer function $H_{rc}(f)$ of the reconstruction filter is known. The noise power can be calculated as

$$P_e = \int_{-\inf}^{\inf} k_e |N_{TF}(f)|^2 H_{rc}(f)^2 \, df \tag{5.25}$$

and the obtained value can be used for deriving a precise SQNR. Still, the formulae are valid only for stochastic, active, non-periodic signals.

5.3 Higher-order noise shaping and band-pass modulators

Higher order modulators exist, which implement better noise shaping. Their design is not straightforward due to stability problems. In general, their input signal amplitude has to be reduced for stable operation, or a multi-bit quantizer used, which removes the advantage of the inherent linearity of the 1-bit quantizer. With high order DSM, the output word is often wider than 1 bit.

By using appropriate $H(z)$, the noise can be pushed away from selected frequency. The technique is called band-pass DSM and is widely used in digital radio applications (mobile communications). Band-pass filters are used for reconstructing the samples.

---

[3] In this section, low-pass DSM structure is considered. For a band-pass DSM, the reconstructing filter should be band-pass.

CHAPTER

SIX

DSM beamformer

The use of 1-bit oversampled ADC and DAC in ultrasound scanners can provide the same benefits that it brought to the telecommunication and audio applications - inexpensive data conversion and compactness. Although the medical imaging systems have no potential of becoming a mass product due to the specific knowledge and experience required from the operators, the cost, size and weight reduction can make them more affordable and more practical for use outside the clinical environment. This chapter will provide an overview of the research in the area of oversampled beamformers and will introduce a new architecture that offers improved image quality and flexibility.

6.1 Previous approaches for utilizing DSM in beamformers

The oversampling conversion offers several advantages over the use of multi-bit ADC in ultrasound beamformers. First, the modulators can be integrated in large numbers on a chip, with the requirement of one input and one-bit output per modulator. Second, the inter-sample interpolation that is necessary with multi-bit flash ADC can be avoided since the delay resolution of a DSM beamformer is determined by the sampling rate of the modulators. The latter is inherently high. Third, the time gain compensation and/or channel weighting can be incorporated to a certain degree in the modulator by varying the amplitude of the feedback voltage (up to 25 dB of useful dynamic range has been reported [38]).

A block diagram of an oversampled converter is shown in Fig. 6.1(concept from [39]). By performing the sample reconstruction after the coherent sum across channels, significant savings in logic resources/area can be made. Although the reconstruction in this case is applied on a multi-bit stream, the implementation is still more compact than in the case where separate sample reconstruction is performed on each channel.

Dynamic focusing in receive can be realized by means of sample buffer with variable length. The easiest way of adjusting the inter-element delay is to drop or repeat samples in the modulator output stream. On the other hand, the samples produced by an oversampled A/D converter

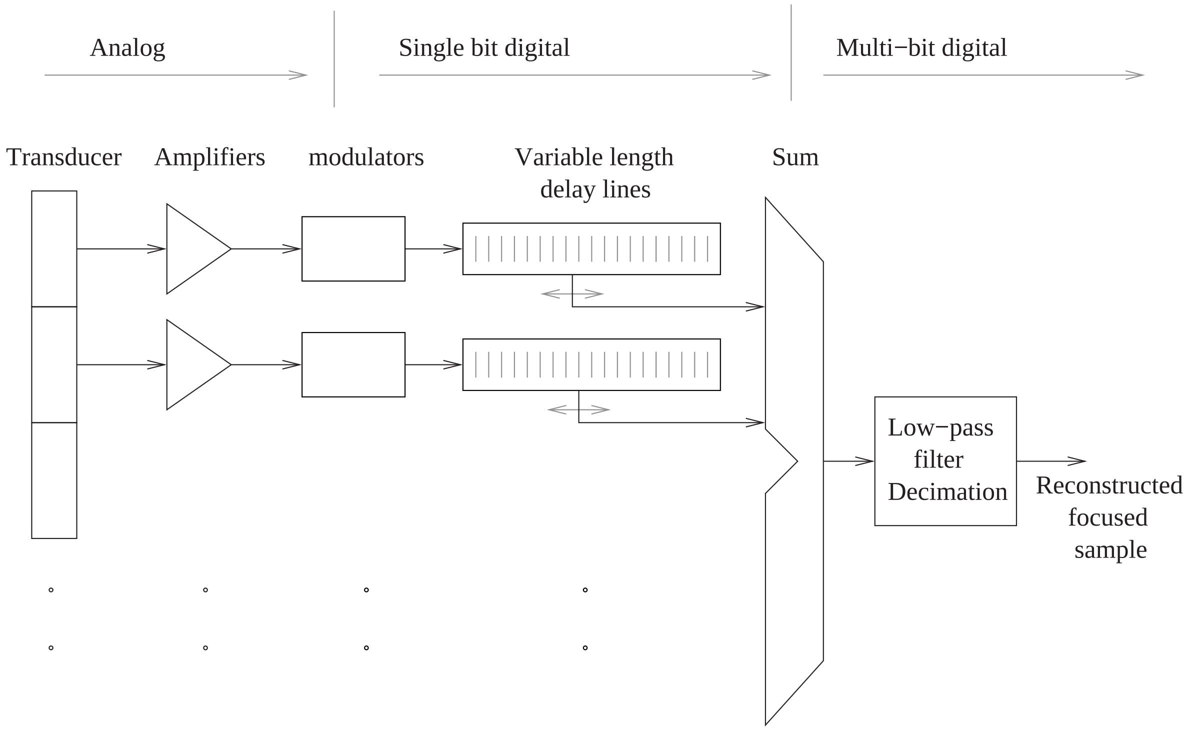
Analog
Single bit digital
Multi−bit digital
Transducer
Amplifiers
modulators
Variable length delay lines
Sum
Low−pass filter Decimation
Reconstructed focused sample

Figure 6.1: Block diagram of an oversampled beamformer.

are representative of the input signal only if the modulator output stream is not distorted. An oversampled beamformer that uses the described simple way of adjusting the delays introduces errors due to the repetition or skipping of samples.

6.1.1 Modified modulator architecture for compensation of sample drop or insertion

The efforts of Freeman et al. [39] led to the development of a modified modulator architecture, in which the feedback of the modulator is controlled by the delay logic of the beamformer. Whenever the delay has to be increased, 1) a neutral sample value is inserted or 2) a sample is split into two in the modulator output stream. For that purpose, recoding techniques are used as shown in Tables 6.1 and 6.2.

The described recoding techniques provide means for inserting a neutral sample value or splitting a sample value in the output stream. In both cases the feedback path does not require modification, while in case of repeating a sample, double sample value has to be fed back. The additional logic that is inserted into the modulator structure as shown in Fig. 6.2.

Whenever the delay has to be decreased, a sample is dropped or summed with the next one in

Modulator stream	Digital level	New coding unsigned	New coding signed
1	+1	10 (2)	01 (1)
0	-1	00 (0)	11 (-1)
New level	0	01 (1)	00 (0)

Table 6.1: Digital recoding techniques for inserting a zero sample

Modulator stream	Digital level	New coding unsigned	New coding signed
1	+1	100 (4)	010 (2)
New level	+0.5	011 (3)	001 (1)
New level	-0.5	001 (1)	111 (-1)
0	-1	000 (0)	110 (-2)

Table 6.2: Digital recoding techniques for inserting a sample in half

the bit stream. In both cases the modulator feedback is set to neutral value (0), as shown in Fig. 6.3.

The approach has been reported to compensate to a large extent the for the disruption of the modulation process by the focusing. The inherent drawback is that the output word width is increased by one bit.

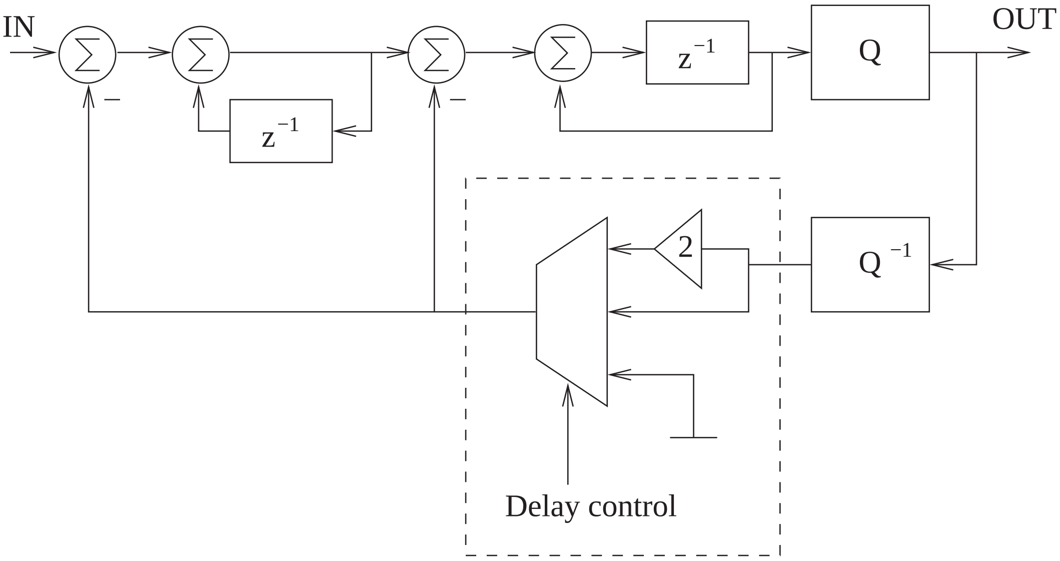

Figure 6.2: Modified modulator structure for compensating of delay increase

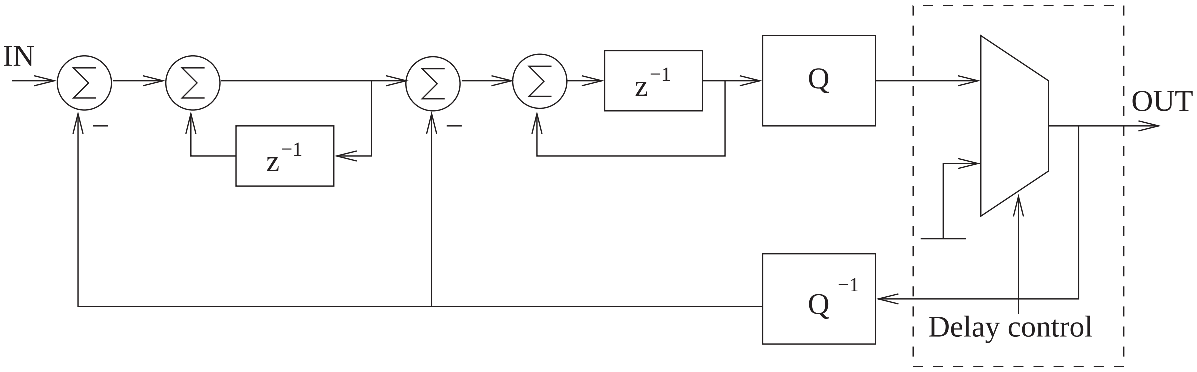

Figure 6.3: Modified modulator structure for compensating of delay decrease

6.1.2 Use of non-uniform sampling clock

Fig. 6.4 illustrates how during dynamic focusing (with changing delay between channels) some values from the bit streams have to be used twice while others have to be omitted. Kozak and Karaman [40] have proposed sampling with a non-uniform (gated) sampling clock, specific for each channel so that the delays are incorporated and all channels produce the same number of samples per image line.

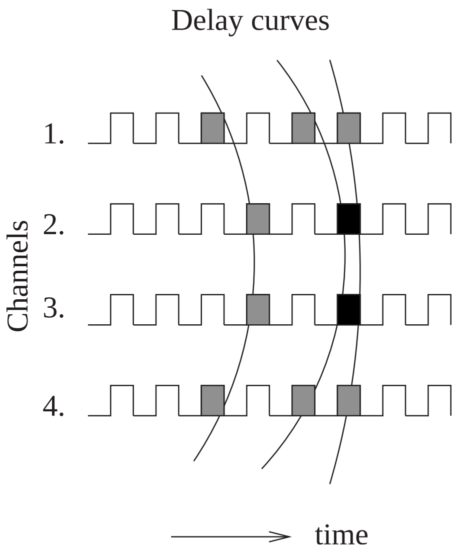

Figure 6.4: Illustration of delay profile coincidence with data values on different channels

A block digram of the architecture that realizes that concept is shown in Fig. 6.5. The performance of such an imaging system is below that of an uniformly sampling system, since the non-uniform sampling degrades the SQNR.

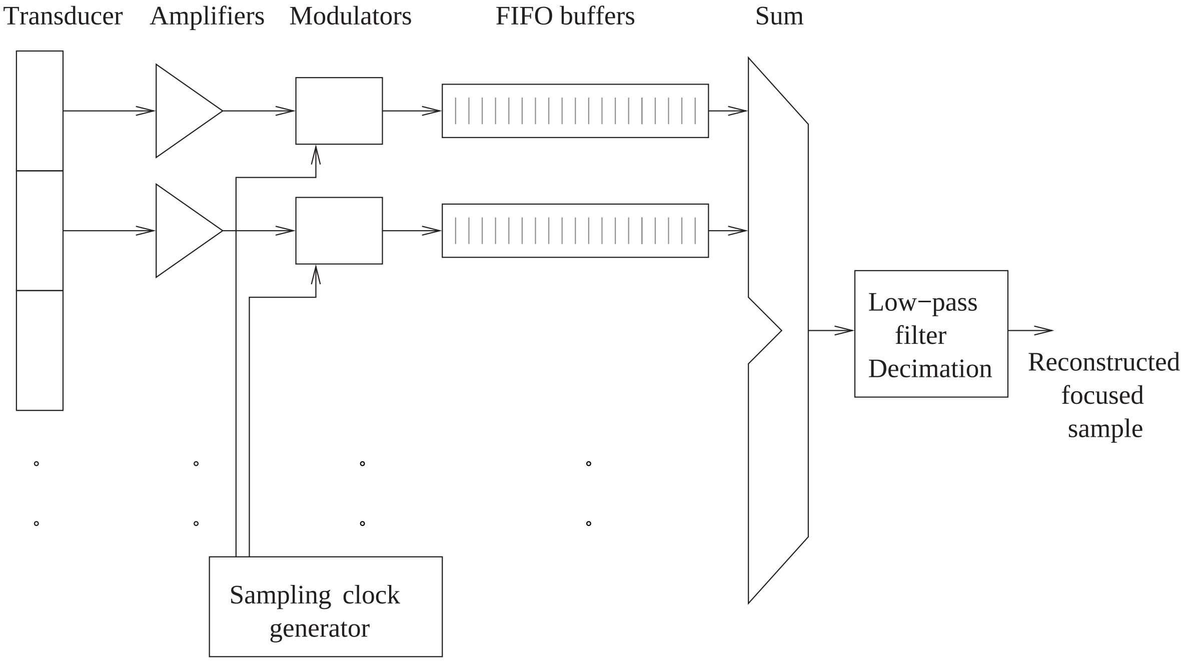
Transducer
Amplifiers
Modulators
FIFO buffers
Sum
Low−pass filter Decimation
Reconstructed focused sample
Sampling clock generator

Figure 6.5: Block diagram with of a oversampled beamformer utilizing non-uniform sampling clock

6.2 New architecture for an oversampled beamformer

A new oversampled beamformer architecture has been developed where disruption of the delta-sigma modulation process is avoided by reconstructing the samples with a digital FIR filter. For reducing the number of the calculations, only the samples needed for display are reconstructed by obtaining the echo signal for both the in-phase and quadrature components at equidistant depths along the image lines. The features and the performance of the architecture are presented below.

6.2.1 Sparse sample processing concept

In a digital beamformer, several thousand samples are processed for each image line. The ultrasound images are shown on raster displays, which rarely have a vertical resolution beyond that of a TV (525 lines for NTSC) or VGA (640x480 pixels). Processing only the necessary data for about 500 points provides large savings in consumed power, and allows for lower processing rate. The concern here is whether the reduced number of points provides (visually) the same information as the thousands of points in conventional beamforming.

Sparse sample processing in the form of pixel-based focusing was proposed by Karaman et al. [41]. According to that approach, the focal points for which samples are produced correspond to the raster display pixels. These do not lie on the beam axis (unless linear array imaging is performed) and therefore the information for the focusing is hard to derive in a recursive fashion. The present approach processes samples that correspond to equidistant focal points lying on the beam axis. In this way, it is possible to calculate the focusing information in a recursive fashion.

For an imaging situation where the frequency-dependent attenuation in tissue is a dB/(cm·MHz) and the compensation range (time-gain compensation) of the imaging system is A dB, the image depth with high dynamic range can be calculated as

$$d = \frac{A}{2af_0}, \tag{6.1}$$

where f_0 is the utilized frequency. The image depth, expressed in wavelengths ($\lambda = c/f_0$) of the central frequency, is

$$d_\lambda = \frac{d}{\lambda} = \frac{A}{2ac}, \tag{6.2}$$

and is independent of the transducer frequency used. For a typical image situation where the attenuation coefficient in tissue is 0.5 dB/(cm·MHz), the TGC range is 60 dB and the speed of sound is 1540 m/s, d_λ is 390. Beyond that depth, the dynamic range of the image gradually decreases until the image becomes too noisy to be of any practical value. If the SNR at the quoted depth is 60 dB, it will be exhausted after the same distance as above and the image depth can be at most 780λ.

In case that the signal is reconstructed in 512 points within the high dynamic range area, the spacing between them is 0.76 λ. For the worst case, the spacing is 1.52 λ. These distances are calculated for a relatively weak tissue attenuation. Taking into account a higher value for the attenuation (1 dB/(cm·MHz) is more realistic) will lead to lower estimate for the achievable image depth and the lower focal point spacing.

The axial resolution of an imaging system can be evaluated by producing the processed echo from a point reflector. The echo signal is the excitation waveform convolved twice with the transducer impulse response. The matched filter applied on the received RF data has the same shape as the expected echo signal. The image data is produced by filtering the echo signal with the matched filter and calculating the envelope of the result. For a case where the excitation waveform is one period of a sinusoid at a central frequency f_0 and the transducer has the same central frequency and 60 % bandwidth at -6 dB, the imaging system axial resolution at -3 dB is 1.87 λ and is 2.67 λ at -6 dB. These distances are larger than the spacing calculated above, and no image information is lost due to the sparse sample processing.

As is the case for the classic beamforming, the reconstruction of the envelope of the signal requires its in-phase and quadrature components. In the sparse sample processing approach, the quadrature signal cannot be produced by filtering of the in-phase signal because the latter is an undersampled representation of the echo signal. Therefore both components have to be created at the same stage. This is achieved by using in-phase and quadrature reconstruction filters, as will be explained further.

6.2.2 Signal processing

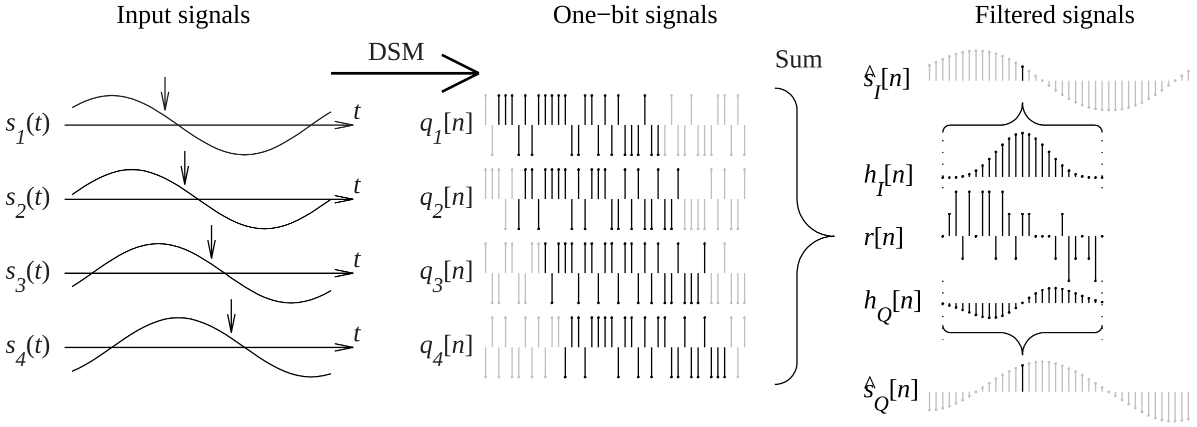

Figure 6.6: Signal processing of the proposed beamformer, illustrated with 4 channels

The signal processing is illustrated in Fig. 6.6. The analog input signals $s_k(t)$ (k is channel index) from different channels are converted into one-bit streams $q_k[n]$ in the DSM. In order to sum the echoes coming form a certain focal point (indicated by arrows in the plots of $s_k(t)$), sequences of bits (shown in black) are selected from the streams $q_k[n]$. Their positions correspond to the required channel delays. The length of the sequences is equal to the length of the reconstruction filters that will be used. The selected sequences are summed into a sequence $r[n]$. The latter is then filtered by the in-phase $h_I[n]$ and quadrature $h_Q[n]$ reconstruction filters to yield in-phase $\hat{s}_I[n]$ and quadrature $\hat{s}_Q[n]$ components of the signal from the chosen focal point. In the figure, all possible reconstructed in-phase and quadrature are shown, in gray. With the chosen sparse sample processing, only every 30th (for example) sample has to be produced.

6.2.3 Choice of reconstruction filter

In general, the DSM reconstruction filter has to be inversely matched to the noise transfer function (NTF) of the modulator, e.g. if the NTF is band-rejecting (pushing noise away form a

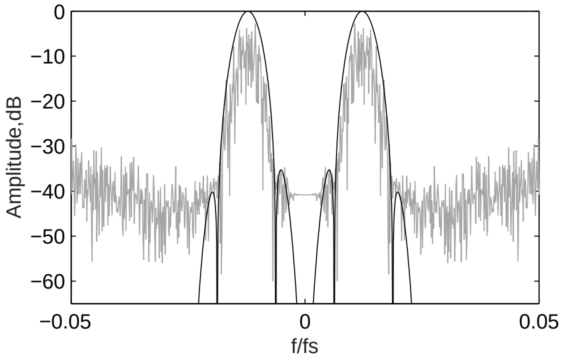

Figure 6.7: DSM output spectrum (gray) with frequency response of the matched filter (black) for OSR=20.

given center frequency), the filter should be band-pass with the same center frequency.

The best filter for a known signal in the presence of white noise is the matched filter, which is a time-reversed and delayed version of the expected signal [42]. In an ultrasound beamformer, the expected signal is the transmitted excitation, convolved twice with the impulse response of the transducer. Since the amplifiers in transmit and receive have much greater bandwidth than the transducer, their impulse response is not a limiting factor and is not taken into account here.

The matched filter for the expected echo signal should be able to filter out the quantization noise, since it has a band-pass transfer function centered around the central frequency of the useful signal, as shown on Fig. 6.7. The transfer function of the matched filter drops below -60 dB for frequencies above twice the central frequency. Therefore the matched filter, sampled at the DSM sampling frequency, is used as an in-phase reconstruction filter, and a Hilbert transformation of it is used as a quadrature reconstruction filter.

6.2.4 Calculation of the necessary oversampling ratio

A beamformer was designed, with target parameters shown in Table 6.3.

Using the formulae given in Subsection 3.2.3, the desired delay quantization induced sidelobe level is used for calculating the necessary delay precision. For the particular case, the values were derived as follows: In the near field the random quantization sidelobes are prevalent and for achieving sidelobe of -60 dB, the necessary sampling frequency is 25.6 times the central frequency of the ultrasound pulse (76.8 MHz), yielding -30 dB sidelobe level in transmit and -30 dB sidelobe level in receive.

Apart from the sidelobe level, the sampling frequency also determines the level of the quantization noise. The quantization noise power of a single multi-bit ADC with a quantization step

Parameter	**Value**
Speed of sound	1540 ms^{-1}
Transducer center frequency f_0	3 MHz
Excitation	2 periods of a sinusoid at f_0
Target image SNR	60 dB
Target delay quantization sidelobe level	60 dB
Image type	phased array image
Number of channels	32
Transducer center frequency	3 MHz
Transducer pitch	0.26 mm
Transducer elevation focus	7 cm
Image depth	15 cm.

Table 6.3: Target beamformer parameters.

δ is

$$P_{qe} = \frac{\delta^2}{12}, \tag{6.3}$$

if the noise is white, as it is assumed here. The coherent sum of the signals across the array would sum up the signal amplitudes and the channel noise powers. Therefore the gain of the SNR in the summed signal will be determined by the apodization profile as follows:

$$G_{SNR} = \frac{\sum_{n=1}^{N} w_n}{\left[\sum_{n=1}^{N} w_n^2\right]^{\frac{1}{2}}}. \tag{6.4}$$

For example, a 32-channel array with Hamming apodization can provide $G_{SNR} = 13.6$ dB, while uniform apodization yields 15 dB. That gain in SNR relieves the requirements toward the sampling frequency.

Having the requirement for 60 dB signal SNR after summation, and array SNR contribution of 13.6 dB, the channel SNR has to be 60-13.6 = 46.4 dB. Using a second order DSM, the necessary OSR ($= \frac{f_s}{2\,BW}$) is: $OSR_2 = 10^{\frac{SNR-6.02-1.76+12.9}{50}} = 10.7$. Therefore the sampling frequency has to be 21.4 times the bandwidth of the ultrasound pulse. In this particular case, the bandwidth of the signal is assumed to be 60 % around the central frequency (± 30 %) at -6 dB, i.e 2.1 to 3.9 MHz. Since a low-pass modulator is used, the bandwidth is considered to span from DC, i.e. $BW = 3.9$ MHz. Therefore the necessary sampling frequency is $f_s = 2 \cdot OSR_2 \cdot 3.9 = 83.6$ MHz.

Since an expanding aperture may be used, starting from a couple of channels around the beam origin, two channels have to be able to provide 60 dB of SNR. Therefore the OSR has to be 17.5 and the sampling frequency has to be 136.3 MHz.

Parameter	**Value**
Speed of sound	1540 ms^{-1}
Transducer center frequency f_0	3 MHz
Sampling frequency f_s	140 MHz
Excitation	2 periods of a sinusoid at f_0
Number of channels	32
Transducer pitch	0.26 mm
Transducer elevation focus	7 cm
Image depth	15 cm.
Transmit apodization	uniform
Transmit focus depth	7 cm
Receive apodization	Hamming window
Receive focus	dynamic
Image type	Phased array image
Image sector	90 degrees
Number of lines	135

Table 6.4: Simulation parameters

The chosen target sampling frequency is 140 MHz.

6.2.5 Simulation results

The ultrasound field simulation program Field II [27] was used for generating echo data from scatterers at different depths. The simulation parameters are given in Table 6.4. The echo signals were then beamformed using conventional beamforming and using DSM beamformer.

Point spread function

A comparison with a reference beamformed PSF is shown in Fig. 6.8 and Fig. 6.9. As can be seen, the resolution is approximately the same, while the noise level in the DSM beamformation is at about -60 dB due to quantization noise.

Blood flow simulation

Due to the sparse sample processing, flow estimation on the DSM beamformed data form this architecture can only be performed using the autocorrelation approach. The parameters of the simulated flow phantom are given in Table 6.5.

Parameter	**Value**
Tube radius	0.01 m
Tube length	0.04 m
Tube center depth	0.04 m
Tube slope	45 degrees
Flow profile	parabolic
Maximum blood velocity	0.5 ms^{-1}
Number of scatterers	3939

Table 6.5: Simulated flow parameters

The results from flow estimation using conventionally beamformed data and DSM beamformed data are shown in Fig. 6.10.

The drops in the estimated velocity profiles are due to the used blood flow presence criterion. It can be seen that the shapes of the velocity profiles for a given number of shots are similar, which shows that the DSM beamforming with sparse sample processing can successfully replace the conventional beamforming.

6.2.6 Phantom data processing results

A set of element traces sampled at 40 MHz was obtained using the experimental sampling system RASMUS [17] and a Vermon phased array transducer. That data was re-sampled at 140 MHz, and was beamformed according to the suggested signal processing. The results are shown in Fig. 6.11. The difference from the simulation setup is in that the number of elements is 40 and their pitch is 0.22 mm.

6.3 Discussion

The suggested architecture avoids modulation disruption and does not have any special requirements toward the modulators. The FIR filters, being the most complex stage in the architecture, will determine the achievable operation frequency of the beamformer in any given hardware implementation.

The simulated point-spread functions indicate that the resolution is approximately the same (visually indistinguishable in an image), while the noise level in the DSM beamformation is at about -60 dB due to quantization noise.

The flow estimation performance of the architecture is comparable to that of a conventional beamformer. It is noticeable that the blood velocity profile obtained with oversampled beamforming closely follows the shape of the one obtained by conventional beamforming. That fact indicates that the oversampled beamformer does not introduce distortion into the signal processing. The difference between the two profiles can be attributed to the additional noise (the remaining quantization noise after filtering) which is present in the signal produced by the oversampled converter.

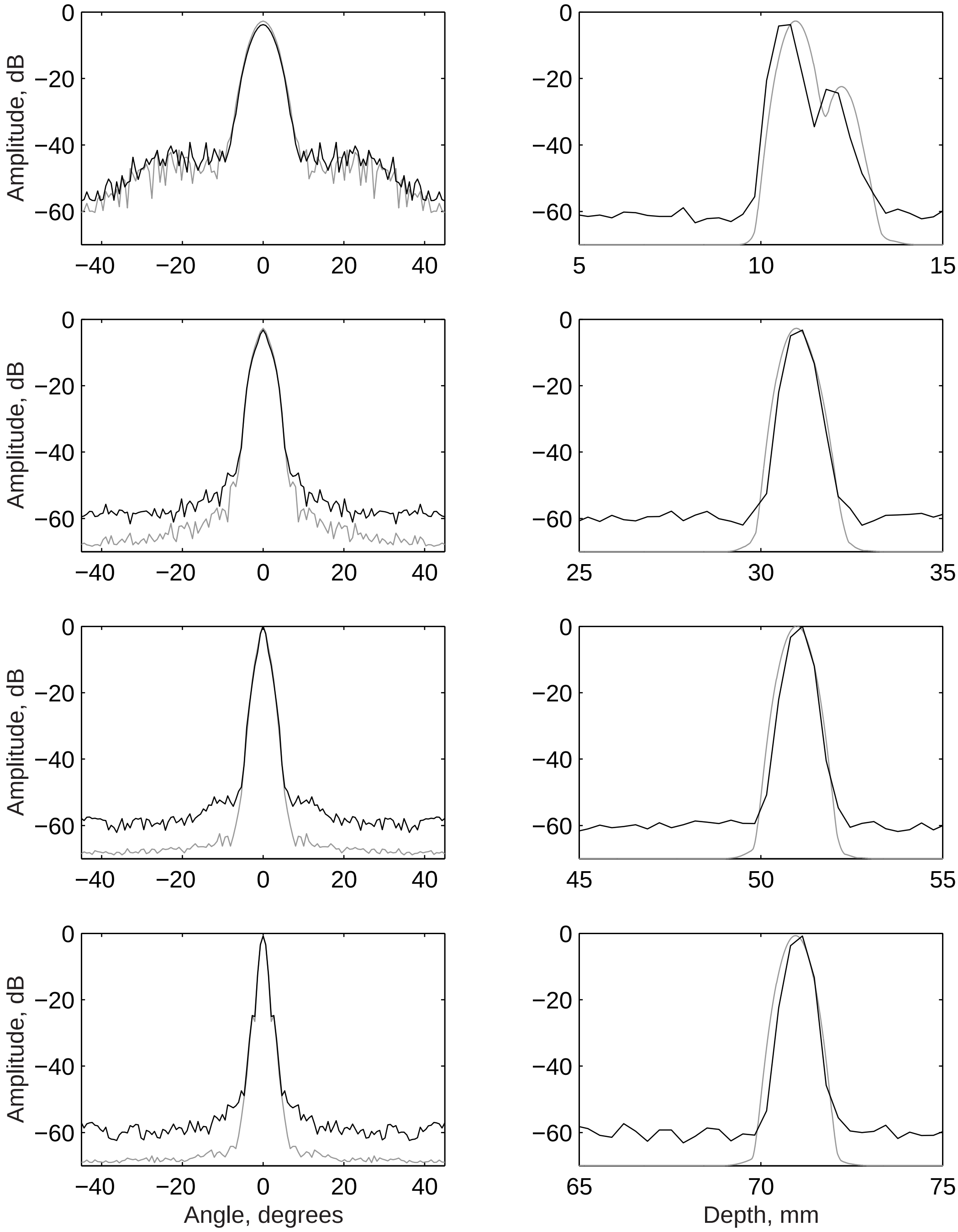

Figure 6.8: Simulated PSF: classic beamforming (grey), DSM beamforming (black) for depths of 1,3,5, and 7 cm.

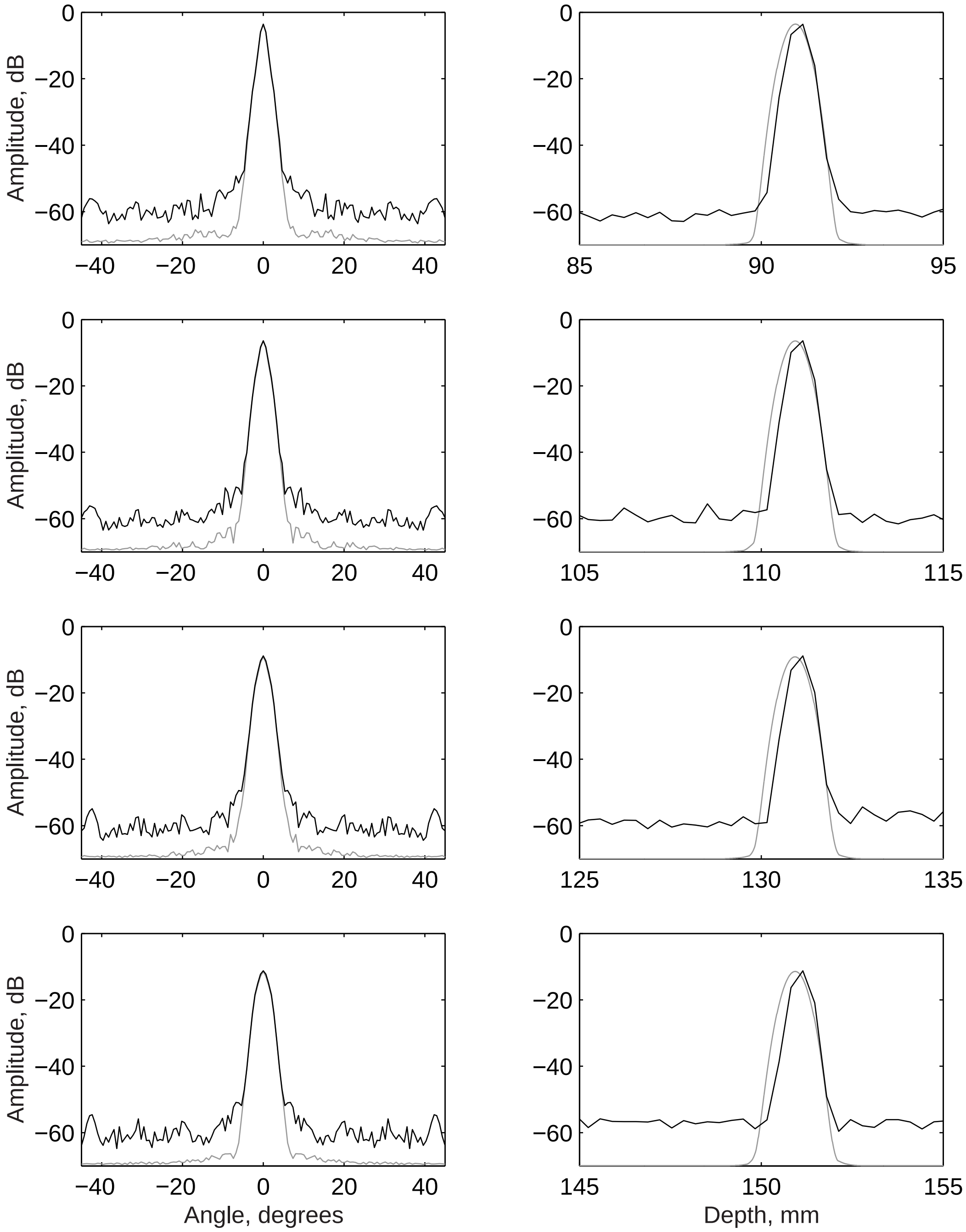

Figure 6.9: Simulated PSF: classic beamforming (grey), DSM beamforming (black) for depths of 9,11,13, and 15 cm.

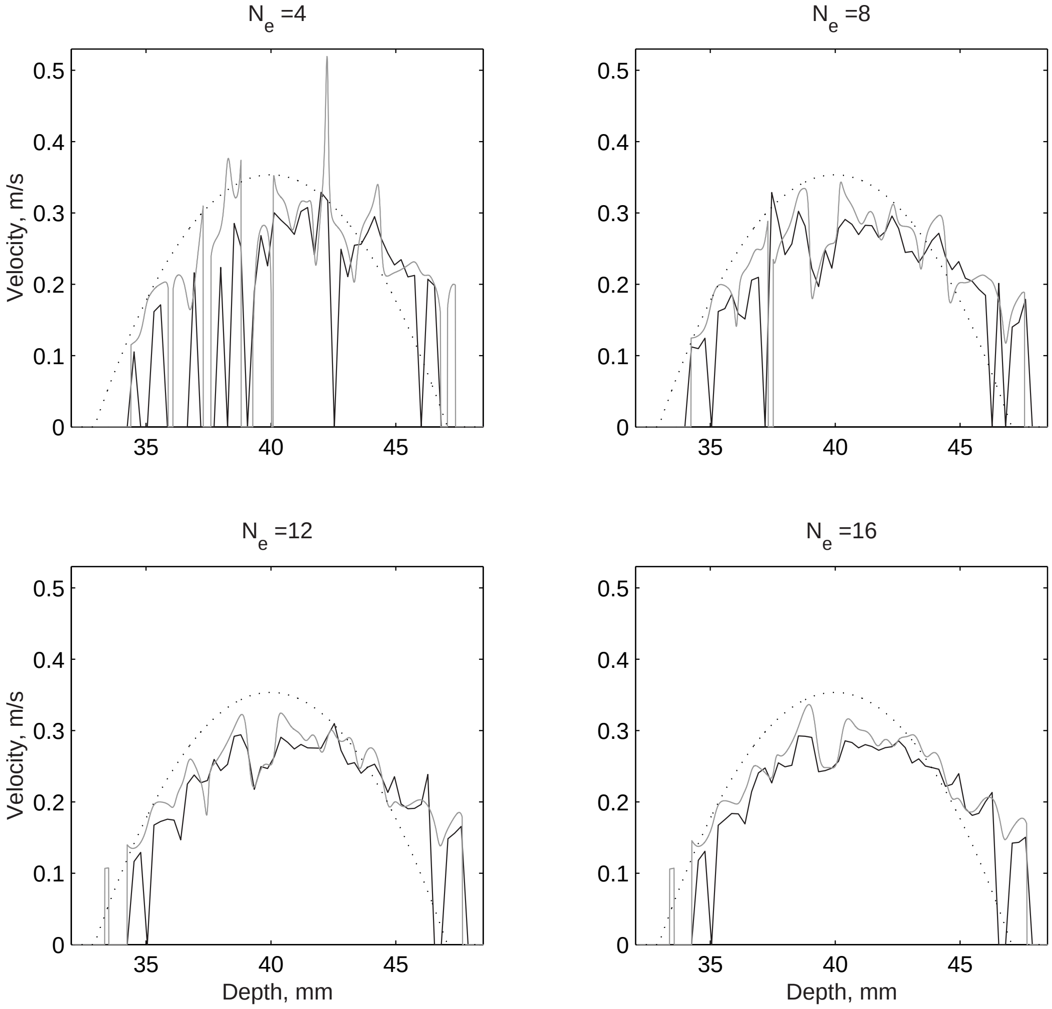

Figure 6.10: Velocity profiles obtained using different numbers of shots. The real velocity profile is drawn with dotted line. The flow estimate from conventional beamformed data is drawn in gray. The flow estimate from DSM beamformed data is drawn in black.

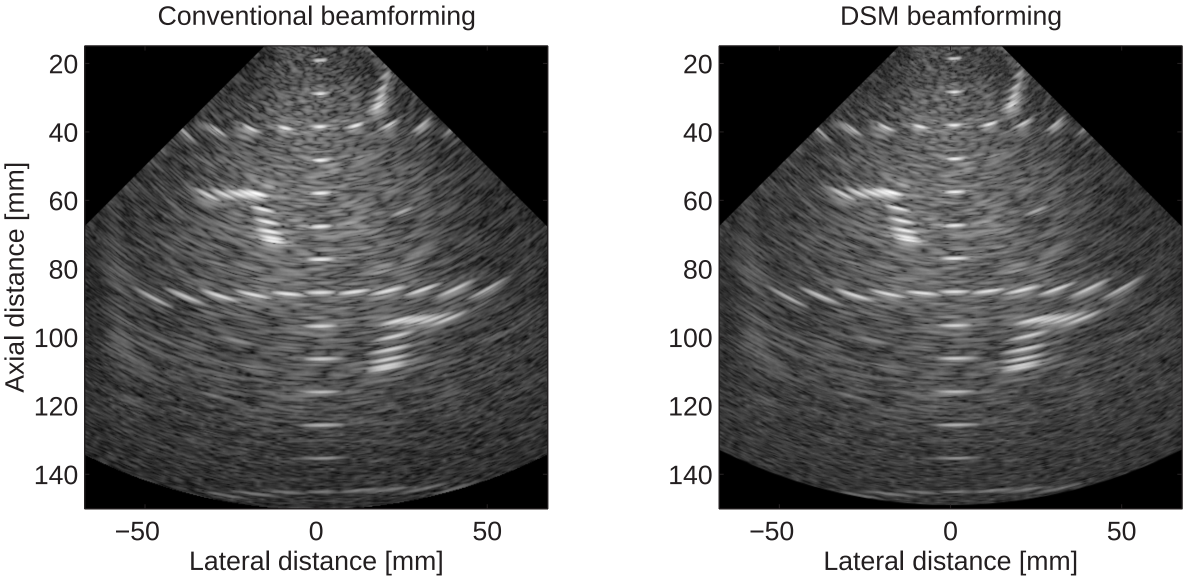
Conventional beamforming
DSM beamforming
Axial distance [mm]
20
40
60
80
100
120
140
−50
0
50
Lateral distance [mm]

Figure 6.11: Image created using classic phased array beamforming and DSM phased array beamforming. Dynamic range: 60 dB

CHAPTER

SEVEN

Implementation

As a means for evaluating the performance of the sparse sample processing beamformer, it was described in VHDL and synthesized for an FPGA device XCV2000E-7 by Xilinx. The chosen implementation parameters are shown in Table 7.1.

The following beamformer parameters were chosen:

The functional blocks in the sparse sample processing architecture are shown in Fig. 7.1.

A number of channels produces aligned bit sequences by reading the buffered bit stream from locations determined by the delay generation logic. The corresponding bits from within these sequences are summed. As a result, sequence of multi-bit numbers is produced. The sequence passes through filter block that produces in-phase and quadrature sample.

The sample buffers are implemented using dual-port RAM blocks, in which the write operation is independent of the read operation and both can be performed simultaneously. That feature is available with Xilinx FPGA devices and its presence determined the choice of the target device.

An important feature of the implementation is the parallelizing of the processing logic in four. This is necessary because of the required length of the in-phase and quadrature filters, and the amount of available clock cycles for sample reconstruction. The input sample rate of 140 Mbps per channel does not leave much room for reading the data at higher rate (twice higher at most is possible with the selected FPGA device, and that is the state-of-the-art performance for a contemporary FPGA devices).

Parameter	**Value**
Target sampling rate	140 MHz
Number of channels	32
Length of the matched filter	120 coefficients
Number of lines per image	80

Table 7.1: Parameters for the implementation

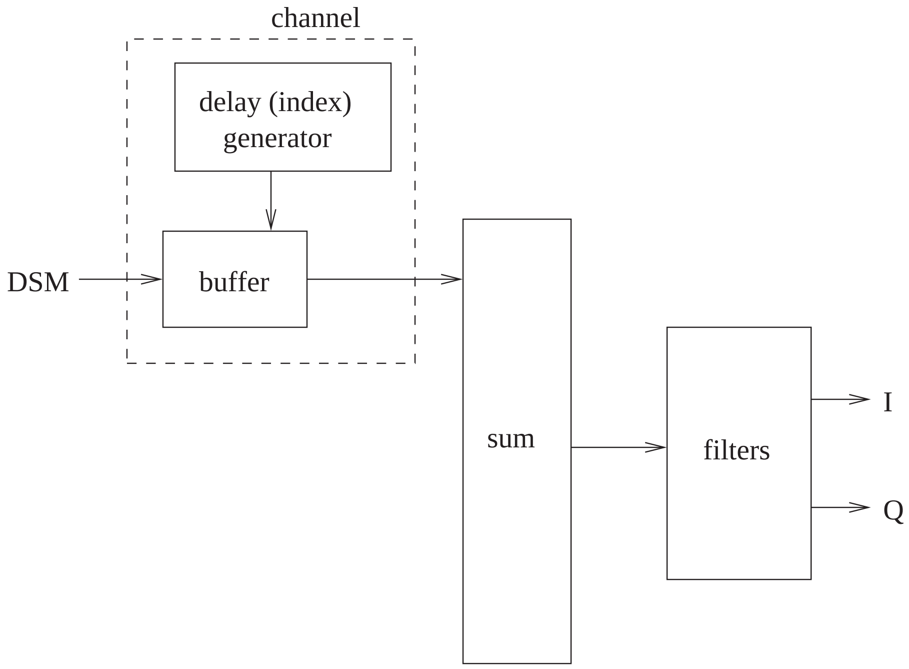

Figure 7.1: Sparse sampling architecture layout

7.1 Sample buffer

In digital ultrasound beamformers, sampling buffers (digital memories, analog cells, CCD cells) are used as temporary storage for the sampled data. They provide the ability to change the delay profile from sample to sample by reading the samples (digital word, current or charge) corresponding to a specific time instant.

For the FPGA implementation of the sparse sample processing beamformer, using Xilinx FPGA device is beneficial in that it incorporates quite a large number of dual-ported memory blocks (Block SelectRAM+^{TM}), which provide simultaneous read and write capability with different word sizes for the read and write operations. For the specific case, the written samples are one-bit wide, while the read data is 4-bit wide.

Since the requested start address for the read operation is specified in one-bit samples, an alignment unit has to be used so that the first output word from the buffer memory contains the samples 1 to 4 starting with the specified address, the second - bits 5 to 8 and so on. Such an alignment unit is created using a set of 7 two-stage latches. The logic of the operation of the sample buffer is shown in Fig. 7.2. The 2 least significant bits of the read address determine in what position the output bus multiplexers will stay during the present sample processing cycle. The rest of the read address bits determine the 4-bit word that will be read. That part of the address is increased by one on each clock cycle. On the first clock cycle after a valid address

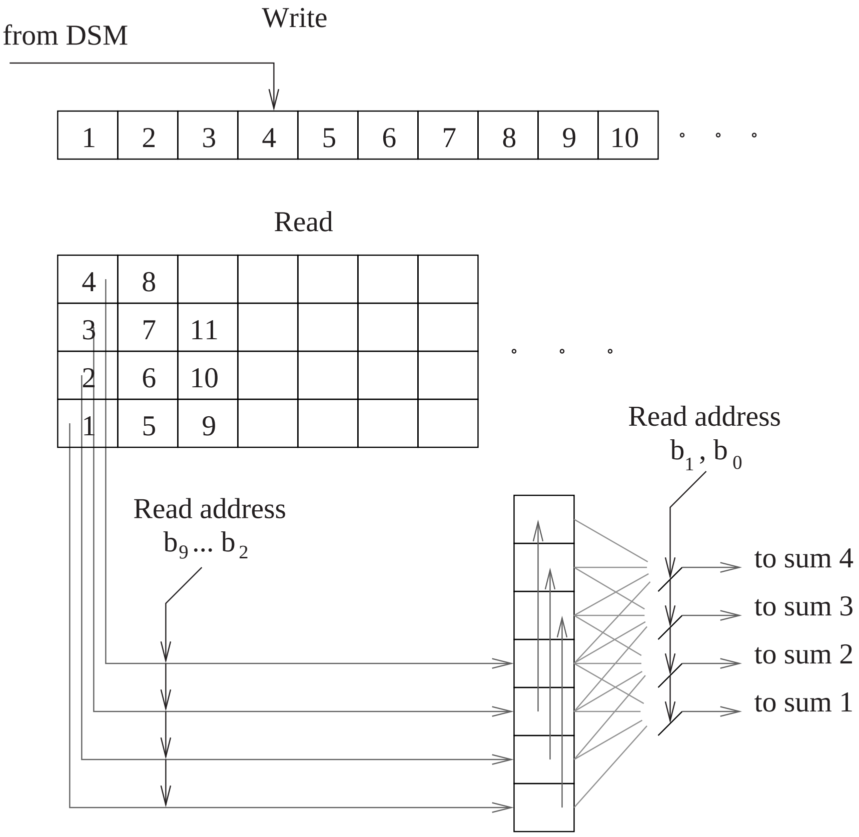
Write
from DSM
1
2
3
4
5
6
7
8
9
10
Read
4
8
3
7
11
2
6
10
1
5
9
Read address
b_1, b_0
Read address
$b_9 \ldots b_2$
to sum 4
to sum 3
to sum 2
to sum 1

Figure 7.2: Writing and reading form the sample buffer

is selected, an initial reading into the alignment register is done. That register produces aligned bit groups starting with the second clock cycle. Therefore, in 33 clock cycles, up to 128 bits can be read.

The amount of logic resources occupied by that module in the FPGA device is 17,775 gates, and its estimated maximum operation clock frequency after taking into account switching delays is 154.799 MHz.

7.2 Delay generation logic

Own delay generation logic was synthesized with the following results: total equivalent gate count for design was 4,453 and maximum operating frequency of 114.534 MHz.

A recursive delay generation algorithm, developed by Feldkämper et al. [30], was adopted. The computation logic consists of 4 registered adders and 1 comparator plus some control circuitry

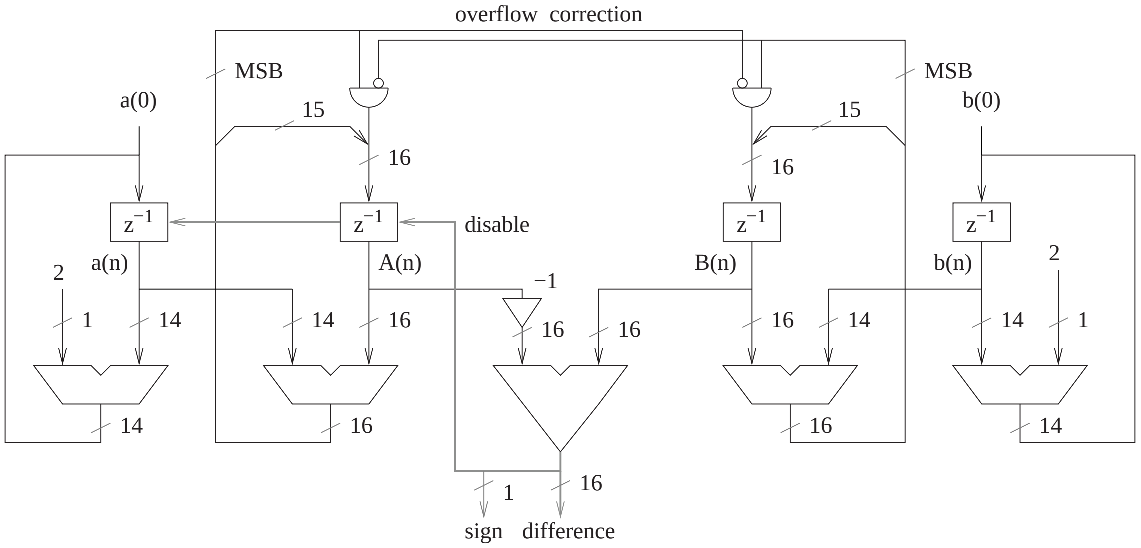

Figure 7.3: Delay generation logic

(Fig. 7.3). The number of parameters per line per channel is 4, thus making it easy to fit the beamformation information for the whole image inside the FPGA memory space.

Using XILINX ready-made and optimized modules, the gate count is 2,251, and the maximum operation frequency is 186.220 MHz.

7.3 Apodization

The apodization (aperture smoothing, tapering) can be applied either on the digital data or on the analog signal before delta-sigma modulation. The channel weighting control consists of a register for the current weighting coefficient of the channel signal and control logic for changing the coefficient with time.

Using the weight coefficient in digital domain means that after the apodization block, the channel data bit-width will be equal to that of the weight coefficient. Thus, the sum operation across the channels is performed on multi-bit numbers instead on 1-bit numbers. For maintaining high operation speed, the adder pipeline depth has to be increased and the latency of the adders increases.

Applying the weight coefficient in the analog domain can be done by varying the feedback voltage of the sigma-delta modulator [38]. The voltage can be generated by pulse-width modulation or by DSM D/A conversion.

The algorithm for generation of the apodization coefficient is not straightforward. Simple linear development of the apodization coefficients throughout the image produces inferior array directivity pattern. Therefore, the linear interpolation should be combined with look-up table so that finer apodization profiles can be achieved. At present, no apodization strategy was preferred and consequently, no apodization was implemented in VHDL.

7.4 Summing block

The sum operation across all channels is pipelined in order to incorporate numerous inputs and to process them at high clock frequency. The first stage in the pipeline contains 4-input look-up tables, each producing the sum of the incoming 1-bit words from 4 channels. The resulting 8 3-bit numbers are summed in pairs in the second pipeline stage into 4 4-bit numbers. The third summation stage produces 2 5-bit numbers and the 4th stage produces one 6-bit number that is fed into the matched filter. The summation stage has latency of 3 clock cycles and can operates at very high frequency.

The equivalent gate count for the summing block is 1,083 and it can operate at clock frequency up to 271.592MHz.

7.5 Filters for in-phase and quadrature component

The length of the filters is constrained by the amount of clock cycles that are available for producing a reconstructed sample. That number is inversely proportional to the density of the beamformed samples, and its maximum value for a given imaging setup can an be calculated as

$$N_r c = \left\lfloor \frac{2 * f_s * d_{max}}{N_s c} \right\rfloor, \tag{7.1}$$

where d_{max} is the image depth, N_s is the number of reconstructed samples, and c is the speed of sound. The minimum available number of clock cycles is the distance between the first two read operations offsets.

For instance, if 512 points should represent a depth range of 0.15 m, there are 33 cycles available to the filter block for producing in-phase and the quadrature reconstructed samples. In the current design, the filtering operation is parallelized in four, so in-phase and quadrature filters with length up to 128 can be used (32 clock cycles are usable and one is lost due to latency). A perfect matched filter for the simulation setup has length of 168. Therefore, a pseudo-matched filter with 120 coefficients was used in the implementation.

The total equivalent gate count for design is 31,720. The multipliers are pipelined, with latency of 3 clock cycles. The adders are registered, with latency of 1 clock cycle. The maximum operation frequency is 150.489 MHz

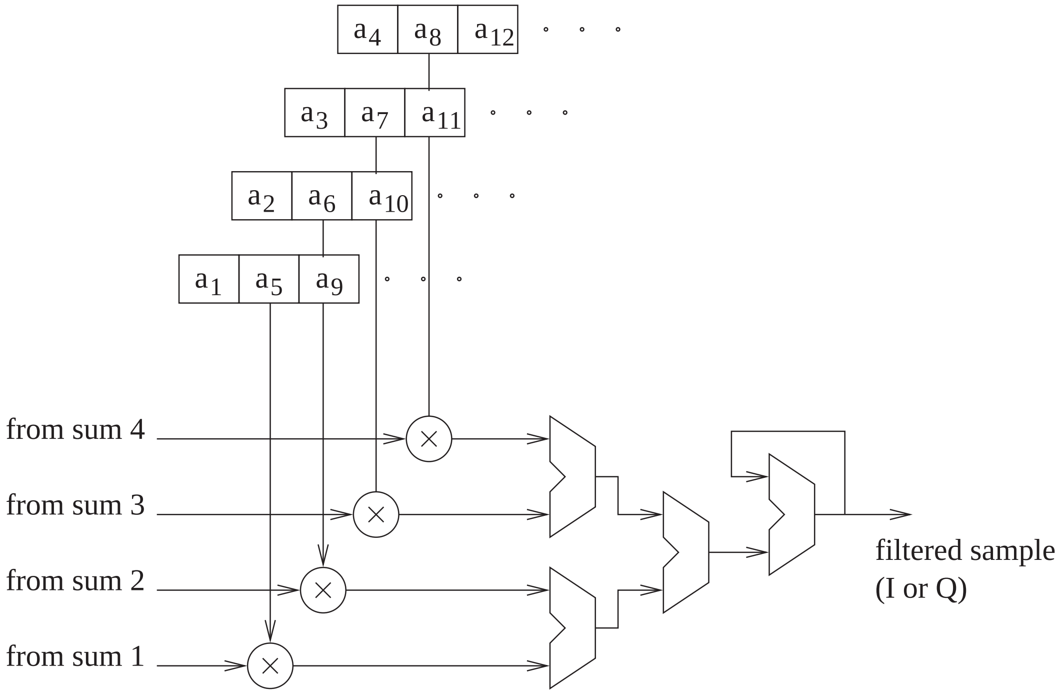

Figure 7.4: Filter block with 4 parallel data paths

7.6 Interface

As an initial interface to the beamformer, a PC parallel port compatible interface was developed. Operated under Windows 2000, the achieved throughput is 40 KB/s. The low throughput is due to the used parallel port access library.

With 512 in-phase and quadrature signal components per image line, for an image depth of 15 cm and speed of sound 1540 m/s, the necessary transfer speed to the PC is

$$M = \frac{512}{\frac{2\dot{0}.15}{1540}} \approx 2.63 MSPS \tag{7.2}$$

The samples are 12-bit, therefore the above rate corresponds to $\approx$ 31.6 Mbps.

That data rate is easily achievable by IEEE-1394 (FireWire, 400 Mbps theoretical) and USB-2 (480 Mbps theoretical) interfaces. For utilizing USB (12 Mbps theoretical) of PC parallel port (up to 12 Mbps), the data rate (and the pulse repetition frequency) has to be decreased about three times.

Parameter	**Value**	**Pct of the total**
Number of Slices	8,487	44
Number of Slice Flip Flops	10,835	28
Total Number 4 input LUTs	14,315	37
Number of bonded IOBs	46	11
Number of Block RAMs	64	40

Table 7.2: Resource utilization results

7.7 Synthesis results for a 32-channel beamformer

After technology mapping, the estimated gate count for the 32-channel beamformer is 1 248 209.

The estimated maximum operation frequency for the design is 144.2 MHz. That estimate takes into account only the logic switching delays. The estimated operation frequency after place and route was 71.6 MHz. In this estimate, the signal routing delays are incorporated. The large difference in the operation frequency estimates shows that the size of the design has a negative influence on the achievable performance, unless manual placing with respect to minimizing the longest paths is used. Another approach is pipelining, but it also requires manual placement of the inserted registers in suitable locations so that the length of the signal paths decreases significantly.

The power consumption for clock frequency of 140 MHz is 1.4 W.

For completeness, the Xilinx Foundations reported resource usage is given in Table 7.2.

CHAPTER EIGHT

Conclusion

The purpose of this Ph.D. project was to investigate approaches for achieving compact beamformation. There exists a multitude of hardware platforms on which compact beamformation can be pursued. Several successful examples will be mentioned:

- Charge Domain Processing [43] - manipulating electrical charge.
- Switched current delay lines [44] - using switched current memory elements.
- Analog FIFO, consisting of Sample-and-Hold elements [45].

That list demonstrates the interest of the research society in the area of compact and inexpensive medical imaging. The present work concentrated on oversampled converters, which are suitable for CMOS implementation.

One of the contributions of this thesis is the general recursive delay generator. For the particular case of focusing delays, it appeared to be second to the LUCS delay generator, but the approach may find other applications, given its ability to generate precise delays from the moment of transmission. Another contribution is the new oversampled beamformer architecture, which performs precise sample reconstruction. Its evaluation shows that it is capable of producing high-quality B-mode images and flow estimates.

Future work will include applying the oversampled beamforming for synthetic aperture imaging and building a prototype imaging device based on the suggested beamformer.

APPENDIX

A

A new architecture for a single-chip multi-channel beamformer based on a standard FPGA

Authors : Borislav Gueorguiev Tomov and Jørgen Arendt Jensen

Presented : Paper presented at the IEEE Ultrasonics Symposium, 2001, Atlanta, USA. Published in the Proceedings of the Ultarsonics Symposium, 2002.

Abstract

A new architecture for a compact medical ultrasound beamformer has been developed. Combination of novel and known principles has been utilized, leading to low processing power requirements and simple analog circuitry. Usage of a field programmable gate array (FPGA) for the digital signal processing provides programming flexibility.

First, sparse sample processing is performed by generating the in-phase and quadrature beamformed signals. Hereby only 512 samples are beamformed for each line in an image. That leads to a 15-fold decrease in the number of operations and enables the use of Delta-Sigma ($\Delta\Sigma$) modulation analog-to-digital converters (ADC).

Second, simple second-order $\Delta\Sigma$ modulation ADC with classic topology is used. This allows for simple analog circuitry and a very compact design. Several tens of these together with the corresponding preamplifiers can be fitted together onto a single analog integrated circuit.

Third, parameter driven delay generation is used, using 3 input parameters per line per channel for either linear array imaging or phased array imaging. The delays are generated on the fly. The delay generation logic also determines the digital apodization by using 2 additional parameters. The control logic consists of few adders and counters and requires very limited resources.

Fourth, the beamformer is fully programmable. Any channel can be set to use an arbitrary delay curve, and any number of these channels can be used together in an extendable modular multi-channel system.

A prototype of the digital logic is implemented using a Xilinx Virtex-E series FPGA. A 5 MHz center frequency is used along with an oversampling ratio of 14. The sampling clock frequency used is 140 MHz and the number of channels in a single Xilinx 1 million gate FPGA XCV600E is 32. The beamformer utilizes all of the BlockRAM of the device and 33 % of its Core Logic Block (CLB) resources.

Both simulation results and processed echo data form a phantom are presented.

1 Introduction

Making sophisticated technology more accessible is an important consideration in system design. Since digital electronics is rapidly evolving, moving processing functions from analog to digital electronics is a powerful approach which allows for increased flexibility and compactness of the mixed-signal devices.

ΔΣ modulation (DSM) [33] is one of the techniques that make it possible to decrease the complexity of the analog interface electronics by using digital logic. A DSM ADC consists of consecutive stages containing low-pass filters and decimators. The reconstructed samples represent the input signal at equidistant time instances. Ultrasound beamformers though require non-regular sampling because of the delay profiles in receive. A number of researchers have tried to incorporate DSM ADCs into ultrasound beamformers. Freeman et al. [39] have developed a modified modulator architecture in order to facilitate the delay profiles in the beamforming without interrupting the modulation process. Since the oversampling ratio (OSR) is crucial for the amplitude resolution of a DSM ADC, the same research group suggested base-band demodulation [46]. Kozak and Karaman [40] have proposed a beamformer featuring DSM with a non-uniform sampling clock.

In the present paper, several novel techniques are combined in a new beamformer architecture. First, sparse sample processing is employed, leading to about 15-fold decrease in the necessary operations as only 512 samples per image line are processed. The samples are chosen at the precise time instances, discretized by the sampling frequency of the DSM. Second, each channel uses a circular buffer at the output of the DSM for extraction of the necessary data. Thus, the structure does not impose any restrictions or requirements on the order or topology of the DSM, allowing for flexibility and interchangeability of the analog front-end. Third, the delay generation is parametric and allows independent on-the-fly delay generation for each channel. The calculation scheme is inspired by the Bresenham drawing algorithm [32].

2 Principles behind the suggested beamformer architecture

2.1 Rationale for the sparse sample processing

The ultrasound images are displayed on raster devices - CRT or LCD displays, which rarely use a resolution beyond that of a TV (525 lines for NTSC) or VGA (640x480 pixels). Therefore, on such displays a beamformed line in an image is represented by no more than 512 points. Thus, it is sufficient to have the correct envelope and phase of the RF signal in 512 equidistant points along the beamformed line to present a correct B-mode or color-flow image. A similar approach was proposed in a different context by Karaman et al. [41].

2.2 Usage of the Delta-Sigma modulator in the beamformer

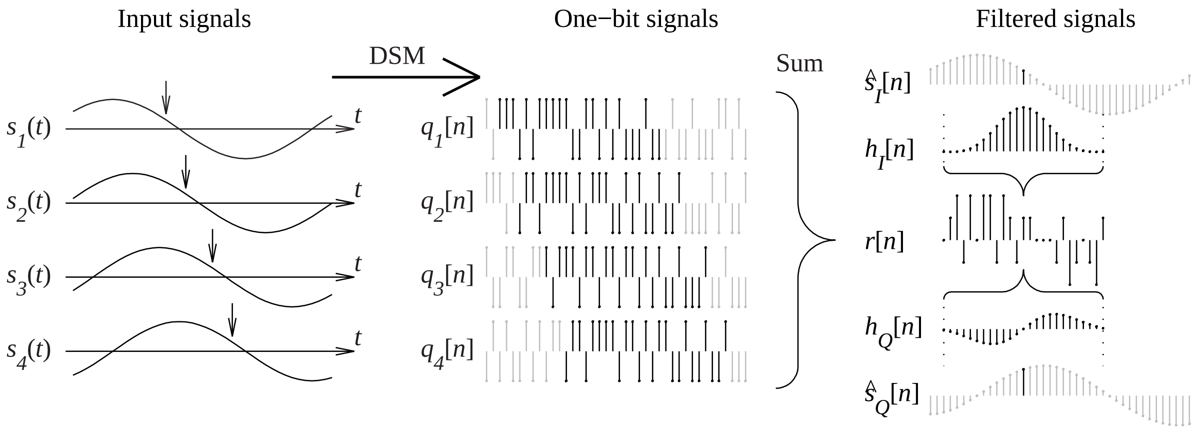

Figure A.1: Signal processing of the proposed beamformer, illustrated with 4 channels

The principle of the DSM implies that the appropriately filtered output of a DSM approximates the input signal, and the approximation improves with increasing the oversampling ratio (OSR). If a filter is applied directly on the DSM output stream, valid output samples can be reconstructed at any clock cycle. In this way, the delay resolution in a beamforming process will be equal to the period of the inherently high modulation frequency.

The signal processing is illustrated in Fig. A.1. The analog input signals $s_k(t)$ (k is channel index) from different channels are modulated into bit streams $q_k[n]$ in the DSM. In order to perform beamforming at a given point indicated by arrows in the plots of $s_k(t)$, sequences of bits (shown in black) are extracted from the streams $q_k[n]$, at places that correspond to the appropriate channel delays. The length of the sequences is equal to the length of the reconstruction filters that will be used. The selected sequences are summed into sequence $r[n]$. The latter is then weighted by in-phase $h_I[n]$ and quadrature $h_Q[n]$ filters to yield selected samples of the in-phase $\hat{s}_I[n]$ and quadrature $\hat{s}_Q[n]$ reconstructed streams. The matched filter from the classic beamforming is used as in-phase filter and its Hilbert transform is used the quadrature filter, since they suppress the quantization noise to a sufficient degree.

2.3 Delay generation

A delay calculation scheme is suggested that allows on-the-fly delay generation. It approximates the analytic delay curve for a given imaged line and receiver element. A similar approach with different calculation scheme has been suggested by Feldkämper et al. [30] for increasing the delay resolution in beamformers.

The geometry behind the delay calculation algorithm is shown in Fig. A.2. The distance to the focus point P along the scan line is denoted d and the echo path is denoted d_r. The full path of the ultrasound wave is denoted p. The aperture distance between the emission center and the receiving element is denoted with x and the angle between the scan line and the normal to the transducer surface is denoted φ.

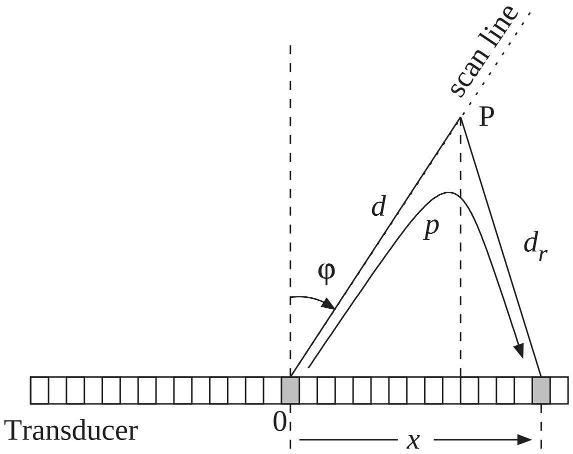

Figure A.2: Delay calculation geometry

The echo path d_r can be expressed as:

$$d_r = p - d = \sqrt{(x - d\sin\varphi)^2 + (d\cos\varphi)^2}. \tag{A.1}$$

After some transformations the equation

$$p^2 - 2d(p - x\sin\varphi) - x^2 = 0 \tag{A.2}$$

is obtained, which describes the imaged line. The term $x\sin\varphi$ is constant for a given line inclination and element and is denoted k. For converting the variables into units of clock cycles (for calculations in hardware), both sides of (A.2) have to be multiplied by $(\frac{f_s}{c})^2$, where f_s is the sampling frequency and c is the speed of sound. Eq. (A.2) becomes:

$$f(p_N, d_N) \equiv p_N^2 - 2d_N(p_N - k_N) - x_N^2 = 0, \tag{A.3}$$

where the index N denotes that the variable unit is clock cycle.

In order to keep the focus on the imaged line, the delay generation logic has to keep $f(p_N, d_N)$ as close to 0 as possible, therefore it should increase p_N by 1 or 2 for each unit increase of d_N. The choice[1] is made by evaluating the sign of the function $f(p_N + 1, d_N + 1)$. It can be seen that:

$$f(p_N + 1, d_N + 1) = f(p_N, d_N) - 2d_N + 2k_N - 1 < f(p_N, d_N) \tag{A.4}$$

and

$$f(p_N + 2, d_N + 1) = f(p_N, d_N) + 2p_N - 4d_N + 2k_N > f(p_N, d_N). \tag{A.5}$$

Therefore the following algorithm is suggested:

1. The initial values $d_N(1) = d_{start}\frac{f_s}{c}$, $p_N(1) = p_{start}\frac{f_s}{c}$, and $k_N = x \sin\varphi \frac{f_s}{c}$ are supplied.

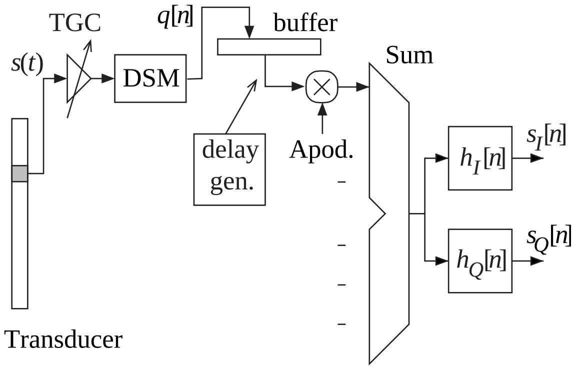

Figure A.3: Beamformer architecture

2. If $f(p_N + 1, d_N + 1) > 0$, then $p_N(n+1) = p_N(n) + 1$, else $p_N(n+1) = p_N(n) + 2$.
3. If the end of the line is not reached, go to 2.

The described algorithm approximates the analytical dynamic delay curve within ±1 clock cycle.

---

[1] In case of tilted line, p_N could also stay unchanged at some increase of d_N. The decision requires evaluation of the sign of $f(p_N, d_N + 1)$.

3 Beamformer architecture

The suggested beamformer architecture is shown in Fig. A.3. The received RF signal $s(t)$ from every active transducer element is amplified by a variable-gain amplifier (used for time-gain compensation) and is converted into high-frequency 1-bit digital signal $q[n]$ in the DSM. That data stream is written to a circular buffer. At time instances determined by the delay generation logic, sequences from the stream are read. After multiplication by the apodization coefficient (the weight) of that channel, the aligned sequences corresponding to a given line point are summed across all channels. The result is then filtered for extracting the in-phase and the quadrature components $\hat{s}_I[n]$ and $\hat{s}_Q[n]$.

4 Implementation tradeoffs and choices

The described architecture was implemented in hardware with the following beamformer parameters:

Parameter	**Value**
Speed of sound	1540 $\frac{m}{s}$
Center frequency f_0	5 MHz
Excitation	2 sinusoids at f_0
Oversampling ratio (OSR)	14
Number of channels	32

An important design decision is the choice of the in-phase and the quadrature filters. The matched filter from classic beamforming (time reversed excitation convolved twice with the impulse response of the transducer) provides excellent suppression of the quantization noise. The length of the filters though is constrained by the amount of clock cycles that are available for producing a reconstructed sample. That number is inversely proportional to the density of the beamformed points. For instance, if 512 points should represent a depth range of 0.15 m, there are between 26 and 53 clock cycles available to the filter block for producing in-phase and the quadrature reconstructed samples.

In the current design, the filtering operation is parallelized in four, so in-phase and quadrature filters with length up to 104 can be used. A perfect matched filter for the simulation setup has length of 168. Therefore, a number of pseudo-matched filters were investigated. The frequency response of the perfect matched filter and that of a shortened one (3 central frequency sinusoids, Hamming window weighted) is shown in Fig. A.4.

The point spread functions (PSF) of single scaterers in the transmit focal point were obtained through simulations using the two mentioned filters. They were compared against the reference beamforming PSF (Fig. A.5) .

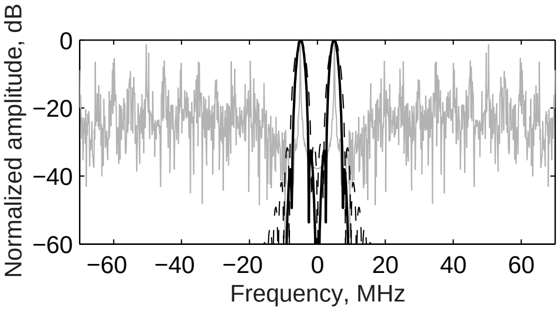

Figure A.4: Frequency response of perfect matched filter (solid line) a shortened one (dashed line), along with typical DSM output spectrum (gray).

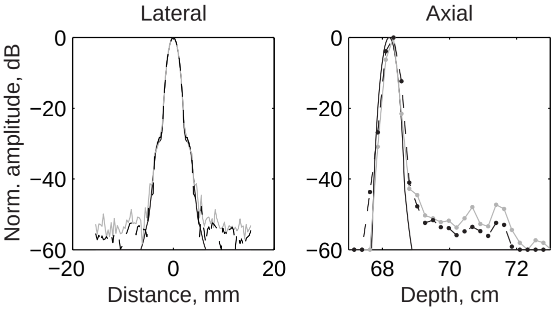

Figure A.5: Simulated PSF: classic beamforming (solid line), ideal matched filter (dashed line), shortened filter (grey line).

The implementation target is the Xilinx Virtex-E FPGA device family which features quite a high number of dual-ported fast SRAM that can be used as buffers for the DSM output stream. A number of specific design choices are made:

1. The output word of the delay buffer is wider than the input one. This speeds up the reading and allows for parallel processing of the data at the highest possible clock rate.
2. Each calculation cycle in the delay generation requires two clock cycles, therefore a more aggressive computational scheme is employed: d_N is increased by 2 for each computation cycle and the sign of $f(d+2,p+1)$, $f(d+2,p+2)$ and $f(d+2,p+3)$ determines whether p_N should be increased by 1, 2, 3, or 4.
3. The output data from the DSM is a 1-bit wide in the current implementation and the apodization does not require multiplications. It uses one register instead.
4. The sum operation across all channels is pipelined in order to incorporate numerous inputs and to process them at high clock frequency. The multiplication operation is

pipelined also and works at the modulation clock frequency.

5. A chain of beamformers can be used, each of them receiving partially beamformed sample from a neighbor, summing it with its own partially beamformed sample, and passing it further on.

5 Phantom data processing results

A set of element traces sampled at 40 MHz was obtained using the experimental sampling system RASMUS [17]. That data was resampled at 140 MHz and 200 MHz, and was beamformed according to the suggested architecture. A comparison between the beamforming approaches is shown in Fig. A.6. The element number is 32 and the F-number is between 2.5 and 10. It can be seen that the quantization noise of the DSM limits the picture contrast and increasing the OSR improves that. Improvement can also be achieved by employing a more sophisticated modulator architecture.

6 Conclusion

A novel flexible beamformer architecture utilizing DSM is suggested. The beamformer can be housed in one standard FPGA, which can easily be programmed and upgraded. Combined with a simple analog front end, the whole design can be implemented by three chips (one of them containing the transmit amplifiers). A standard portable PC can be used for display, making it a very inexpensive system.

Acknowledgment

This work was supported by grant 9700883 and 9700563 from the Danish Science Foundation, by B-K Medical A/S, Gentofte, Denmark, by the Thomas B. Thrige Center for Microinstruments, and by the Danish Research Academy.

The authors would like to thank all colleagues at the Center for Fast Ultrasound Imaging for their cooperation and valuable comments on the paper.

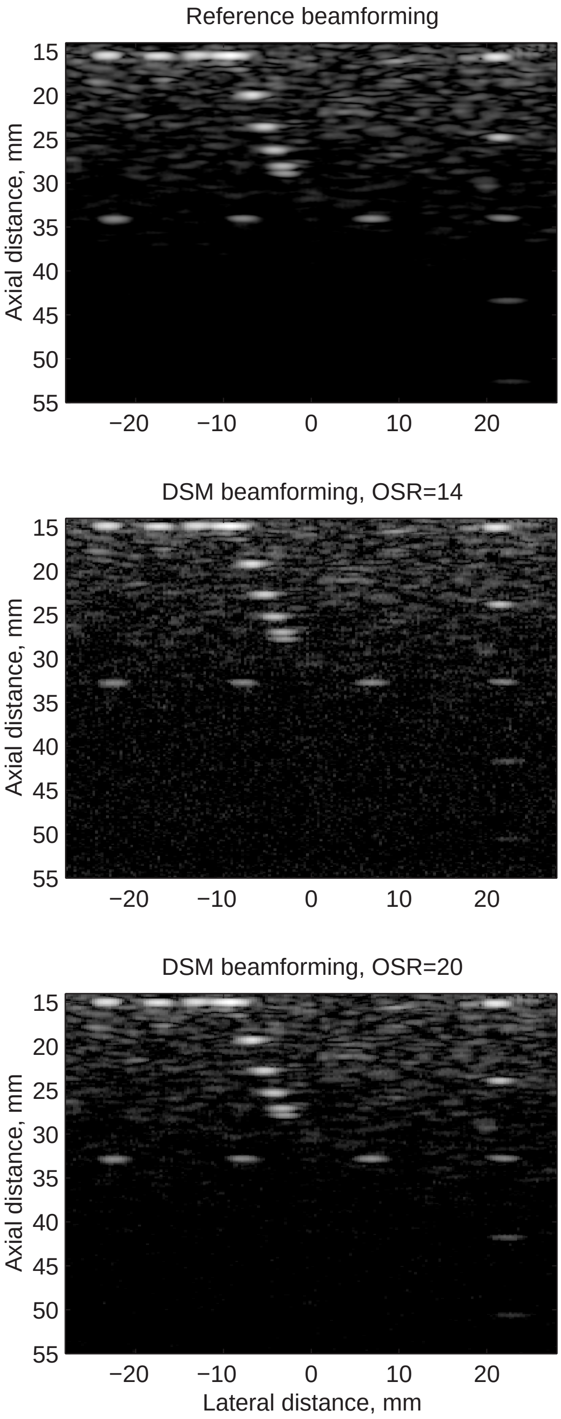
Reference beamforming
DSM beamforming, OSR=14
DSM beamforming, OSR=20
Axial distance, mm
15
20
25
30
35
40
45
50
55
−20
−10
0
10
20
Lateral distance, mm

Figure A.6: Images created with classic beamforming and with the suggested beamforming at different OSR. The dynamic range is 40 dB

APPENDIX

B

Delay generation methods with reduced memory requirements

Authors : Borislav Gueorguiev Tomov and Jørgen Arendt Jensen

Presented : Paper accepted for presentation at SPIE Conference on Medical Imaging, 2003, San Diego, USA

Abstract

Modern diagnostic ultrasound beamformers require delay information for each sample along the image lines. In order to avoid storing large amounts of focusing data, delay generation techniques have to be used. In connection with developing a compact beamformer architecture, recursive algorithms were investigated. These included an original design and a technique developed by another research group. A piecewise-linear approximation approach was also investigated. Two imaging setups were targeted - conventional beamforming with a sampling frequency of 40 MHz and subsample precision of 2 bits, and an oversampled beamformer that performs a sparse sample processing by reconstructing the in-phase and quadrature components of the echo signal for 512 focal points. The algorithms were synthesized for a FPGA device XCV2000E-7, for a phased array image with a depth of 15 cm. Their performance was as follows: 1) For the best parametric approach, the gate count was 2095, the maximum operation speed was 131.9 MHz, the power consumption at 40 MHz was 10.6 mW, and it requires 4 12-bit words for each image line and channel. 2) For the piecewise-linear approximation, the corresponding numbers are 1125 gates, 184.9 MHz, 7.8 mW, and 15 16-bit words.

Introduction

In medical ultrasound, the vast majority of the diagnostic images are produced line by line. A number of receive channels perform focusing along the image lines as the transmitted wave propagates in depth. The process is called beamforming. For the purpose of maintaining focus as the depth increases, the delay applied to the echo signal samples on different channels has to change [14]. In digital beamformers, variable length delay lines can be easily implemented by using memory elements. The use of digital memory allows a new focal depth to be targeted for each sample produced by the beamformer. The amount of necessary focusing information is large, since delay information for all receive channels for all focusing depths has to be stored. Keeping it in an uncompressed form requires a lot of memory, and researchers have been working on approaches for compression since the introduction of the digital beamformation. With the advances in digital IC fabrication, the algorithms grew in complexity. The compression techniques utilize the nature of the focusing delay curves. Among the first to investigate compression of focusing data were Peterson and Kino [10]. They suggested delta encoding - storing only the differences between the delay (index) values. Among the first to suggest a parametric approach for delay calculation were Jeon et al. [29], who applied this technique to sampling clock generation. Recently, Feldkämper at al [30], while working on the LUCS (Low-power Ultrasound Chip Set) project, developed an efficient delay computation scheme along the same principle, offering a very compact implementation. This method will be discussed further in this paper, and will be referred to as the ”LUCS delay generator”.

During the development of a new oversampled beamformer architecture [31], a general parametric delay generation algorithm was developed, capable of providing a geometrically valid delay value for all channels from the moment of transmission. Due to the need of operation at a high frequency, piecewise-linear approximation of the delay curve was also investigated. This paper presents the approaches considered and the implementation results for each of them.

Section 2 demonstrates by an example the need for compressing the focusing data. Section 3 shows the delay generation geometry and the equations that can be derived from it. In Section 4, the general parametric approach is presented. The LUCS delay generator is presented in Section 5. The piecewise-linear approximation of the delay curve is discussed in Section 6 and implementation results are given in Section 7. Section 8 contains a discussion on the suitability of the approaches for different beamformer types.

1 Memory requirements in ultrasound beamforming

A digital beamformer, that performs dynamic receive focusing, requires a new delay value on each clock cycle and for every channel involved in the beamformation. For an image line with a length $d_l = 15$ cm, sampled at a frequency $f_s = 40$ MHz and for speed of sound $c = 1540$

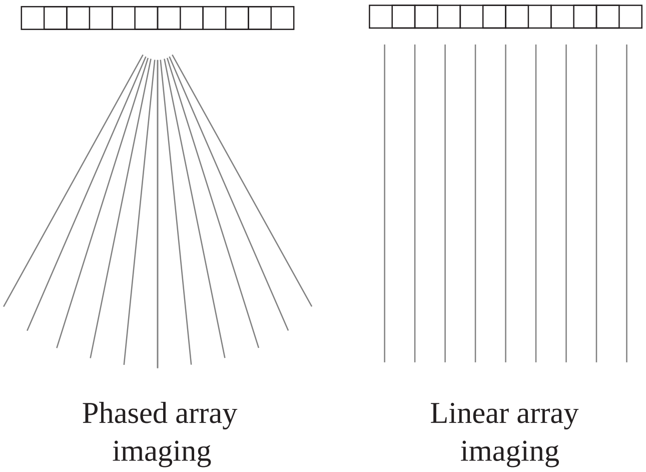

Figure B.1: Image line positions in different imaging techniques.

ms^{-1}, the number of the delay values is

$$N_l = \frac{2d_l f_s}{c} = 7792. \tag{B.1}$$

That number, multiplied by the number of channels n, will yield the necessary storage size for the beamformation of one image line. For calculating the necessary storage for a whole image, multiplication by the number of lines m has to be done. For a modest ultrasound imaging system with 64 channels, the number of delay values per frame consisting of 80 lines is

$$N_f = mn\frac{2d_l f_s}{c} \approx 40 \times 10^6. \tag{B.2}$$

Depending on the way the image lines are generated in an ultrasound image, different options for reducing the amount of necessary memory exist:

- In phased array imaging, the symmetry in the beamforming can be exploited so that the number of values is halved (see Fig. B.1).
- In linear array imaging, with linear or convex transducer, the delay information is the same from line to line, and the channels connect to a different transducer element on every emission. Also, there is symmetry in the delay profiles, which allows the focusing data to be halved. In that case, the necessary number of delay values for a 64-channel system is

$$N_f = m\frac{2d_l f_s}{2c} = 249 \times 10^3. \tag{B.3}$$

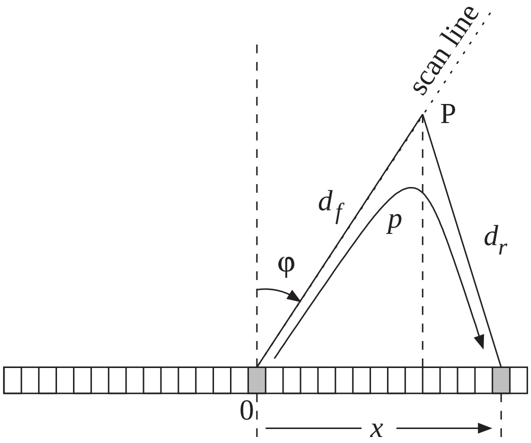

Figure B.2: Delay calculation geometry

In both cases, the necessary storage could hardly fit together with the focusing logic into a single-chip beamformer. Compression of the focusing information can reduce the memory requirements. A conventional, transportable imaging system also benefits from reducing the amount of integrated circuits it uses.

2 Index generation geometry

The images produced by contemporary ultrasound scanners consist of straight lines originating from the transducer surface. The geometry for the calculation of the time of flight of the ultrasound wave is shown in Fig. B.2.

The distance from the beam origin to a focal point P along the scan line is denoted d_f and the echo path is denoted d_r. The full path of the ultrasound wave is denoted $p \equiv d_f + d_r$. The distance between the beam origin center and the receiving element is denoted with x and the angle between the scan line and the normal to the transducer surface is denoted φ.

The echo path d_r can be expressed as:

$$\begin{aligned} d_r = p - d_f &= \sqrt{(x - d_f \sin\varphi)^2 + (d_f \cos\varphi)^2} \\ &= \sqrt{x^2 - 2d_f \sin\varphi + d_f^2}. \end{aligned} \tag{B.4}$$

The pulse-echo path p is calculated as

$$p = d_f + d_r = d_f + \sqrt{x^2 - 2d_f \sin\varphi + d_f^2}. \tag{B.5}$$

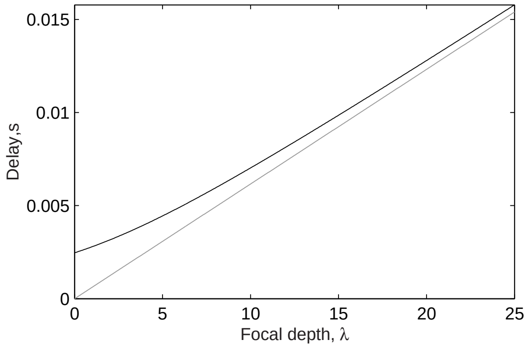

Figure B.3: Delay profiles for center element (gray) and an element (black) situated at 8 λ away from the center element.

The times of flight for a transducer element at the beam origin and for another element that is situated at a distance of 8λ away from it are shown for depths up to 25λ and non-tilted beam in Fig. B.3. It illustrates the nature of the delay profiles in beamforming. As the wave propagates in depth, the difference between the times of flight for different receiving elements decreases. Here $\lambda = \frac{c}{f_0}$, where c is the speed of sound and f_0 is the central frequency of the transmitted wave. For best imaging performance, it is usually selected to coincide with the peak of the frequency response of the transducer elements.

In this paper, independent beamformer channels are considered and beamformation can be viewed as selecting the correct sample for a given focus depth from different channels. Therefore, the beamformation will be described by sample indexes and not by relative delays between channels.

3 General parametric approach

A pioneer in the numeric control, Bresenham suggested algorithms for fast drawing of lines, circles and ellipses on raster devices [32]. According to his approach, the describing equation of the curve is rewritten as a function of point coordinates. When the value of the function is zero, the point with the current coordinates lays on the curve. When the value is positive or negative, the point is either above or below (on the left or on the right side of) the curve. The sign/space relation depends on the chosen leading coordinate and the way the curve equation is rewritten. The leading coordinate is the one that is supposed to increase by one at each calculation (and drawing) step. During drawing of circles and ellipses, the leading coordinate changes (from x to y) at the places where the slope of the curve crosses $\frac{\pi}{4}$.

Bresenham's approach can be generalized for use with any kind of curve that is described by a quadratic function. Due to the fact that the delay curve can be described by an equation, a delay generation algorithm can be built around that equation by numerically solving it at each step of increase of a leading variable (in this case - time). The resulting implementations require a few input parameters, but have the disadvantage of dissipating power in calculations. This section presents a general algorithm for approximating the ideal delay curve, developed for use in a compact beamformer.

3.1 Transformation to clock periods (clock cycles)

After some transformations, (B.5) turns into

$$p^2 - 2d(p - x\sin\varphi) - x^2 = 0. \tag{B.6}$$

This is the equation of the delay curve. The term $x\sin\varphi = k$ is constant for a given line inclination and element.

The aim of the delay generation approach is for every output sample to produce delays (sample indexes, RAM addresses) that for each channel are pointing to the appropriate sample, necessary for the focusing of the output sample. For this purpose, the algorithm is expected to generate delays at a rate of one value per output sample. The leading variable in (B.6) is the instant focal depth d, which changes by $\Delta = cT_s/2$ with each clock cycle. Dividing both sides of (B.6) by the squared distance Δ^2 converts the computation unit into clock cycles:

$$f(p_N, d_N) \equiv p_N^2 - 2d_N(p_N - k_N) - x_N^2 = 0. \tag{B.7}$$

The index N denotes that the variable unit is quantized and is an integer.

3.2 Influence of the directivity properties of the transducer elements

Generating delay values for every beamformer channel from the moment of the transmission is not necessary because of the directivity properties of the transducer elements. Immediately after transmission, only a few transducer elements receive a useful echo signal. Also the reflection from the scaterers is strongest in the direction from where the wavefront has come, and is weaker to the sides. An illustration of an imaging situation is given in Fig. B.4.

These limitations are of major importance, since they cause the most curved section of the delay curve to be effectively omitted, and thus relieve the requirements toward the delay generation algorithms. In the following, the influence of the directivity properties of the transducer elements is considered.

One additional parameter has to be provided for each channel: delay to start of use. The setup for calculating that parameter is shown in Fig. B.5. The distance d_0 along the image line from which an element i should start taking part into the beamforming can be derived using the Sinus

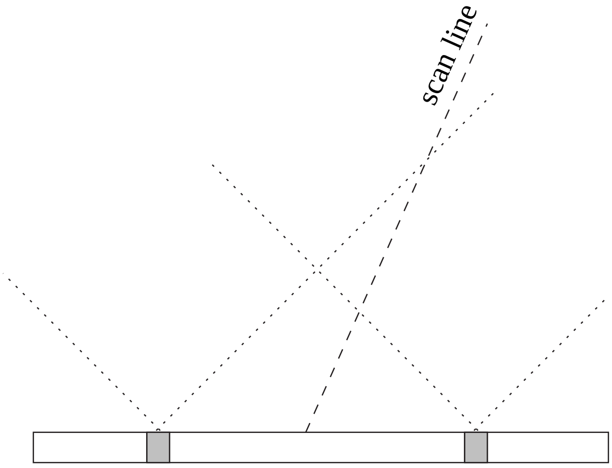

Figure B.4: Limitations to the element contribution to the beamforming.

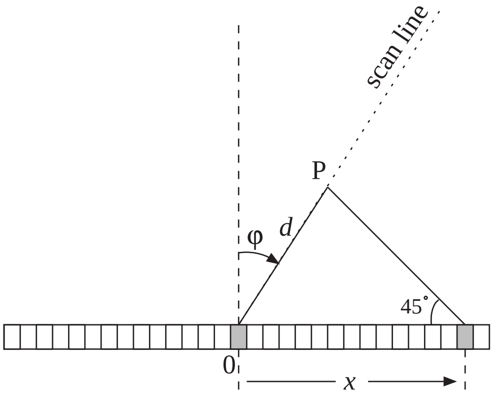

Figure B.5: Setup for calculating the delay after which a channel can contribute to the beamforming of a given image line.

theorem for a triangle as

$$d_{0,i} = \frac{x_i}{\sqrt{2}\sin(\frac{3\pi}{4} - \varphi)}, \tag{B.8}$$

where x_i is the distance between the transducer element and the origin of the transmitted beam. According to this relation, the receive aperture is not symmetrical when the image line is tilted.

Taking that limitation into account when designing a beamformer leads to relaxed requirements on the length of the delay lines.

3.3 Delay generation algorithm

In the suggested algorithm, the function to be evaluated is $f(p_N, d_N)$. To approximate the delay curve, the delay generation logic has to keep $f(p_N, d_N)$ as close to 0 as possible, therefore it should increase p_N by 1 or 2 for each unit increase of d_N. The choice is made by evaluating the sign of the function $f(p_N+1, d_N+1)$. It can be seen that:

$$f(p_N+1, d_N+1) = f(p_N, d_N) - 2d_N + 2k_N - 1 < f(p_N, d_N) \tag{B.9}$$

and

$$f(p_N+2, d_N+1) = f(p_N, d_N) + 2p_N - 4d_N + 2k_N > f(p_N, d_N). \tag{B.10}$$

Therefore the following algorithm is suggested:

1. The initial values $d_N(1) = d_{start}\frac{f_s}{c}$, $p_N(1) = p_{start}\frac{f_s}{c}$, and $k_N = x\sin\varphi\frac{f_s}{c}$ are supplied.
2. If $f(p_N+1, d_N+1) > 0$, then $p_N(n+1) = p_N(n)+1$, else $p_N(n+1) = p_N(n)+2$.
3. $d_N(n+1) = d_N(n)+1$. If the end of the line is not reached, go to 2.

The described algorithm generates output with a maximum error of ±1 units. Since these units correspond to the distance that the waveform travels in half a clock period, the precision is therefore $\pm 1/2$ clock periods.

4 LUCS delay generator

This approach is based on a different use of the delay geometry. It is shown in Fig.B.6.The distance to the focal point is expressed as $r(t) = tc/2$ and the time-of-flight difference between the transducer element at the beam origin and another element is calculated as:

$$l(t) = \sqrt{r^2(t) + 2r(t)x\sin\varphi + x^2} - r(t). \tag{B.11}$$

The focal depth changes by $\Delta = cT_s/2$. Eq. (B.11) is squared and scaled with the distance Δ . It becomes:

$$\underbrace{n^2 + 2nk(n) + k^2(n)}_{A(n)} = \underbrace{n^2 + n\alpha + \beta}_{B(n)}, \tag{B.12}$$

where $n = r(nT_s)/\Delta$ is the clock period number, $k(n) = l(nT_s)/\Delta$ is the quantized value for the time-of-flight difference, and $\alpha = 2x\sin\varphi/\Delta$ and $\beta = x^2/\Delta^2$ are precalculated constants, specific for each scan line. The expressions $A(n)$ and $B(n)$ are calculated iteratively:

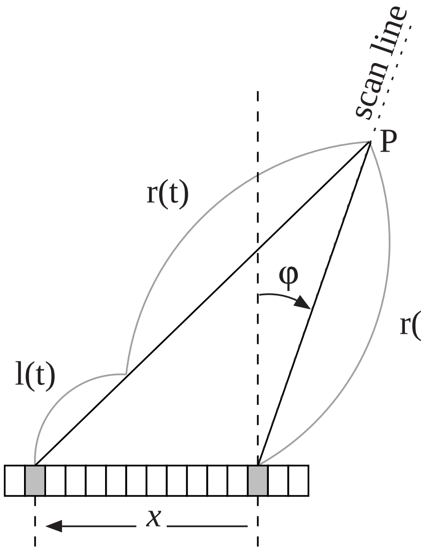
scan line
P
r(t)
φ
r(t)
l(t)
x

Figure B.6: Delay generation geometry for the LUCS generator.

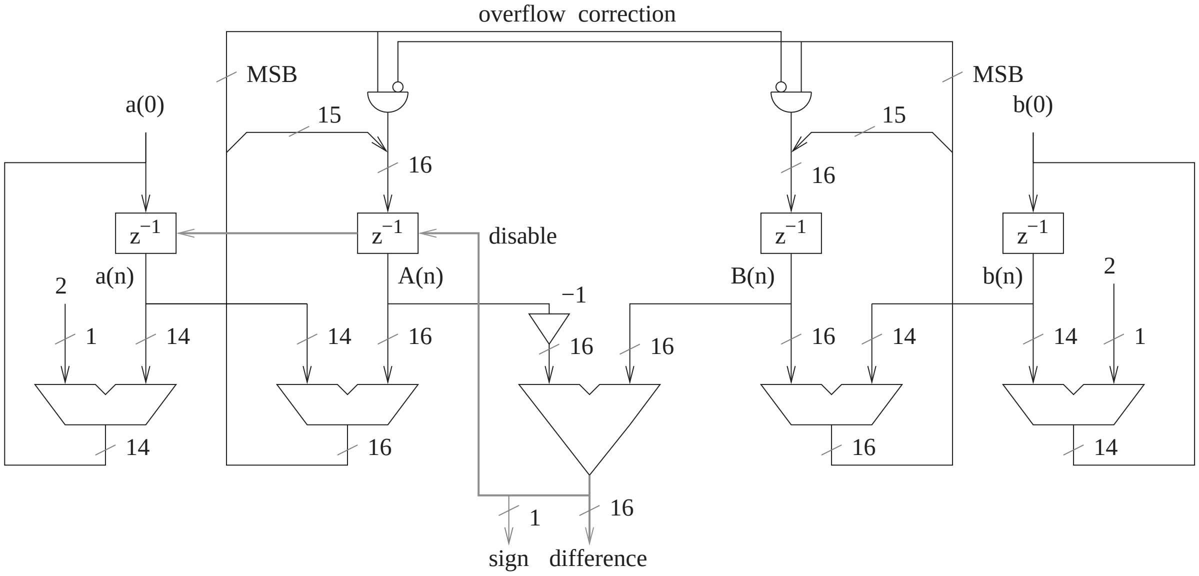
overflow correction
MSB
MSB
a(0)
15
15
b(0)
16
16
z−1
z−1
z−1
z−1
disable
2
a(n)
A(n)
−1
B(n)
b(n)
2
1
14
14
16
16
16
16
14
14
1
14
16
16
14
1
16
sign
difference

Figure B.7: LUCS delay generator.

$$A(n+1) = A(n) + \underbrace{2n + 2k(n) + 1}_{a(n)}, \qquad A(0) = k^2(0) \tag{B.13}$$

$$B(n+1) = B(n) + \underbrace{2n + 1 + \alpha}_{b(n)}, \qquad B(0) = \beta \tag{B.14}$$

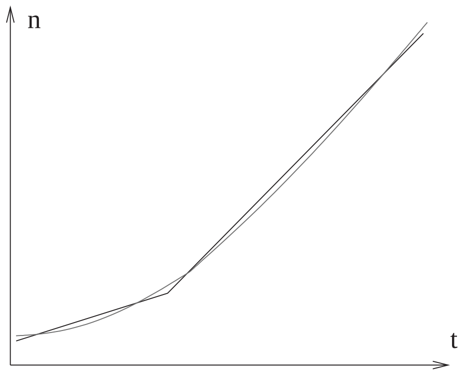

Figure B.8: Piecewise-linear approximation of a delay curve.

The update terms are calculated as:

$$a(n+1) = a(n) + 2, \qquad a(0) = 2k(0) + 1 \tag{B.15}$$

$$b(n+1) = b(n) + 2, \qquad b(0) = \alpha + 1; \tag{B.16}$$

Comparison between $A(n)$ and $B(n)$ determines whether $k(n)$ should be changed. Whenever $A(n) > B(n)$, $k(n)$ has to be decreased by one. It can be calculated that $A(n+1, k-1) = A(n,k)$ and $a(n+1, k-1) = a(n,k)$, therefore the consequence of decreasing k is skipping one update cycle of $A(n)$ and $a(n)$.

A block diagram of the algorithm is shown in Fig.B.7, with some example bus widths.

The overflow correction ensures that when the most significant bits (MSB) of both $A(n)$ and $B(n)$ are 1, then they both become 0. In this way, the same number is subtracted from both expressions. The bus width and the register width should be chosen so that the maximum value of $a(n)$ and $b(n)$ that can occur for some imaging setup, will not cause overflow and loss of information.

One simplification that can be made with this algorithm, is the following: In the beginning of a calculation, it is assumed that the present parameters depict a point on the delay curve. Since only the difference between $A(n)$ and $B(n)$ is of importance, their initial values can be set to 0 without introducing error in the calculation. Thus, β does not have to be used at all.

5 Piecewise-linear approximation

The delay curve can be approximated using a piecewise-linear approximation, as shown in Fig. B.8, where axis t represents the time and axis n represents the sample index. The number of

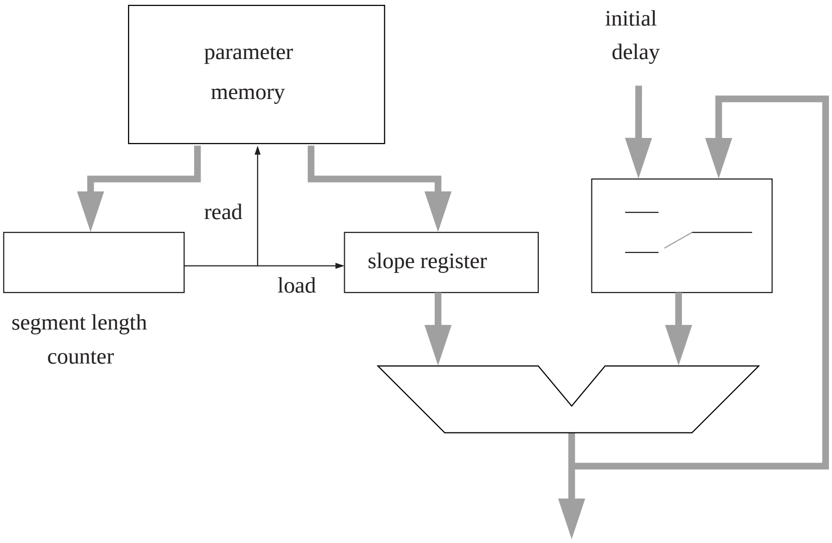

Figure B.9: Piecewise-linear delay generator.

segments is determined by the magnitude of the acceptable error and the curvature of the delay profile. For a less curved delay profile or larger acceptable error, the amount of data (the number of pairs slope/segment length) is less than for a strongly curved profile or smaller acceptable error. After determining the number of necessary segments for representing the delay curve with some predetermined precision, a set of tests is run for determining the necessary bit width of the slope representation word, so that the introduced error from quantization is e.g. below 10 % of the selected maximum delay error.

A simple logic for the delay generation using that method is shown in Fig. B.9. It is very simple and can operate at very high speed. An adder adds the slope to the current delay on each clock cycle. When the segment counter reaches the end of the current segment, new segment length and slope are loaded. The focusing data is represented by an initial sample index and pairs of slope and length for each segment. Delta encoding can be used for the slope information and the segment length, and is used in our study.

6 Comparison between index generation techniques

A comparison between approximation schemes for possible embedding in a compact beamformer was performed. The necessary memory amount, occupied logic resources and power consumption were estimated for a VHDL implementation in an FPGA for a target device XCV2000E by Xilinx. Approximately the same level of optimizations was achieved in the designs. The parameters for the delay generation are given in Table B.1. For the non-oversampled

Parameter	Value
Speed of sound	1540 ms^{-1}
Transducer center frequency f_0	5 MHz
Sampling frequency f_s	140 MHz
Image type	phased array image
Number of channels	32
Transducer pitch	$\frac{\lambda}{2}$
Image depth, cm	15
Target precision, clock periods	± 1

Table B.1: Parameters for the delay generation approximation approaches comparison

Approach	Memory, bits	Logic, gates	Power, mW	Speed, MHz
Piecewise-linear approx.	240	1125	7.8	184.9
General parametric gen.	48	2819	13.6	81.9
LUCS delay generator	48	2095	10.6	131.9

Table B.2: Implementation results for delay generation approaches, per channel

case, the sampling frequency is 40 MHz and the precision is $\pm 1/4$ clock period, for the purpose of achieving good focusing [11].

The implementation results for the delay generation approaches are shown in Table B.2. It can be seen that the general parametric approach, whose algorithm is not optimized, occupies most logic, consumes most, and can not achieve high operation speed. The LUCS delay generator, on the other hand, performs very well, and provides additional intersample precision with little overhead - only one comparator more is necessary (described in [30]). The piecewise-linear approximator is simple and fast, with the only drawback that it requires more memory than the parametric approaches.

7 Discussion

The delay generation methods presented are suitable for use in many contemporary imaging modalities, where the images are created line by line. Their particular strength is in compact implementation of ultrasound beamformers. For an imaging system with 64 channels that produces phased array images consisting of 90 lines, the necessary logic resource for the delay generation is 143040 gates, and the necessary memory is 4320 bits per channel (276480 bits in total), when the LUCS delay generator is implemented. These resources are available in the bigger FPGA devices nowadays. If an external memory connection is acceptable, then the piecewise-linear approximation can be used, with the benefit of better efficiency.

8 Conclusion

The present paper discusses some algorithms for delay generation which have low memory requirements. A comparison between their memory usage, logic resource usage and power consumption has been made. It can be seen that a tradeoff exists between speed and memory requirements. The choice in any particular case would depend on the importance of the different delay generator properties.

Acknowledgments

This work was supported by grant 9700883 and 9700563 from the Danish Science Foundation, by B-K Medical A/S, Gentofte, Denmark, by the Thomas B. Thrige Center for Microinstruments, and by the Danish Research Academy. The authors would like to express their gratitude to Svetoslav Nikolov for his valuable comments on the paper.

APPENDIX

C

Compact FPGA-based beamformer using oversampled 1-bit AD converters

Authors : Borislav Gueorguiev Tomov and Jørgen Arendt Jensen

Presented : Paper submitted for publication in IEEE Transactions on Ultrasonics, Ferroelectrics, and Frequency Control, 2003.

Abstract

A compact medical ultrasound beamformer architecture that uses oversampled 1-bit analog-to-digital converters is presented. Sparse sample processing is used, as the echo signal for the image lines is reconstructed in 512 equidistant focal points along the line through its in-phase and quadrature components. That information is sufficient for presenting a B-mode image and creating a color flow map. The high sampling rate provides the necessary delay resolution for the focusing. The low channel data width (1-bit) makes it possible to construct a compact beamformer logic. The signal reconstruction is done using FIR filters, applied on appropriately selected parts of the delta-sigma modulator output. The approach allows for a multi-channel beamformer to fit in a single field programmable gate array (FPGA) device. A 32-channel beamformer occupies approx. 40 % of the available resources in a Xilinx XCV2000E FPGA, and is capable of operating at 144 MHz, thus providing images with a dynamic range of 60 dB.

1 Introduction

Medical ultrasound has gained popularity in the clinical practice as a quick, portable and affordable diagnostic tool. It has the advantage over the Computed Tomography and the Magnetic Resonance Imaging methods in that the preparation for a scan is minimal and there are no health hazards involved. In the recent past, portable and lightweight ultrasound scanners have been developed [43, 47], which greatly expand the range of situations and sites, where medical ultrasound can be utilized.

The evolution of the ultrasound scanners is directly influenced by the developments in analog and digital electronics. The number of functions and the image quality increases, while the implementation price for any given function decreases with time. One powerful approach for increasing the flexibility and compactness of an ultrasound scanner is moving processing functions from the analog to digital electronics [14].

Delta-sigma modulation [33] (DSM) is one of the techniques that make it possible to decrease the complexity of the analog interface electronics by using digital logic. It offers A/D and D/A conversion using little chip area, provides robust performance and is compatible with the digital CMOS fabrication process. The dynamic range of the conversion depends strongly on the oversampling ratio. Nowadays, converters based on the DSM principle are widely used in audio applications and their extensive use in video and high-frequency applications is a matter of time, depending to a large extent on the progress in the integrated circuit technology.

In this paper, a novel extendable beamformer architecture for use with oversampled 1-bit analog-to-digital converters will be presented. It allows a complete beamformer to be implemented using a single standard FPGA chip.

In Section 2 the memory requirements and the necessary processing power is assessed for the classic digital beamformer architecture. The principles behind the new architecture will be described in Section 3. The performance of the architecture is compared to the classic beamformer performance by processing synthetic and real ultrasound echo data in Section 4.The implementation choices are described in Section 5. The potential and the limitations of the architecture are discussed in Section 6.

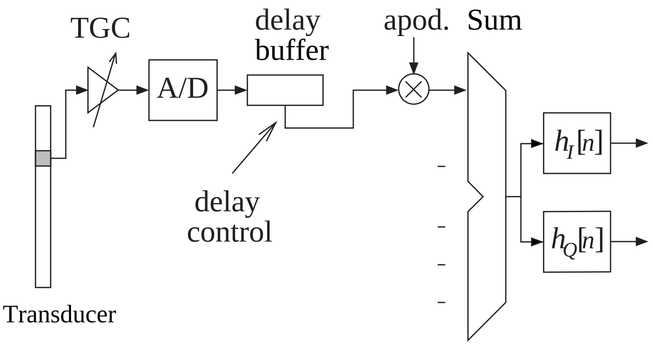

Figure C.1: Beamformer architecture for dynamic receive focusing

2 Traditional beamformer architecture

In the modern commercial scanners, the images are created line by line. A focused ultrasound pulse with central frequency f_0 of 3 to 12 MHz[1] is sent into the tissue. In digital beamformers, the image lines are created by continuously focusing along the pulse propagation axis.

A typical architecture of a modern digital receive beamformer is shown in Fig. C.1. The received echoes are sampled at a frequency of 20 to 60 MHz (usually at 4 times f_0) and the sampled signal at each channel is stored in a delay buffer. At each clock cycle, appropriately delayed samples from each channel are chosen and combined, using weighted sum, into a reconstructed sample. The delay values are calculated as the time it takes the emitted signal to reach the current focal point and propagate back to the receiving transducer elements. The delay resolution and the sample precision determine the quality of the beamforming [10, 11, 13]. In order to achieve sufficient delay resolution, interpolation between samples is used. After summing, the samples pass through a matched filter whose function is to maximize the signal-to-noise ratio of the signal. The quadrature component of the signal has to be derived for generating the envelope data. The most accurate way is to pass the signal through a Hilbert transform filter. The envelope is then calculated as the magnitude of the filtered signals. The envelope is logarithmically compressed and put into an image buffer as an image line. An image typically consists of 128 or more lines. Scan conversion is applied to make the rectangular image display on the screen.

In order to perform the dynamic receive focusing, a digital beamformer needs one sample index and one inter-sample precision parameter per produced sample for every contributing channel. These two parameters can naturally merge into one index with sub-sample precision, that will be decoded by the focusing logic. Another parameter is the weighting (apodization) coefficient for each channel. To keep a constant F-number, the apodization function changes with depth.

A beamformer that reconstructs all samples along the beam axis, has to produce

$$P = \frac{2d f_s}{c}, \tag{C.1}$$

samples, where f_s is the sampling frequency of the ADCs, c is the speed of sound, and d is the image depth. If no optimizations are used with respect to the memory, a N-channel digital beamformer that beamforms L lines per image, with image depth d, has to store PNL index values and PNL weight coefficients.

The necessary calculations per channel are as follows: 2 multiplications per channel per sample (which means per clock cycle) because of the linear interpolation, 1 addition for producing the contribution from that channel. The apodization can either be implemented by using one additional multiplication, or by including the apodization coefficient in the linear interpolation coefficients, in which case they are no longer a natural part of the sample index. The sum of all channels is made using an inverted binary tree of pipelined adders with $\frac{N}{2}+\frac{N}{4}+\frac{N}{8}+\ldots+1=N-1$ adders. The beamforming therefore requires $2PNL$ multiplications and $PL(2N-1)$ additions per image.

---

[1] Skin imaging is done at frequencies of up to 30 MHz with single-element focused transducers, i.e. without any beamforming. That case is not discussed, since the current paper focuses on beamforming.

The matched filtering is done using FIR filter with K coefficients, so K multiplications and $K-1$ additions are needed per reconstructed sample. The same number of operations are needed for creating the quadrature reconstructed sample. Since the in-phase and quadrature signals can be used directly in an autocorrelation blood velocity estimation scheme, the further processing for generating flow estimation data will not be considered.The reconstruction of the in-phase and quadrature component takes $2KPNL$ multiplications and $(K-1)PNL$ additions per image.

In a typical imaging situation, the image depth could be up to 20 cm. For a sampling frequency of 20 MHz and speed of sound $c=1540\ \mathrm{ms}^{-1}$, the number of samples to beamform is $P=5195$. The corresponding amount of memory for a 64-channel system, making 100 lines per image, using 8-bit coefficients and 16-bit index, is approximately 126 MB.

If the transmission follows immediately after reception from the 20 cm depth, the pulse repetition frequency (image line rate) is 3850 Hz, and the frame rate is 38.5 Hz.

The matched filter for the received echo will be the emitted signal convolved twice with the impulse response of the transducer. If the excitation is 2 cycles of a sinusoid at 5 MHz, and the transducer has a 60 % bandwidth around 5 MHz, the length of the matched filter K is 37. With the given parameters the beamforming requires $\approx 2.57\cdot 10^9$ multiplications per second and $\approx 2.52\cdot 10^9$ additions per second. The matched filtering requires $2(K+1)PNL \approx 97\cdot 10^9$ multiplications per second and $KPNL \approx 47.8\cdot 10^9$ additions per second. Real-time processing is therefore only possible with dedicated chips today.

3 New beamformer features

In this section, the principles behind the suggested architecture will be described.

3.1 Sparse sample processing

In the modern scanners, much more information is processed than what actually is displayed on screen. The ultrasound images are shown on raster displays, which rarely have a vertical resolution beyond that of a TV (525 lines for NTSC) or VGA (640x480 pixels). Therefore, on such displays an image line is represented by no more than 512 points. Sparse sample processing in the form of pixel-based focusing was proposed by Karaman et al. [41]. According to that approach, the focal points for which samples are produced, correspond to the raster display pixels. These do not lie on the beam axis (unless for linear array imaging) and therefore, the information for the focusing is hard to derive in a recursive fashion. The present approach processes samples that correspond to equidistant focal points lying on the beam axis. In this way, it is possible to calculate the focusing information in a recursive fashion.

For an imaging situation, where the frequency-dependent propagation attenuation in tissue is a dB/(cm·MHz) and the compensation range (time-gain compensation) of the imaging system is A dB, the achievable image depth is

$$d = \frac{A}{2af_0}, \tag{C.2}$$

where f_0 is the utilized frequency. The image depth, expressed in wavelengths ($\lambda = c/f_0$) of the central frequency, is

$$d_\lambda = \frac{d}{\lambda} = \frac{A}{2ac}, \tag{C.3}$$

and is independent of the wavelength. For a typical image situation where the attenuation coefficient in tissue is 0.5 dB/(cm.MHz), the TGC range is 60 dB and the speed of sound is 1540 m/s, d_λ is 390. Beyond that depth, the dynamic range of the image gradually decreases until the image becomes too noisy to be of any practical value. The SNR drops to zero for the same distance, and the image depth can be at most 780λ.

In case that the signal is reconstructed in 512 points within the high dynamic range area, the spacing between them is 0.76 λ. For the worst case, the spacing is 1.52 λ. These distances are calculated with a relatively weak tissue attenuation. Taking into account a higher value for the attenuation (1 dB/(cm·MHz) is more realistic) will lead to decrease of the reachable image depth and the sample spacing.

The axial resolution of an imaging system can be evaluated by producing the processed echo from a point reflector. The echo signal is the excitation waveform convolved twice with the transducer impulse response. The matched filter applied on the received RF data has the same shape as the echo signal. The image data is produced by filtering the echo signal with the matched filter and calculating the envelope of the result. For a case where the excitation waveform is one period of a sinusoid at a central frequency f_0 and the transducer has the same central frequency and 60 % bandwidth at -6 dB, the imaging system axial resolution at -3 dB is 1.87 λ and is 2.67 λ at -6 dB. These distances are larger than the spacing calculated above, and no image information is lost due to sparse sample processing.

As is the case for the classic beamforming, the reconstruction of the envelope of the signal requires its in-phase and quadrature components. In the sparse sample processing approach, the quadrature signal cannot be produced by filtering of the in-phase signal because the latter is an undersampled representation of the echo signal. Therefore both components have to be created at the same stage. This is achieved by using in-phase and quadrature reconstruction filters, as explained below.

3.2 Beamforming with oversampled signals

A DSM approximates the input signal by feeding back the error into the decision loop, and shaping the quantization noise spectrum away from the given band of interest. Appropriate filtering applied on the modulator output bit stream suppresses the noise and valid samples can be reconstructed at the sampling rate.

Since performing a large number of multiplications and summation at a high clock frequency is not economical, and the target data rate is much lower than the DSM sampling frequency due to the necessary oversampling, the output samples are produced by passing the modulator output through consecutive stages performing of comb filtering and decimation. That reconstruction method is widely used in all DSM ADCs.

The oversampling conversion offers several advantages for ultrasound beamforming over the use of multi-bit ADC. First, the DSMs can be integrated in large numbers on a chip, with the requirement of one input and one-bit output per modulator. Second, the inter-sample interpolation, that is used with multi-bit flash ADC, can be avoided, since the delay resolution of a DSM beamformer is determined by the sampling rate of the modulators, which is inherently high. Third, the time gain compensation and/or channel weighting can be incorporated to a certain degree (providing about 25 dB dynamic range [38]) in the modulator by varying the amplitude of the feedback voltage.

The reconstruction process in DSM beamformers takes place after summation of the aligned echo signals from the channels. Although the reconstruction in this case is applied on a multi-bit stream, the implementation is still more compact than in the case where separate sample reconstruction is performed on each channel.

In dynamic receive focusing, only one channel (corresponding to the transducer element from which the beam/line originates) can have a linear delay development in time. All other channels have non-linear delay development. An oversampled beamformer that uses the aforementioned reconstruction method introduces errors due to the repetition or skipping of samples from different channels.

Previous approaches for focus adjustment

The efforts of Freeman et al. [39] led to the development of a modified modulator architecture, in which the feedback of the modulator is controlled by the delay logic of the beamformer. Such an architecture requires dedicated modulators with external control lines, that are therefore not easily interchangeable.

Kozak and Karaman [40] have proposed sampling with non-uniform sampling clock, specific for each channel, so that the delays are incorporated and all channels produce the same number of samples per image line. That solution requires a large memory for controlling the sampling clock.

Both these approaches come close to utilizing the full performance potential of the oversampled converters, at the expense of more complex beamformer structure, and by disrupting the modulation process.

Approach with preserved modulation process

The new oversampled beamformer architecture differs form the previously suggested ones in that only the necessary amount of samples for display are reconstructed, using FIR filters that yield in-phase and quadrature signal components.

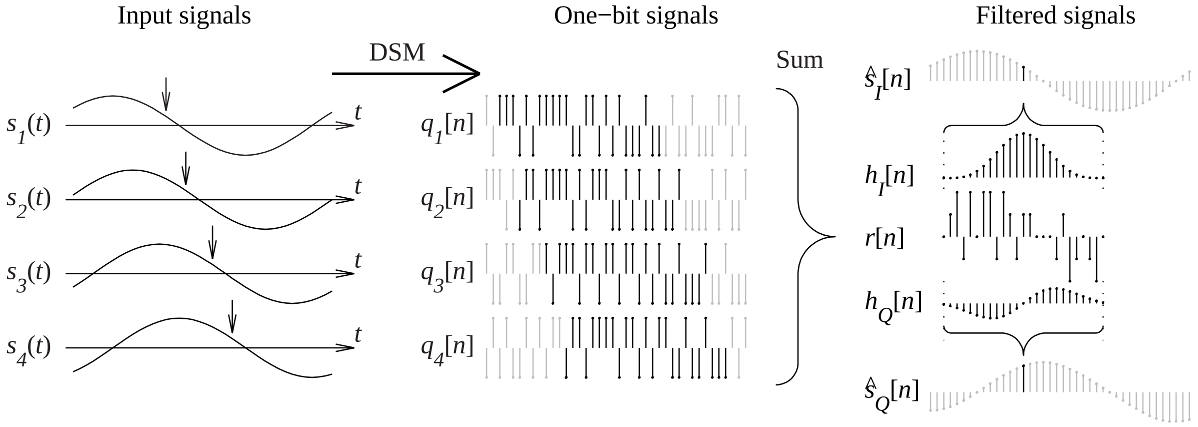

Figure C.2: Signal processing of the proposed beamformer, illustrated with 4 channels. The analog echo signals are modulated into one-bit streams. Corresponding bit-stream sequences form the different channels are added, and the result is filtered to produce in-phase and quadrature components.

The signal processing is illustrated in Fig. C.2. The analog input signals $s_k(t)$ (k being the channel index) from different channels are modulated into bit streams $q_k[n]$ in the DSM. In order to sum the echoes coming form a certain focal point (indicated by arrows in the plots of $s_k(t)$), sequences of bits (shown in black) are selected from the streams $q_k[n]$, at places that correspond to the appropriate channel delays. The length of the sequences is equal to the length of the reconstruction filters that will be used. The selected sequences are summed into sequence $r[n]$. The latter is then filtered by the in-phase $h_I[n]$ and quadrature $h_Q[n]$ filters to yield in-phase $\hat{s}_I[n]$ and quadrature $\hat{s}_Q[n]$ components of the signal from the chosen focal point. In the figure, all possible reconstructed in-phase and quadrature samples are shown in gray. With the chosen sparse sample processing, only every 30th sample has to be produced.

3.3 Reconstruction filters

In general, the DSM reconstruction filter has to be inversely matched to the noise transfer function (NTF) of the modulator, e.g. if the NTF is band-rejecting (pushing noise away form a given center frequency), the filter should be band-pass with the same center frequency.

The best filter for a known signal in the presence of white noise is the matched filter, which is a time-reversed and delayed version of the expected signal [42]. In an ultrasound beamformer, the expected signal is the transmitted excitation, convolved twice with the impulse response of the transducer. Since the amplifiers in transmit and receive have much greater bandwidth than the transducer, their impulse response is not a limiting factor and is not taken into account.

The matched filter for the expected echo signal should be able to filter out the quantization noise, since it has a band-pass transfer function centered around the central frequency of the useful signal, as shown on Fig. C.3. The transfer function of the matched filter drops below -60 dB for frequencies above twice the central frequency. Therefore the matched filter, sampled at the DSM sampling frequency, is used as the in-phase reconstruction filter, and a Hilbert transformation of it is used as the quadrature reconstruction filter.

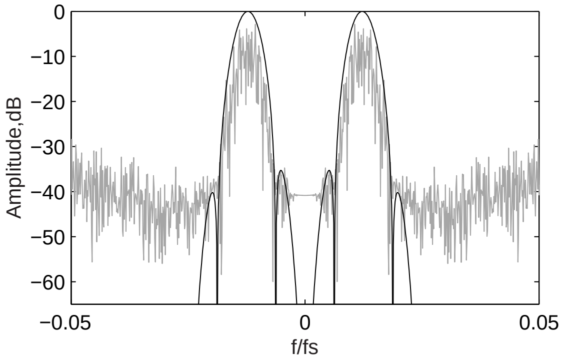

Figure C.3: DSM output spectrum (gray) with frequency response of the matched filter (black) for OSR=20.

4 Image quality

The image quality of the proposed beamformer was compared to that of a conventional digital beamformer. First, the necessary oversampling ratio was calculated. Then, the echo data was processed using oversampled beamforming and using conventional beamforming.

Parameter	**Value**
Transducer center frequency f_0	3 MHz
Target image SNR	60 dB
Target delay-resolution-induced sidelobe level	60 dB
Number of channels	32

Table C.1: Target beamformer parameters

4.1 Calculating the necessary sampling frequency

The target image quality parameters and the number of channels are shown in Table C.1.

The delay resolution of a beamformer has a high impact on its ability to focus in a given direction, while rejecting signals from other directions. According to the most restrictive of the published formulae, given in [11], the worst-case discrete quantization sidelobe level (due to periodic phase errors over the array) in a beamformer is described as:

$$SL_{focus} \approx \frac{2}{mL\cos\varphi}\frac{1}{IPG}\left(\frac{r\lambda}{m}\right)^{\frac{1}{2}}, \tag{C.4}$$

where

$$IPG = \frac{1}{N}\sum_{n=0}^{N-1}\omega_n^2 \tag{C.5}$$

is the incoherent power gain of an N-element array with apodization coefficients $\omega_n, n = 1..N$, φ is the beam angle from the normal, λ is the wavelength, $m = \frac{f_s}{f_0}$ is the ratio of the sampling frequency and the central frequency, L is the aperture size, and r is the distance along the beam.

The maximum random quantization sidelobe level (due to random phase error over the array) is

$$SL_{peak} \approx \frac{\pi}{m}\left(\frac{4.6\,ENBW}{3\,N}\right)^{\frac{1}{2}}, \tag{C.6}$$

where

$$ENBW = \frac{IPG}{CPG},\; CPG = \left[\frac{1}{N}\sum_{n=0}^{N-1}\omega_n\right]^2 \tag{C.7}$$

is the equivalent noise bandwidth, (CPG being the coherent power gain of an N-element array). The maximum sidelobe level is $SL_{max} = max(SL_{focus}, SL_{peak})$.

Calculating these values for the particular case, the following results are obtained: In the near field the random quantization sidelobes are prevalent, and for achieving sidelobe of -60 dB, the necessary sampling frequency is 25.6 times the central frequency of the ultrasound pulse (76.8 MHz), yielding -30 dB sidelobe level in transmit and -30 dB sidelobe level in receive.

Apart from the sidelobe level, the sampling frequency determines also the level of the quantization noise. The quantization noise power of a single multi-bit ADC with quantization step δ, assuming white noise, is

$$P_{qe} = \frac{\delta^2}{12}. \tag{C.8}$$

The coherent sum of the signals across the array would sum up the signal amplitudes and the channel noise powers. Therefore the gain of the SNR in the summed signal will be determined by the apodization profile as follows:

$$G_{SNR} = \frac{\sum_{n=1}^{N} w_n}{\left[\sum_{n=1}^{N} w_n^2\right]^{\frac{1}{2}}}. \tag{C.9}$$

A 32-channel array with Hamming apodization can provide $G_{SNR} = 13.6$ dB, while uniform apodization yields 15 dB. That gain in SNR relieves the requirements towards the sampling frequency.

Having the requirement for 60 dB signal SNR after summation and array contribution of 13.6 dB, the channel SNR has to be 60-13.6 = 46.4 dB. Using a second order DSM, the necessary OSR ($= \frac{f_s}{2\,BW}$) is: $OSR = 10^{\frac{SNR-6.02-1.76+12.9}{50}} = 10.7$. Therefore the sampling frequency has to be more 21.4 times the bandwidth of the ultrasound pulse. In this particular case, the $BW = 1.3\ f_0 = 3.9$ MHz. Therefore the necessary sampling frequency is $f_s = 83.6$ MHz.

Since an expanding aperture will be used, starting with the couple of channels in the middle of the transducer, two channels have to be able to provide 60 dB SNR. Therefore the OSR has to be 17.5 and the sampling frequency has to be 136.3 MHz.

The chosen target sampling frequency was 140 MHz.

4.2 Simulation results

The ultrasound field simulation program Field II [27] was used for generating echo data from scaterers at different depths. The simulation parameters are given in Table C.2. The echo signals were then beamformed using conventional beamforming and using DSM beamformer.

Point spread function

A comparison with reference beamforming PSF is shown on Fig. C.4 and Fig. C.5. As can be seen, the resolution is approximately the same, while the noise level in the DSM beamformation is at about -60 dB due to quantization noise.

Parameter	Value
Speed of sound	1540 ms^{-1}
Transducer center frequency f_0	3 MHz
Sampling frequency f_s	140 MHz
Excitation	2 periods of a sinusoid at f_0
Number of channels	32
Transducer center frequency	3 MHz
Transducer pitch	0.26 mm
Transducer elevation focus	7 cm
Image depth	15 cm.
Transmit apodization	uniform
Transmit focus depth	7 cm
Receive apodization	Hamming window
Receive focus	dynamic
Image type	Phased array image
Image sector	90 degrees
Number of lines	135

Table C.2: Simulation parameters

Parameter	Value
Tube radius	0.01 m
Tube length	0.04 m
Tube center depth	0.04 m
Tube slope	45 degrees
Flow profile	parabolic
Maximum blood velocity	0.5 ms^{-1}
Number of scaterers	3900

Table C.3: Simulated flow parameters

Blood flow simulation

Due to the sparse sample processing, flow estimation on DSM beamformed data can only be performed using autocorrelation approach. The parameters of the simulated flow phantom are given in Table C.3.

The results from flow estimation using conventionally beamformed data and DSM beamformed data are shown in Fig. C.6.

The drops in the estimated velocity profiles are due to the used velocity presence criterion. It can be seen that the shapes of the velocity profiles for given number of shots are similar, which shows that the DSM beamforming with sparse sample processing can successfully replace the conventional beamforming.

4.3 Phantom image

A set of element traces, sampled at 40 MHz, was obtained using the experimental sampling system RASMUS [17]. That data was re-sampled at 140 MHz, and was beamformed according to the suggested architecture. The result, along with a conventionally beamformed image, is shown in Fig. C.7. The number of channels used was 40. It can be seen that the quantization noise of the DSM limits the picture contrast.

5 Implementation

The suggested architecture was implemented in VHDL. A Xilinx FPGA device XCV2000E-7 was targeted. In this section, the implementation parameters, choices and results will be described.

The beamformer structure is shown in Fig.C.8. Its target parameters are given in Table C.4.

Parameter	Value
Target sampling rate	140 MHz
Number of channels	32
Length of the matched filter	120 coefficients
Number of lines per image	80

Table C.4: Target implementation parameters

The number of available clock cycles between two consecutive reconstructed samples is 33, when expanding aperture apodization (maintaining F-number 1 until all elements are used) is used. The necessary length of the FIR filters is above 100 coefficients (the matched filter for the given beamformer parameters was 168). Therefore, the processing path is parallelized in 4.

Sample buffer

For the FPGA implementation of the sparse sample processing beamformer, using Xilinx FPGA device is beneficial in that it incorporates quite a large number of dual-ported memory blocks (Block SelectRAM), which provide simultaneous read and write capability with different word sizes of the read and write operations. For the specific case, the written samples are one-bit wide, while the read data is 4-bit wide.

Since the requested start address for the read operation is specified in one-bit samples, an alignment unit has to be used, so that the first output word from the buffer memory contains the samples 1 to 4 starting with from specified address, the second - bits 5 to 8 and so on. Such an alignment unit is created using a set of 7 two-stage latches. The structure of the sample buffer is shown in Fig. C.9. The 2 least significant bits of the read address determine in what position the output bus multiplexers will stay during the present sample processing cycle. The rest of the read address bits determine the address of the 4-bit word. That address is increased by one on each clock cycle. On the first clock cycle after a valid address is selected, an initial reading into the alignment register is done. Aligned groups of 4 bits are provided from the second clock cycle on. Therefore, in 33 clock cycles, up to 128 bits can be read.

Delay generation logic

After investigation of delay generation techniques with reduced memory requirements [48], a recursive delay generation algorithm, developed by Feldkämper et al. [30], was adopted. The computation logic consists of 4 adders and 1 comparator plus some more control circuitry. The number of parameters per line per channel is 4 (12-bit words).

Sum across the channels

The sum operation across all channels is pipelined in order to incorporate numerous inputs and to process them at high clock frequency. The first stage in the pipeline contains 4-input look-up tables, each producing the sum of the incoming bits form 4 channels. The resulting 8 3-bit numbers are summed in pairs in the second pipeline stage into 4 4-bit numbers. The third summation stage produces 2 5-bit numbers and the 4th stage produces one 6-bit number that is fed into the matched filter. The summation stage has latency of 3 clock cycles, but using simple summation allows operation at very high frequencies (up to 200 MHz in the selected FPGA).

In-phase and quadrature filters

The filter logic is illustrated in Fig. C.10. The length of the filters is constrained by the amount of clock cycles that are available for producing a reconstructed sample. That number is inversely proportional to the density of the beamformed samples, and its maximum value for a given imaging setup can an be calculated as

$$N_r c = \left[\frac{2 f_s d_{max}}{N_s c} \right], \tag{C.10}$$

where d_{max} is the image depth, N_s is the number of reconstructed samples, and c is the speed of sound. The minimum available number of clock cycles is the distance between the first two read operations offsets.

For instance, if 512 points should represent a depth range of 0.15 m, there are 33 cycles available to the filter block for producing in-phase and the quadrature reconstructed samples. In the current design, the filtering operation is parallelized in four, so in-phase and quadrature filters with length up to 128 can be used. A perfect matched filter for the simulation setup has length of 168. Therefore, a shorter filter with length of 120 was used in the implementation.

5.1 Implementation results

After technology mapping, the estimated gate count for the 32-channel beamformer is 1 248 209. The design occupies approximately 40 % of the logic resources of the target FPGA device.

The estimated maximum operation frequency is 144.2 MHz. That estimate takes into account only the logic switching delays. The estimated operation frequency after taking into account the signal routing delays is 71.6 MHz.

The power consumption for clock frequency of 140 MHz is 1.4 W.

6 Discussion

It can be seen that the quantization noise of the DSM limits the image contrast and increasing the OSR improves it. Improvement can be achieved by employing a more sophisticated modulator architecture. With the suggested beamformer architecture, is is easy to swap delta-sigma modulators, as far as they have the same output data size.

The large difference in the operation frequency estimates shows that the size of the design has a negative influence on the achievable performance, unless manual placing with respect to minimizing the longest paths is used. Another approach is pipelining, but it also requires manual placement of the inserted registers in suitable locations so that the length of the signal paths decreases significantly.

7 Conclusion

A novel flexible beamformer architecture utilizing oversampling is presented. The beamformer can be housed in one standard FPGA, which can easily be programmed and upgraded. Based on that beamformer implementation, a compact ultrasound imaging system can be made. A standard portable PC can be used for display, making it a very inexpensive system.

Acknowledgment

This work was supported by grant 9700883 and 9700563 from the Danish Science Foundation, by B-K Medical A/S, Gentofte, Denmark, by the Thomas B. Thrige Center for Microinstruments, and by the Danish Research Academy.

The authors would like to thank all colleagues at the biomedical engineering group for their cooperation and valuable comments on the paper.

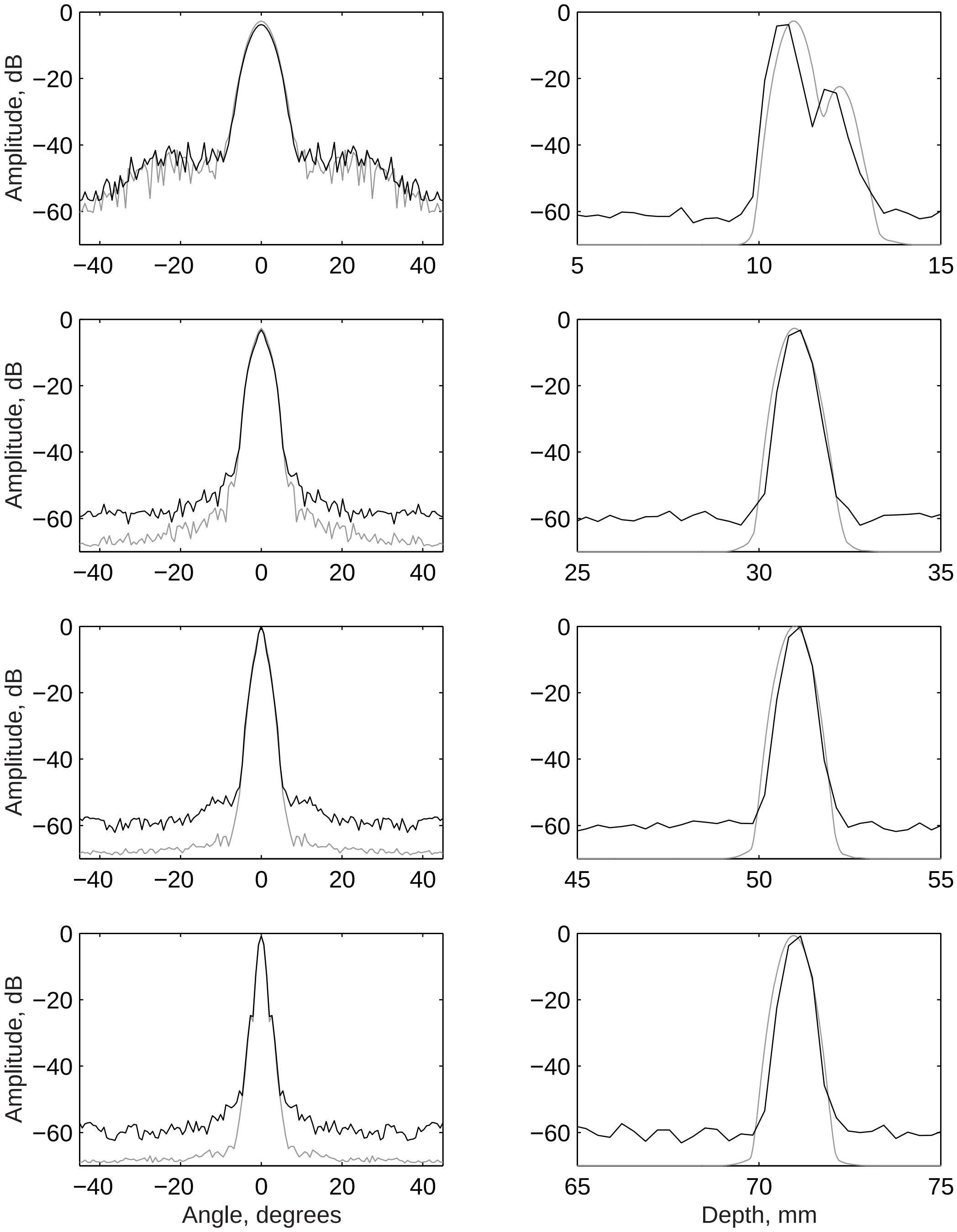

Figure C.4: Simulated PSF: classic beamforming (grey), DSM beamforming (black) for depths of 1,3,5, and 7 cm.

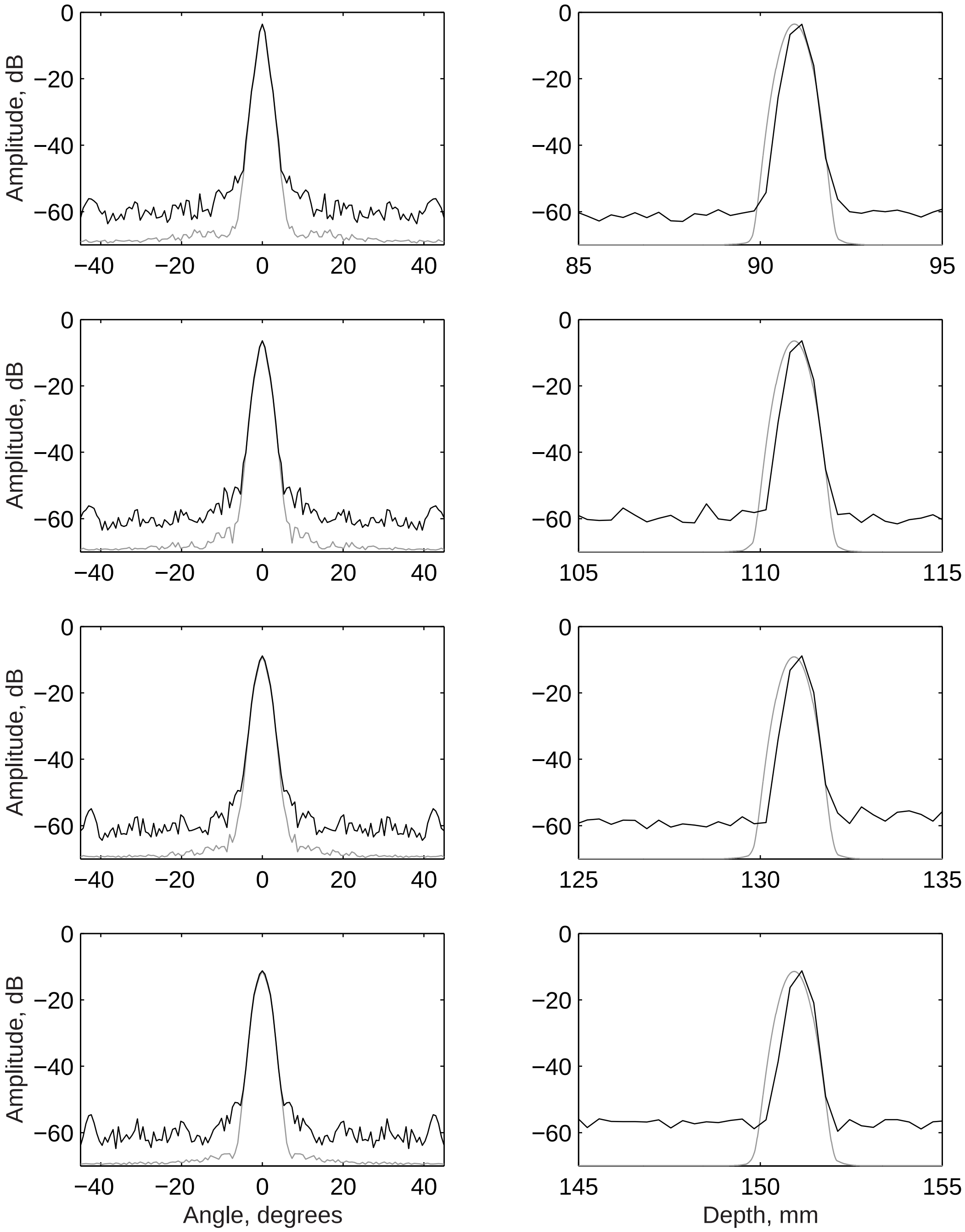

Figure C.5: Simulated PSF: classic beamforming (grey), DSM beamforming (black) for depths of 9,11,13, and 15 cm.

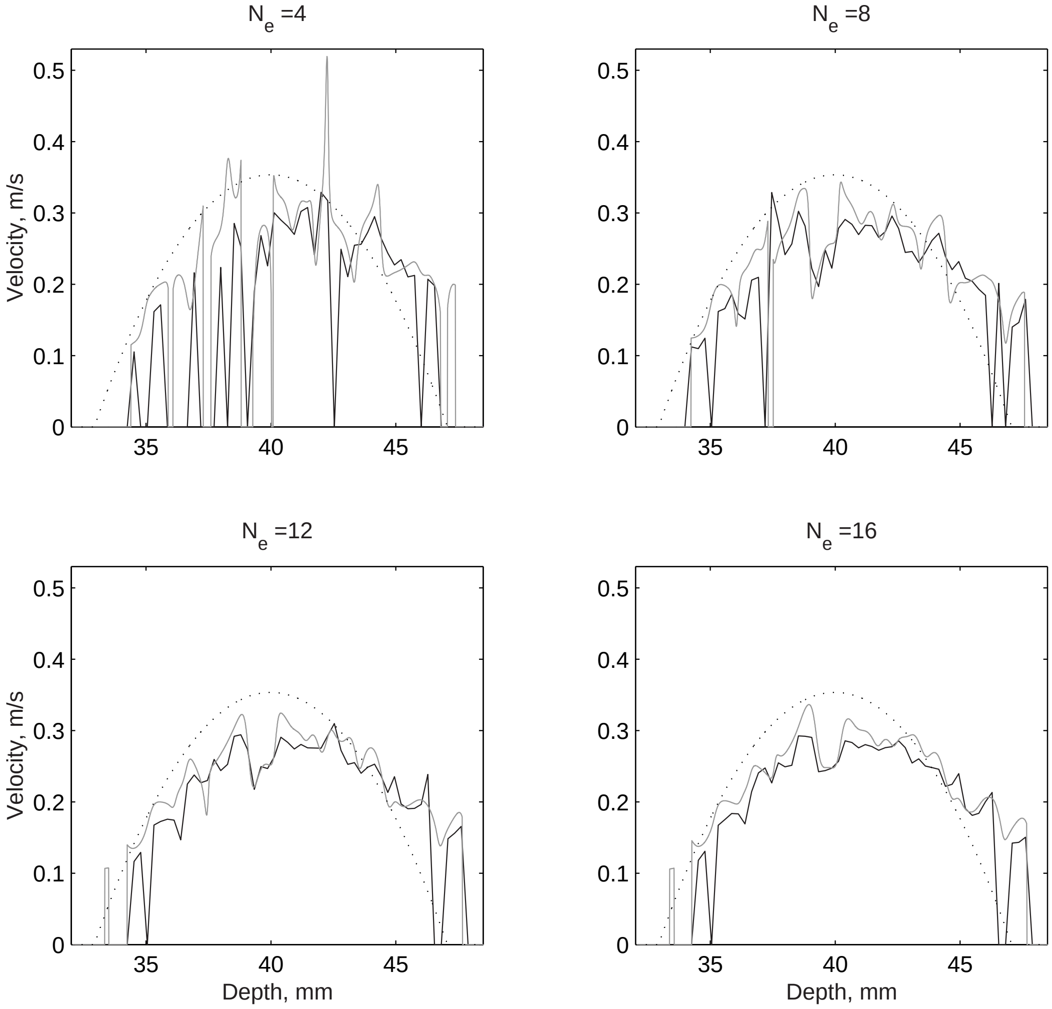

Figure C.6: Velocity profiles obtained using different numbers of shots. The real velocity profile is drawn with dotted line. The flow estimation on conventional beamformed data is drawn in gray. The flow estimation on DSM beamformed data is drawn in black.

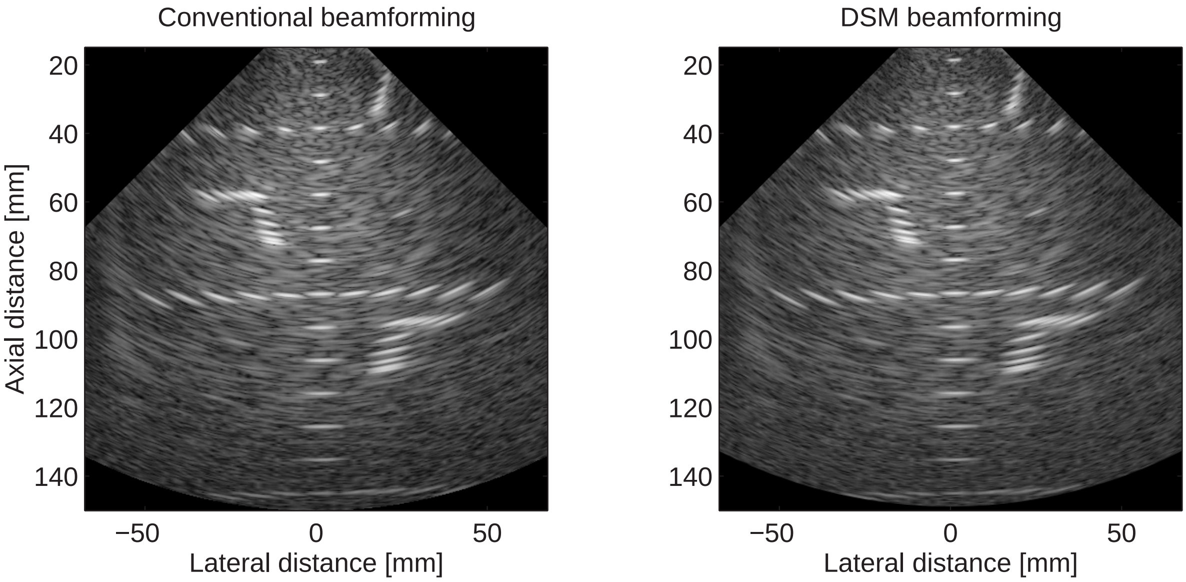
Conventional beamforming
DSM beamforming
Axial distance [mm]
20
40
60
80
100
120
140
−50
0
50
Lateral distance [mm]

Figure C.7: Image created using classic phased array beamforming and DSM phased array beamforming. Dynamic range: 60 dB

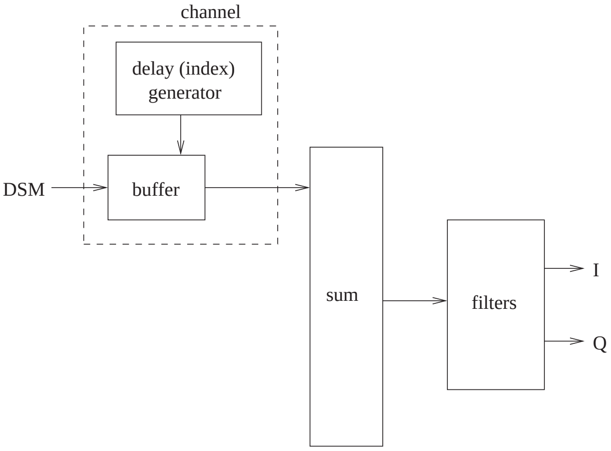
channel
delay (index)
generator
DSM
buffer
sum
filters
I
Q

Figure C.8: Beamformer structure

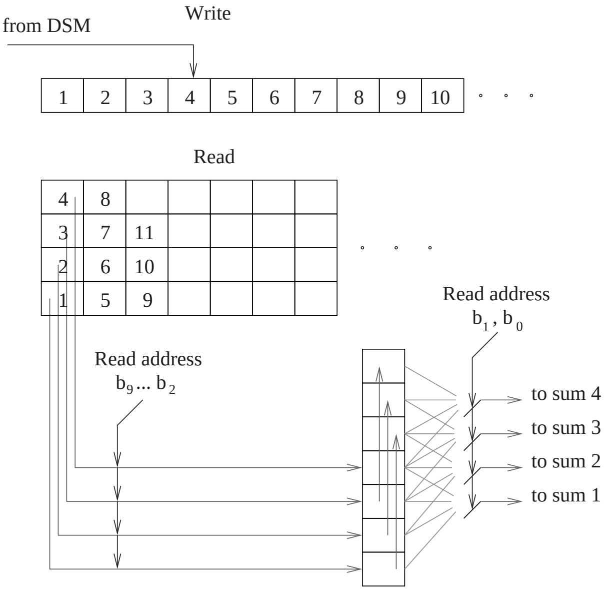
from DSM
Write
1
2
3
4
5
6
7
8
9
10
Read
4
8
3
7
11
2
6
10
1
5
9
Read address
b_1, b_0
Read address
$b_9 \ldots b_2$
to sum 4
to sum 3
to sum 2
to sum 1

Figure C.9: Illustration of the writing and the reading from the sample buffer.

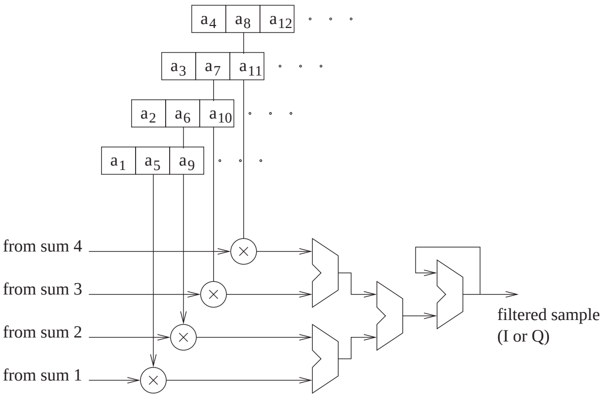
a_4
a_8
a_{12}
a_3
a_7
a_{11}
a_2
a_6
a_{10}
a_1
a_5
a_9
from sum 4
from sum 3
from sum 2
from sum 1
filtered sample
(I or Q)

Figure C.10: Filter block structure

Bibliography

[1] J. A. Jensen. *Estimation of Blood Velocities Using Ultrasound: A Signal Processing Approach*. Cambridge University Press, New York, 1996.

[2] D. H. Johnson and D. E. Dudgeon. *Array signal processing. Concepts and techniques.* Prentice-Hall., Englewood Cliffs, New Jersey, 1993.

[3] A. D. Pierce. *Acoustics, An Introduction to Physical Principles and Applications*. Acoustical Society of America, New York, 1989.

[4] P. R. Stepanishen. Pulsed transmit/receive response of ultrasonic piezoelectric transducers. *J. Acoust. Soc. Am.*, 69:1815–1827, 1981.

[5] J. A. Jensen, D. Gandhi, and W. D. O'Brien. Ultrasound fields in an attenuating medium. In *Proc. IEEE Ultrason. Symp.*, pages 943–946, 1993.

[6] S. W. Flax and M. O'Donnell. Phase-aberration correction using signals from point reflectors and diffuse scatterers: basic principles. *IEEE Trans. Ultrason., Ferroelec., Freq. Contr.*, 35:758–767, 1988.

[7] L. F. Nock and G. E. Trahey. Synthetic receive aperture imaging with phase correction for motion and for tissue inhomogenities - part I: basic principles. *IEEE Trans. Ultrason., Ferroelec., Freq. Contr.*, 39:489–495, 1992.

[8] M. Karaman and H. Koymen. A phase aberration correction method for ultrasound imaging. *IEEE Trans. Ultrason., Ferroelec., Freq. Contr.*, 40:275–282, 1993.

[9] P. A. Magnin, O. T. Von Ramm, and F. L. Thurstone. Delay quantization error in phased array images. *IEEE Trans. Son. Ultrason.*, 28:305–310, 1981.

[10] D. K. Peterson and G. S. Kino. Real-time digital image reconstruction: A description of imaging hardware and an analysis of quantization errors. *IEEE Trans. Son. Ultrason.*, 31:337–351, 1984.

[11] S. Holm and K. Kristoffersen. Analysis of worst-case phase quantization sidelobes in focused beamforming. *IEEE Trans. Ultrason., Ferroelec., Freq. Contr.*, 39:593–599, 1992.

[12] O. T. von Ramm and S. W. Smith. Beam steering with linear arrays. *IEEE Trans. Ultrason., Ferroelec., Freq. Contr.*, 30:438–452, 1983.

[13] B. D. Steinberg. Digital beamforming in ultrasound. *IEEE Trans. Ultrason., Ferroelec., Freq. Contr.*, 39:716–721, 1992.

[14] K. E. Thomenius. Evolution of ultrasound beamformers. In *Proc. IEEE Ultrason. Symp.*, volume 2, pages 1615–1621, 1996.

[15] P. Munk. *Estimation of blood velocity vectors using ultrasound*. PhD thesis, Department of Information Technology, Technical University of Denmark, Lyngby, Denmark, 2000.

[16] T. I. Laakso, V. Välimäki, M. Karjalainen, and U. K. Laine. Splitting the unit delay. *IEEE Sig. Proc. Mag.*, pages 30–60, 1996.

[17] J. A. Jensen, O. Holm, L. J. Jensen, H. Bendsen, H. M. Pedersen, K. Salomonsen, J. Hansen, and S. Nikolov. Experimental ultrasound system for real-time synthetic imaging. In *Proc. IEEE Ultrason. Symp.*, volume 2, pages 1595–1599, 1999.

[18] S. Freeman, P. Li, and M. O'Donnel. Retrospective dynamic transmit focusing. *Ultrason. Imaging*, 17:173–196, 1995.

[19] J. A. Jensen and P. Gori. Improved accuracy in the estimation of blood velocity vectors using matched filtering. In *Proc. IEEE Ultrason. Symp.*, volume 2, pages 1525–1530, 2000.

[20] J. A. Jensen and P. Gori. Spatial filters for focusing ultrasound images. In *Proc. IEEE Ultrason. Symp.*, pages 1507–1511, 2001.

[21] M. H. Bae and M. K. Jeong. A study of synthetic-aperture imaging with virtual source elements in B-mode ultrasound imaging systems. In *IEEE Trans. Ultrason., Ferroelec., Freq. Contr.*, volume 47, pages 1510–1519, 2000.

[22] M. Karaman, P. C. Li, and M. O'Donnell. Synthetic aperture imaging for small scale systems. *IEEE Trans. Ultrason., Ferroelec., Freq. Contr.*, 42:429–442, 1995.

[23] T. X. Misaridis, K. Gammelmark, C. H. Jørgensen, N. Lindberg, A. H. Thomsen, M. H. Pedersen, and J. A. Jensen. Potential of coded excitation in medical ultrasound imaging. *Ultrasonics*, 38:183–189, 2000.

[24] K. L. Gammelmark and J. A. Jensen. Multi-element synthetic transmit aperture imaging using temporal encoding. In *Proc. SPIE: Progress in biomedical optics and imaging*, volume 3, pages 25–36, 2002.

[25] S. I. Nikolov and J. A. Jensen. Comparison between different encoding schemes for synthetic aperture imaging. In *Proc. SPIE - Progress in biomedical optics and imaging*, volume 3, pages 1–12, 2002.

[26] S. I. Nikolov and J. A. Jensen. Velocity estimation using synthetic aperture imaging. In *Proc. IEEE Ultrason. Symp.*, pages 1409–1412, 2001.

[27] J. A. Jensen. Field: A program for simulating ultrasound systems. *Med. Biol. Eng. Comp.*, 10th Nordic-Baltic Conference on Biomedical Imaging, Vol. 4, Supplement 1, Part 1:351–353, 1996b.

[28] S. I. Nikolov. Users guide for the beamformation toolbox. Technical report, Department of Information Technology, DTU, 2000.

[29] K. Jeon, M. H. Bae, S. B. Park, and S. D. Kim. An efficient real time focusing delay calculation in ultrasonic imaging systems. In *Ultrason. Imaging*, volume 16, pages 231–248, 1994.

[30] H. T. Feldkämper, R. Schwann, V. Gierenz, and T. G. Noll. Low power delay calculation for digital beamforming in handheld ultrasound systems. *Proc. IEEE Ultrason. Symp.*, 2:1763 –1766, 2000.

[31] B. G. Tomov and J. A. Jensen. A new architecture for a single-chip multi-channel beamformer based on a standard FPGA. In *Proc. IEEE Ultrason. Symp.*, pages 1529 –1533, 2001.

[32] J. E. Bresenham. Algorithm for computer control of a digital plotter. *IBM Systems J.*, 4:25–30, 1965.

[33] J. C. Candy and G. C. Temes. *Oversampling Delta-Sigma Data Converters - Theory, Design and Simulation*. IEEE Press, 1992.

[34] P. M. Aziz, H. V. Sorensen, and J. Van der Spiegel. An overview of sigma-delta converters. *IEEE Signal Processing Magazine*, 13:61–84, Jan. 1996.

[35] D. Johns and K. Martin. *Analog integrated circuit design*. John Wiley & Sons, Inc, 1997.

[36] R. W. Stewart and E. Pfann. Oversampling and sigma-delta strategies for data conversion. *Electronics & Communication Engineering Journal*, 10:37–47, Feb. 1998.

[37] P. E. Pace. *Advanced techniques for digital receivers*. Artech House, Inc., 2000.

[38] O. Norman. A band-pass delta-sigma modulator for ultrasound imaging at 160 MHz clock rate. *IEEE Journal of Solid-State Circuits*, 31:2036–2041, 1996.

[39] S. R. Freeman, M. K. Quick, M. A. Morin, R. C. Anderson, C. S. Desilets, T. E. Linnenbrink, and M. O'Donnell. Delta-sigma oversampled ultrasound beamformer with dynamic delays. *IEEE Trans. Ultrason., Ferroelec., Freq. Contr.*, 46:320–332, 1999.

[40] M. Kozak and M. Karaman. Digital phased array beamforming using single-bit delta-sigma conversion with non-uniform oversampling. *IEEE Trans. Ultrason., Ferroelec., Freq. Contr.*, 48:922–931, 2001.

[41] M. Karaman, A. Atalar, and H. Köymen. VLSI circuits for adaptive digital beamforming in ultrasound imaging. *IEEE Trans. Med. Imag.*, 12:711–720, 1993.

[42] S. Haykin. *Communication Systems*. John Wiley & Sons, Inc., 2001.

[43] A. M. Chiang, P. P. Chang, and S. R. Broadstone. PC-based ultrasound imaging system in a probe. *Proc. IEEE Ultrason. Symp.*, 2:1255–1260, 2000.

[44] B. Stefanelli, I. O'Connor, L. Quiquerez, A. Kaiser, and D. Billet. An analog beamforming circuit for ultrasound imaging using switched-current delay lines. *IEEE Journal of Solid-State Circuits*, 35:202–211, 2000.

[45] T. K. Song and J. G. Greenleaf. Ultrasonic dynamic focusing using an analog FIFO and asynchronous sampling. *IEEE Trans. Ultrason., Ferroelec., Freq. Contr.*, 41:326–332, 1994.

[46] S. R. Freeman, M. K. Quick, M. A. Morin, R. C. Anderson, C. S. Desilets, T. E. Linnenbrink, and M. O'Donnell. Heterodyning technique to improve performance of delta-sigma-based beamformers. *IEEE Trans. Ultrason., Ferroelec., Freq. Contr.*, 46:771–790, 1999.

[47] J.-J. Hwang, J. Quistgaard, J. Souquet, and L. A. Crum. Portable ultrasound device for battlefield trauma. *Proc. IEEE Ultrason. Symp.*, 2:1663–1667, 1998.

[48] B. G. Tomov and J. A. Jensen. Delay generation methods with reduced memory requirements. In *Proc. SPIE - Med. Imag.*, page To be published, 2003.